

Temporally and Spatially Resolved Characterisation of Flexible micro-Tube Plasmas as Ionisation Sources for Analytical Applications

Zur Erlangung des akademischen Grades eines

Dr.rer.nat

von der Fakultät Bio- und Chemieingenieurwesen
der Technischen Universität Dortmund
genehmigte Dissertation

vorgelegt von

M.Sc. Caiyan Tian

aus

Longnan, China

Tag der mündlichen Prüfung: 13.06.2025

1. Gutachter: Prof. Dr. Oliver Kayser
2. Gutachter: PD. Dr. Joachim Franzke

Dortmund 2025

Zusammenfassung

Helium ist ein häufig verwendetes Entladungsgas in plasma-basierten Ionisierungsquellen. Der Ionisierungsmechanismus wurde lange Zeit als ähnlich dem von Ionisierungsquellen bei atmosphärischem Druck angesehen. Plasmen, die mit Argon betrieben werden, erhalten zunehmend Aufmerksamkeit. Die Ionisierungseffizienz von Argonplasmen kann mit der von Heliumplasmen konkurrieren und diese teilweise sogar übertreffen. Der Ionisierungsmechanismus von Argonplasmen bleibt jedoch eine Herausforderung.

Um diese Herausforderung anzugehen, untersucht die vorliegende Arbeit systematisch die Anregungs- und Ionisierungsmechanismen von Plasmen, die mit Helium, Argon sowie Neon, Krypton und Xenon betrieben werden, durch spektroskopische Charakterisierung. Der Fokus liegt auf der Ausbreitung dieser Plasmen in einem Mikroröhrchen sowie auf ihrer Ausbreitung in die Umgebungsluft. Zudem wurde ein sogenanntes Diagnosegas mit definierten Emissionswellenlängen eingeführt, um die Umgebungsluft zu ersetzen und detaillierte Simulationen und Untersuchungen der Anregung und Ionisierung der Umgebungsluft zu ermöglichen.

Es wird eine alternative Erklärung für die Produktion von Reaktandionen in plasma-basierten Ionisationsquellen vorgeschlagen, die neue Einblicke bietet und langjährige Erklärungen des sanften Ionisierungsmechanismus infrage stellt. Diese umfassende Untersuchung der grundlegenden Entladungseigenschaften von Plasmen trägt nicht nur zum besseren Verständnis der für analytische Anwendungen kritischen Ionisierungsmechanismen bei, sondern eröffnet auch neue Möglichkeiten für miniaturisierte Ionisierungsquellen in analytischen Plattformen.

Abstract

Helium is a common discharge gas in modern plasma-based ionisation sources. The ionisation mechanism has long been assumed to be like the classical atmospheric pressure chemical ionisation source. Plasmas operated with argon has been obtaining increasing attention. The ionisation efficiencies of argon plasmas can compete with helium plasmas and argon is additionally less expensive. However, the ionisation mechanism of argon plasmas is unknown or incorrect and remains challenging.

To address this challenge, the present work systematically investigates the excitation and ionisation mechanisms of Helium, Argon, Neon, Krypton and Xenon driven plasmas through spectroscopic characterisation. The focus is on the propagation of the named plasmas within a micro tube as well as their propagation to ambient air. Furthermore, another gas called diagnosis gas with well-defined emission wavelengths is introduced later to replace the surrounding ambient air, enabling detailed simulation and examination of the excitation and ionisation of ambient air.

An alternative explanation to produce reactant ions in plasma-based ionisation sources is proposed, providing new insights that challenge long-standing explanations of soft ionisation mechanisms. This comprehensive investigation into the fundamental discharge properties of plasmas not only enhances the understanding of ionisation mechanisms critical to analytical applications but also opens new miniature ionisation sources for analytical platforms.

Table of Contents

Symbols and Abbreviations	IX
1 Introduction.....	1
1.1 Motivation	1
1.2 Scope of This Thesis.....	4
2 Fundamentals	7
2.1 Ionisation Source	7
2.1.1 Plasma Generation	8
2.1.2 Atmospheric Pressure Chemical Ionisation.....	10
2.1.3 Dielectric Barrier Discharge	12
2.1.4 F μ TP Ionisation Source	22
2.2. Optical Emission Spectroscopy	24
2.2.1 Optical Emission.....	24
2.2.2 USB 4000 Spectrometer	25
2.2.3 Kymera Adaptive Focus Imaging Spectrograph	27
2.3 Data Acquisition and Processing.....	28
2.3.1 Data Acquisition.....	28

Table of contents

2.3.2 Data Processing	32
2.4 Gases	33
3 FμTP Ionisation Source: A Dielectric Guided Discharge	35
3.1 Experimental Arrangement.....	36
3.2 Overview of Species in a <i>He</i> -F μ TP	37
3.3 Temporally and Spatially Resolved Emission Spectra.....	39
3.3.1 Propagation of the Whole Emission	39
3.3.2 Propagation of Selected Species	42
3.3.3 Generation Mechanism of N ₂ ⁺	49
3.4 Conclusion	52
4 Discharge Mechanisms of the FμTP	55
4.1 Mass Spectrometric Characterisation of the F μ TP	57
4.2 Spectroscopic Characterisation of the F μ TP	63
4.2.1 Experimental Conditions	63
4.2.2 Overview of Species in Different Plasmas	64
4.2.3 Plasma Development Within the Capillary	70
4.2.4 Plasma Development to Ambient Surrounding.....	82
4.2.5 Proposed Ionisation Mechanism in Ambient Surrounding	86
4.2.6 Plasma Development During the Negative Half Cycle	88
4.3 Conclusion	90
5 Excitation and Ionisation of a Diagnosis Gas	93
5.1 Experimental Arrangement.....	94
5.2 Diagnosis Plasma Ignition in Front of the F μ TP.....	96
5.3 Diagnosis Plasma Ignition Beyond a Glass Wall	105
5.3.1 Beyond the Diagnosis Tube Wall	105
5.3.2 Beyond the Discharge Capillary Wall	107

Table of contents

5.4 The Closed micro-Tube Plasma 109

5.5 Conclusion 111

6 Summary and Outlook..... 113

Bibliography..... 117

Appendix 123

List of Publications and Patent.....127

Declaration of Pre-Published Contents.....129

Acknowledgements.....131

Curriculum Vitae.....133

Symbols and Abbreviations

Symbols

Symbol	Unit	Description
c	$\text{m}\cdot\text{s}^{-1}$	Light speed
d	-	Spacing/grating constant
E	$\text{V}\cdot\text{m}^{-1}$	Electric field
h	-	Planck constant
P	$\text{C}\cdot\text{m}^{-2}$	Polarization density
t	μs or ns	Time
α	degree	Incident angle
β	degree	Diffracted angle
ϵ_0	$\text{C}\cdot\text{V}^{-1}\cdot\text{m}^{-1}$	Electric permittivity of vacuum
ϵ_r	-	Dielectric constant of a material
λ	nm	Wavelength
ν	Hz	Frequency
χ_e	-	Electric susceptibility of the dielectric material

Symbols and Abbreviations

Abbreviations

Symbol	Description
A ⁺	Ionized state of A
A ^{**}	Upper excited states of A
A [*]	Lower excited states of A
A ^M	Metastable states of A
AC	Alternating Current
API	Atmospheric Pressure Ionisation
APCI	Atmospheric Pressure Chemical Ionisation
AMS	Ambient Mass Spectrometry
Ar	Argon
a.u	Arbitrary Units
CCD	Charge Coupled Device
C μ TP	Closed micro-Tube Plasma
DC	Direct Current
DBD	Dielectric Barrier Discharge
DBDI	Dielectric Barrier Discharge Ionisation
DDG TM	Digital Delay Generator
EI	Electron Ionisation
eV	electron Volt
F μ TP	Flexible micro Tube Plasma
FNS	First Negative System
He	Helium
HexD	2,5-hexanedione
HV	High Voltage
Hz	Hertz
ICCD	Intensified Charge Coupled Device
I _D	Displacement Current
I _{PL}	Plasma Current
iDBDI	inverse Dielectric Barrier Discharge Ionisation
iLTP	inverse Low Temperature Plasma
kHz	kilohertz
Kr	Krypton
LTP	Low Temperature Probe
m/z	mass-to-charge
mbar	millibar
mm	millimetre
ml min ⁻¹	milliliters per minute
ms	millisecond

Continued on next page

– continued from previous page

Abbreviation	Description
<i>Ne</i>	Neon
Ni ⁶³	Nickel ⁶³
NIR	Near-Infrared
nm	Nanometer
ns	Nanosecond
OES	Optical Emission Spectroscopy
p-FWHM	position-Full Width at Half Maximum
ppm	parts per million
sccm	Standard cubic centimeters per minute
SNS	Second Negative System
SPS	Second Positive System
UV	Ultraviolet
vDBD	variable Dielectric Barrier Discharge
VUV	Vacuum Ultraviolet
Xe	Xenon

Introduction

1.1 Motivation

The ionisation source is an essential part in mass spectrometry (MS) and ion mobility spectrometry (IMS). These are two powerful analytical techniques for the identification and determination of substances. Ionisation sources that are easy to handle and reliable are in high demand for both techniques.

In addition to the commonly used electrospray ionisation (ESI) [1,2], ultraviolet (UV) ionisation lamps and beta-radiation electron emitters [3], plasma-based ionisation techniques have become suitable sources for a wide variety of applications [4-12]. A soft plasma-based ionisation source enables the generation of intact molecular ions with minimal fragmentation of analyte molecules, ensuring accurate molecular characterisation. One of the main processes of soft ionisation is the proton transfer from reactant ions such as protonated water clusters ($(\text{H}_2\text{O})_{n+1} \text{H}^+ = (\text{H}_2\text{O})_n \text{H}_3\text{O}^+$) to molecular analytes (M), producing protonated target molecules $[\text{M}+\text{H}]^+$.

Atmospheric pressure chemical ionisation (APCI) is one of the most common plasma-based ionisation sources. APCI, based on corona discharge, produces reactant ions by a series of reactions, in which N_2^+ is considered as the primary ion [3,13,14]. With the development of modern plasma-based ionisation sources, such as dielectric barrier

Chapter 1 Introduction

discharge ionisation (DBDI) and low-temperature plasma (LTP) probe, the generation of reactant ions has been widely studied [7,15-17]. Despite different types of gas discharges and different configurations, the ionisation mechanisms of these modern sources have long been regarded as similar to APCI [3].

The operation voltage of a Helium (*He*) plasma is low, which greatly increases the usability of *He*. *He* is hence usually used as the discharge gas in modern plasmas. A well-accepted mechanism is focused on long-lived, high-energy *He* metastables (He^M) that interact with atmospheric gases, such as nitrogen, generating N_2^+ by Penning ionisation, as illustrated in Figure 1.1 [18,19]. The formation of N_2^+ leads to the generation of protonated water clusters, which subsequently protonate analyte molecules. In this sense, the soft ionisation mechanism in *He* plasmas seems to be completely understood and reasonable.

Recently, more and more plasmas developed for soft ionisation have been operated with argon (*Ar*) instead of *He*. *Ar* has some advantages, such as being cheaper than *He*. From the soft ionisation point of view, *Ar* plasmas can compete with *He* plasmas, and in certain instances the ionisation efficiency is even higher than that of *He* plasmas [12,20,21]. However, the ionisation mechanisms that are widely acknowledged for *He* plasmas are

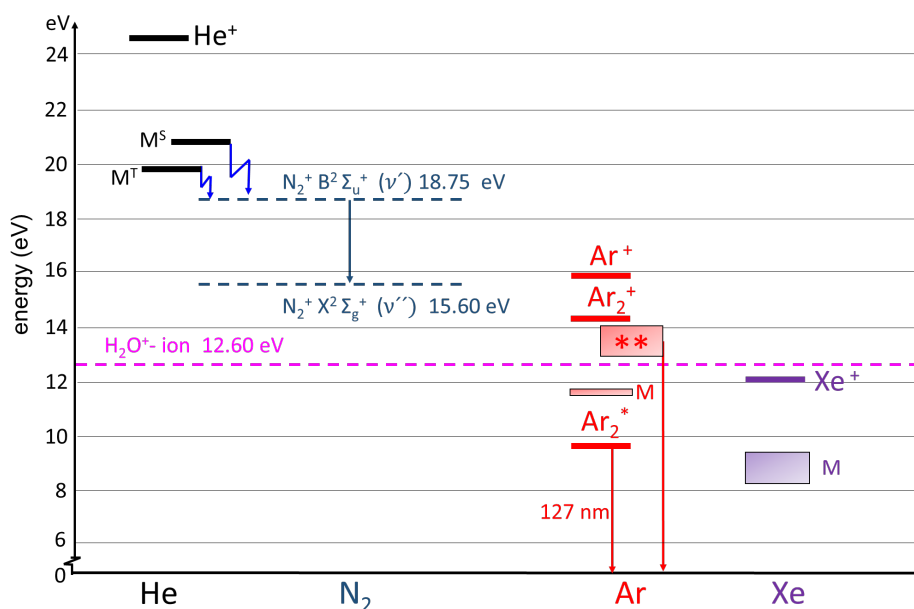


Figure 1.1: Diagram of the excitation and ionisation energy states for *He* (black), *Ar* (red), *Xe* (purple), related nitrogen species (dark blue) and the ionisation energy of water (magenta). The down-pointing arrows show the transitions from upper states to lower states. The blue zigzag arrows show the Penning ionisation path in case of a *He* driven plasma.

1.1 Motivation

inapplicable to *Ar* plasmas. In an *Ar* plasma, the energy levels of Ar^M are lower than the ionisation levels of N_2 and H_2O , as shown in Figure 1.1. Consequently, Penning ionisation between Ar^M with a long lifetime and air components is not feasible in the same manner as it occurs in a *He* plasma.

As the research progressed, either the generation of reagent ions or the ionisation process of analytes seemed to be reasonably deduced with the profound insight of scientists. Different hypotheses may explain the protonation of analytes. Ar^+ and Ar_2^+ can be generated in *Ar* plasmas [22,23]. In principle, Ar^+ has sufficient energy to ionise N_2 and H_2O molecules, resulting in the formation of $N_2^+ X \ ^2\Sigma_g^+$ and H_2O^+ . These ions subsequently contribute to the production of protonated water clusters. However, due to the short lifetime of Ar^+ and Ar_2^+ , the density of $N_2^+ X \ ^2\Sigma_g^+$ and H_2O^+ generated by charge transfer is low [24]. In addition, photoionisation might play a role in the formation of H_2O^+ in *Ar* plasmas, as *Ar* plasmas are theoretically capable of emitting photons with energies ranging from 12.6 eV to 15.8 eV via atomic transitions [12,25]. Nevertheless, the formation of excimers increases at gas pressures higher than 300 mbar [26,27]. As illustrated in Figure 1.1, the corresponding energy of the excited excimer state Ar_2^* in an *Ar* plasma is insufficient to ionise water molecules.

To enable those unverified mechanisms to be supported by sufficient experiments and fully understand soft ionisation mechanism, the Flexible micro-Tube Plasma (F μ TP), a plasma-based ionisation source, is applied in this thesis. The F μ TP allows to ignite plasmas with different noble gases without changing the configuration.

In addition to *He* and *Ar*, which are commonly used as discharge gases, neon (*Ne*), krypton (*Kr*), and xenon (*Xe*) are also used. From the point of view of plasma physics, a *Xe* plasma is not expected to be able to ionise water molecules due to the fact that any state of *Xe* is lower than the ionisation level of water, as shown in Figure 1.1. Although some of these gases are too expensive to be used for analytical applications, the related measurements, however, can help to understand the ionisation mechanism by indirect deduction. In summary, a clear view on the generation of reagent ions and the ionisation mechanism is an important guide for the improvement of the ionisation efficiency, the renovation of ambient ionisation sources, and the exploitation of their full potential applications.

1.2 Scope of This Thesis

This thesis focuses on the elucidation of the discharge mechanisms of F μ TP as well as the excitation and ionisation of a diagnosis gas outside the discharge capillary to understand the soft ionisation mechanisms of plasma-based ionisation sources for analytical applications. At the beginning of this work, the ionisation source is described. Following the introduction of plasma generation, several plasma-based ionisation sources with a focus on dielectric barrier discharge (DBD) are presented. Optical emission spectroscopy (OES) serves as a widely utilised characterisation technique for the study of plasmas. Two spectrometers used in this thesis are therefore presented. The data acquisition using different spectrometers and data processing are explained in detail. The introduction of gases used will complete the chapter **Fundamentals**.

Motivated by the origin of F μ TP and its excellent soft ionisation performance, the main work will begin with a detailed characterisation of the discharge mechanism of the F μ TP ionisation source in one discharge cycle. *He* will be used first as the discharge gas because of the low ignition voltage and the seemingly clear discharge mechanism. The discharge processes of F μ TP will be compared with those of capillary DBDI. By changing the density of N₂ in *He*, the effect of impurities on discharge and the mechanism of N₂⁺ generation will be studied.

In the chapter **Discharge Mechanisms of the F μ TP**, not only *He*, but also *Ne*, *Ar*, *Kr* and *Xe* will be applied as discharge gases to understand the soft ionisation mechanism of plasma-based ionisation sources. The ionisation efficiencies of the named plasmas will be preliminarily investigated by MS measurements. Furthermore, the propagation of excitation and ionisation within the discharge capillary, as well as their propagation into ambient air during the positive half cycle will be examined. On the basis of these results, the ionisation mechanism of these plasmas as soft ionisation sources will be proposed. Finally, the discharge development during the negative half cycle will be conducted as well.

In the final main part of this thesis, a diagnosis gas with known optical emission wavelengths will be introduced to substitute the ambient air components to confirm the proposed ionisation mechanism. To achieve this, various experimental designs will be utilised. A so called diagnosis tube will be employed to deliver such gas. The generation and propagation of plasmas along the diagnosis tube will be examined. This discussion pertains to the investigation of whether soft ionisation is caused by Penning ionisation, charge transfer, or photoionisation occurring between the plasmas and the ambient air.

1.2 Scope of This Thesis

The integration and application of the distinct insights culminate in the development of a new version of the ionisation source, which is also applicable as a soft ionisation source for analytical applications. A brief presentation of the new ionisation source will finish the main part of this thesis. The proposal of a novel ionisation source may be regarded as a reward for the extensive characterisation efforts undertaken in this thesis.

Fundamentals

The fundamentals begin with a brief overview of the function of the ionisation source in MS and IMS. Ionisation sources can be categorised into different groups based on their nature of ionisation. Through the scope of this thesis, the discharge mechanism of F μ TP is systematically characterised. In this chapter, the origin and features of F μ TP are addressed in the initial section of this chapter. Building upon this basis, the methodology employed for plasma characterisation is presented. Subsequently, two different spectrographs are addressed.

2.1 Ionisation Source

MS and IMS are analytical techniques with many strengths that have been widely applied in many fields. MS is based on the mass-to-charge (m/z) ratio of the ions to be analysed and IMS utilises the specific mobility of a substance in the gas phase to identify and quantify analytes [28-32]. For that, the neutral analytes of interest have to be ionised. Resulting ions are accelerated to the detector to be detected. The ionisation process of the analytes is fulfilled by the ionisation source. Therefore, the ionisation source is an essential component in MS and IMS devices.

Chapter 2 Fundamentals

The ionisation techniques are broadly categorised into “hard” and “soft” sources, each differing in the amount of energy imparted to the sample molecules and the resulting degree of fragmentation. Some ionisation methods, such as electron ionisation (EI) source, cause extensive fragmentation [33]. Once the molecules are fragmented, they cannot be measured as an intact molecule. This fragmentation provides detailed structural information and functional groups present. This category of ionisation source is identified as a hard source.

In contrast to the hard ionisation sources, some ionisation sources produce intact molecular ions with minimal fragmentation under appropriate experimental conditions. This preservation of the molecular ion is beneficial for analysing the precise molecular weight of analytes. A controlled fragmentation can be applied if needed. These sources are referred to as soft ionisation sources. The most common sources of soft ionisation in MS are ESI and APCI [1-3,34-36]. They are operated at atmospheric pressure and thereby are so-called atmospheric pressure ionisation (API) source. ESI operates on the principle of the electrospray mechanism. APCI is a plasma-based ionisation source. Throughout the scope of this thesis, only plasma-based ionisation sources are described in the following sections.

2.1.1 Plasma Generation

Plasma, often referred to as the “fourth state of matter”, is a partially or fully ionised gas including free electrons, ions, excited neutral species, and neutral species in the ground state. The generation of a plasma involves providing sufficient energy to a gas to overcome the binding forces that hold electrons to atoms or molecules, resulting in ionisation.

The application of an electric field is a common method for the energy supply. When a high voltage (HV) is applied across a gas-filled volume, free electrons are accelerated in the electric field. The energetic electrons collide with the neutral gas atoms or molecules (A), leading to the excitation and ionisation of the gas.

When the energy of an electron is less than the ionisation energy of particle A but higher than an excited state (A^*), the particle will be excited. This process is expressed in Equation 2.1.



2.1 Ionisation Source

When the energy of an electron exceeds or is equal to the ionisation energy of the particle, the particle will be ionised, forming A^+ . At the same time, a secondary electron is generated. The ionisation process is given in Equation 2.2.



The newly formed electrons are accelerated, resulting in further excitation and ionisation through collisions. This process leads to a cascade of excitation and ionisation events.

Under atmospheric pressure, the high density of neutral particles leads to frequent collisions, dissipating electron energy, and making ionisation less effective. As a result, an electric field created by an electrode is incapable of producing ions over an extended distance [37]. However, the ions generated by the applied electric field create a localised region of intense ionisation, where a self-sustained electric field is established [38,39]. This field subsequently accelerates the electrons, leading to further excitation and ionisation.

In addition to the application of an electric field as an energy supply, the ionisation of particle A can also take place by absorbing a photon with sufficient energy to eject one electron. This process is referred as to photoionisation, as described in Equation 2.3.



Excited species and ions are either rapidly quenched due to collisions with neutral gas molecules or undergo transitions to lower energy states via photon emission, ultimately returning to their neutral particle forms. In plasma physics, the emission processes of excited species are typically faster than collisional processes. This phenomenon occurs because the timescales associated with radiative decay are typically shorter than those correlated with collisional de-excitation [40].

The metastable state (A^M) is forbidden to decay to the ground state according to the quantum mechanism selection rules, resulting in an extended lifetime [41]. A^M loses its energy by collision with other partners. The collisional processes of A^M with a neutral particle (B) are expressed as follows.



When particle B is excited, the process is referred as to excitation transfer [42]. On the contrary, when particle B is ionised, the process is termed Penning ionisation [18].

Chapter 2 Fundamentals

The quenching process of an ion by particle B can be expressed as a charge transfer mechanism (Equation 2.6), wherein particle B is ionised.



The emission processes of excited states as well as ions will be discussed in detail in a later section (see Section 2.2.1).

2.1.2 Atmospheric Pressure Chemical Ionisation

APCI is one of the ionisation sources based on a corona discharge. Typically, corona discharge occurs at sharp edges or other regions where the electric field strength is concentrated. When the local electric field becomes sufficiently strong to ionise the dielectric medium, such as the surrounding air, a plasma is formed. Figure 2.1 (a) shows the main component of an APCI ionisation source and ion formation in corona discharge [43]. A photograph of the plasma generated by corona discharge is shown in Figure 2.1 (b). The following discussion will focus on the generation of positive ions using APCI and related soft ionisation mechanisms.

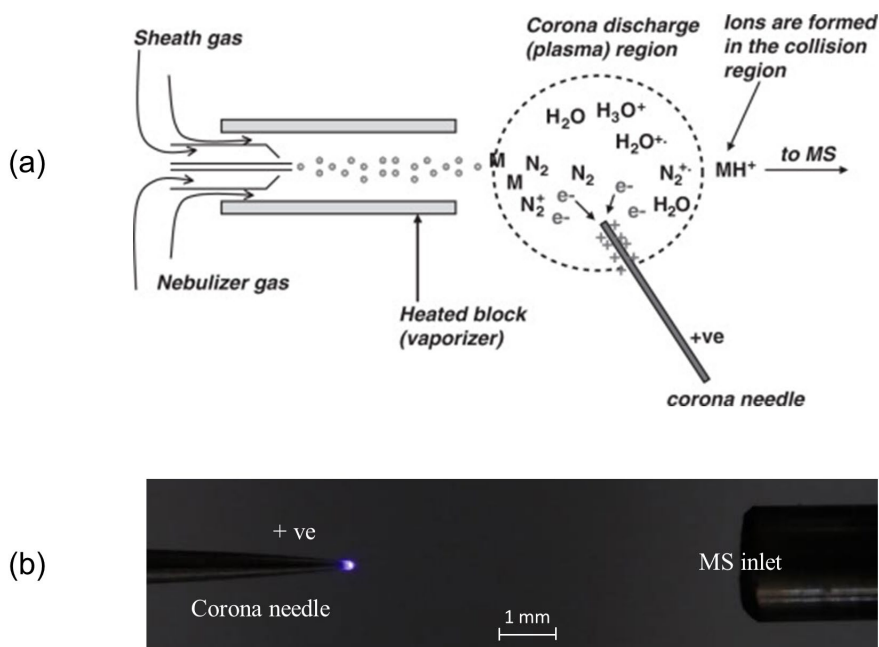


Figure 2.1: (a) Main components of an APCI ionisation source. Ion formation in the corona discharge and collision region is also indicated. Reprinted with permission from [43], Copyright 2008 Elsevier. (b) A photograph of the plasma generated by corona discharge.

2.1 Ionisation Source

The first studies on soft ionisation of molecules using a corona discharge in air at atmospheric pressures were reported by Shahin in 1966 [13]. It was hypothesised that the primary ions of a discharge (e.g. N_2^+ , O_2^+ , etc.) may be responsible for the formation of $(H_2O)_n H_3O^+$ ions by the production of either a hydride or through a charge exchange process. In the case of the production of a hydride, such as N_2H^+ or O_2H^+ , a reaction would proceed as follows [13].



This is followed by the collision of the hydride with a water molecule to form an H_3O^+ .



In the case of the charge exchange process, the reaction is as follows,

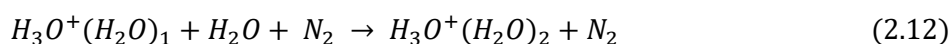
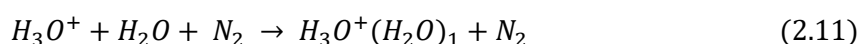


and the subsequent reaction.



In both cases, the first member of the $(H_2O)_n H_3O^+$ series is yielded, while the former case was suggested to be a more likely pathway [13].

Four years later in 1970 Good *et al.* [44] described ion-molecule reactions in pure nitrogen and nitrogen containing traces of water at a total pressure of 0.5 to 4 Torr, in which the following reactions were involved:



It was argued that the production of H_3O^+ occurs almost exclusively through the reactions (2.9 b) and (2.10) [44].

In 1973 Horning *et al.* [3] reported a detection system based on a mass spectrometer with an external ionisation source containing a Ni^{63} source at atmospheric pressure using

Chapter 2 Fundamentals

nitrogen as carrier gas. They cited the above given Equations applicable for pressures between 0.5 and 4 Torr of Good *et al.* and added the very first Equation here called (2.7 a).



Since then, the scheme reaction was cited in MS or IMS textbooks and publications, whenever soft ionisation or protonation is explained, even if the experiments were carried out in ambient air. The scheme of reactions from reaction (2.9) to (2.12) is considered to be the heart of APCI [3,14].

Although APCI technique is very elegant, it is always desirable to develop novel ionisation sources. The pursuit of novel ionisation sources has long been an important research activity in the field of analytical chemistry, and research in this area has increased significantly [4,7,9,12,45,46]. The increased results are due, on the one hand, to the growing application of MS as an analytical method. On the other hand, as a result of the continuous improvement of mass spectrometers, the ionisation source usually becomes the bottleneck of the MS techniques. The innovation of novel ionisation sources, which are simple to configure and small in dimension, particularly for micro-mass spectrometer interfaces, greatly reduces the amount of sample required. This reduction in sample quantity would be of great benefit in the detection of valuable substances. It also contributes to the development of miniature portable analytical systems [9,32,47]. Due to the simple configuration, ease of operation, and efficient energy use, DBD has become a versatile and efficient choice in MS applications.

2.1.3 Dielectric Barrier Discharge

The defining characteristic of DBD is the presence of a dielectric layer that separates at least one electrode from the discharge gap [48]. Various DBD configurations have been designed, such as volume discharge [49], surface discharge [49], and capillary discharge [50]. Different from the glow or direct discharge where a direct current (DC) voltage is applied, the operation of the DBDs requires an alternating current (AC) voltage of several hundred volts up to 10 kilovolts (kV), depending on the electrode configurations and gases. The applied frequencies range from several 100 hertz (Hz) to tens of kilohertz (kHz).

The application of a voltage will lead to an initial polarisation of the dielectric layer caused by sorting the charged species inside the dielectric layer along the applied electric field.

2.1 Ionisation Source

When the discharge is homogeneous and the electric field E is linear, the polarisation density P can be given as Equation 2.1 [51,52],

$$P = \varepsilon_0 \chi_e E \quad (2.1)$$

where ε_0 is the electric permittivity of the vacuum and χ_e is the electric susceptibility of the dielectric material. In principle, χ_e indicates the ability for a dielectric material to be polarized, which is related to the electric permittivity, given as Equation 2.2 [51,52],

$$\chi_e = \varepsilon_r - 1 \quad (2.2)$$

where ε_r is the dielectric constant of a material. This means that the higher the ε_r of a material, the better the named material can be polarised.

The initial polarisation and discharge process is illustrated in Figure 2.2 [53], where a volume discharge configuration is used as an example. Both electrodes are covered by dielectric layers. Usually, when no voltage is applied to the electrodes, the charged species are randomly distributed in the dielectric layer, as shown in Figure 2.2 (a). Once a voltage

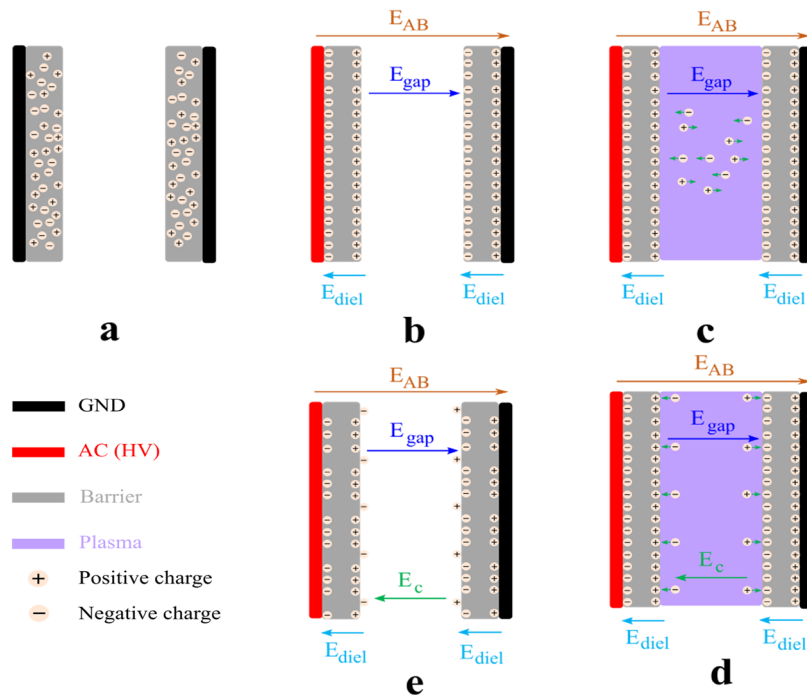


Figure 2.2: Schematic diagram of the plasma ignition in the first half cycle (a - e) in a planar DBD configuration with each electrode covered with a dielectric layer (GND: ground electrode, (AC) HV: (Alternating current) high voltage electrode). Adapted with permission from [53], Copyright 2021 Elsevier.

Chapter 2 Fundamentals

U_{AB} is applied to one electrode and another electrode is grounded, a corresponding electric field \vec{E}_{AB} across the dielectric layers, and a discharge gap is created. At the same time, the positive as well as the negative species in the dielectric layers are rearranged, resulting in an electric field \vec{E}_{diel} in each dielectric layer in the opposite direction to the applied \vec{E}_{AB} (Figure 2.2 b). The effective electric field across the discharge gas is now given by $|\vec{E}_{gap}| = |\vec{E}_{AB} + 2\vec{E}_{diel}| = E_{AB} - 2E_{diel}$. When the increase of $|\vec{E}_{gap}|$ exceeds beyond the dielectric strength of the discharge gas used, the discharge will be ignited (Figure 2.2 c), generating charged species, electrons, and excited neutrals in the volume.

The charged species are attracted and accumulated on the dielectric surface, leading to another electric field \vec{E}_c across the discharge gap in the opposite direction to the \vec{E}_{gap} , as shown in Figure 2.2 d. Therefore, the effective electric field can now be expressed as $|\vec{E}_{gap}| = |\vec{E}_{AB} + 2\vec{E}_{diel} + \vec{E}_c| = E_{AB} - 2E_{diel} - E_c$. With the accumulation of the charges on the surface, the dielectric layers are gradually depolarised and $|\vec{E}_c|$ increases. When the effective $|\vec{E}_{gap}|$ is not sufficient to sustain the discharge, the plasma will extinguish (Figure 2.2 e). The discharge is not reignited until a sufficiently high effective $|\vec{E}_{gap}|$ is created again. This is the reason why an AC voltage should be applied to a DBD discharge. DBD is considered as a discontinuous discharge. The processes of polarisation, the ignition of the plasma, the depolarisation and the reignition have been discussed in detail in the reviews [53,54], where more than one discharge half cycle with the application of a square voltage was picked up to offer a complete explanation.

DBD has experienced significant development and extensive investigation since its initial application as a soft ionisation source in 2007 [55]. In the same year, a DBDI source was reported as an ambient ionisation source for ambient mass spectrometry (AMS) [5,6]. The initial research of DBDI designed a pin-to-plane configuration as shown in Figure 2.3 (a). A sheet of glass is inserted between the electrodes to serve as the dielectric layer. The discharge gas flows through the hollow stainless steel needle. An AC voltage is applied between two electrodes, generating a stable plasma. The dielectric layer is also used as the object platform.

LTP probe [7] is another source based on DBD and was designed as a pin-to-ring configuration. It uses a tube as the dielectric material to separate two electrodes. One of the electrodes is inserted into the tube, and the other is wrapped around the outer surface of the tube. The schematic diagram of the LTP probe is shown in Figure 2.3 (b). The

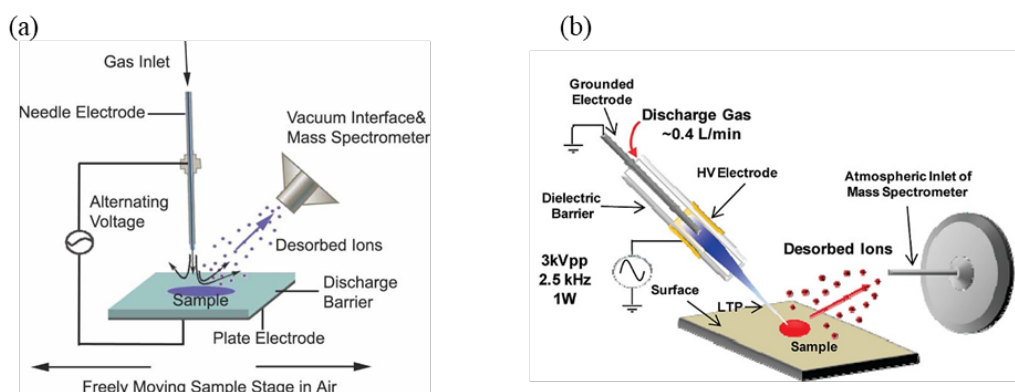


Figure 2.3: (a) The schematic diagram of DBDI ionisation source. Reprinted with permission from [6], Copyright 2007 John Wiley & Sons, Ltd. (b) The schematic diagram of LTP ionisation source. Reprinted with permission from [7], Copyright 2008 American Chemical Society.

discharge gas flows through the tube to produce a plasma that can extend out of the tube and come into direct contact with the analytes. This allows any type of object to be analysed without having to place the analytes between the two electrodes.

Both aforementioned DBDI and LTP probe configurations share a common feature in that only one electrode is covered by the dielectric material. They fulfil the criteria of having at least one electrode separated from the rest of the discharge volume, qualifying it as a DBD, and the rest of the discharge design can be freely chosen and optimised for specific application. In both configurations, one of the electrodes is in direct contact with the plasma.

According to the definition of a DBD, designs with two electrodes where both electrodes are covered by dielectric material can be realised. A notable example of this configuration is the capillary DBDI [15,50]. Capillary DBDI allows the use of glass, ceramic, or quartz capillaries serving as dielectric materials, where two ring electrodes are wrapped on the outer surface of the capillary. A gas suitable for plasma operation is introduced into the capillary. With a sufficiently high polarisation of the dielectric layer, a plasma is ignited. A typical glass capillary DBDI ionisation source is shown in Figure 2.4. In this arrangement, the two electrodes are not in contact with the plasma. It was referred as to a full dielectric barrier discharge [56]. The design in which only one electrode is covered by dielectric material and the other is in direct contact with plasma during the discharge process was referred as to a half dielectric barrier discharge [56].

Both the LTP probe and the capillary DBDI ionisation source employ a tubular structure that serves as the dielectric material and the working gas channel. However, the tube

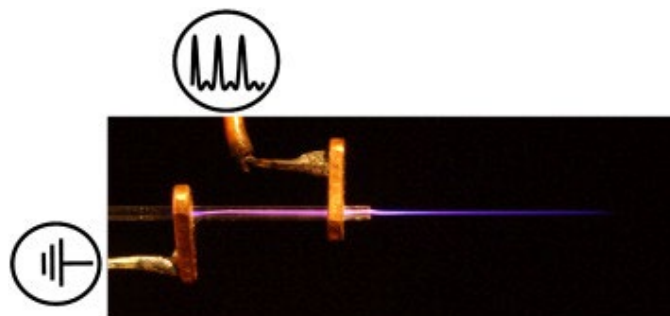


Figure 2.4: The schematic diagram of capillary DBDI ionisation source. Reprinted with permission from [50], Copyright 2009 Elsevier.

diameters, gas flow rates, applied voltages, and power consumption of these two types of discharges are quite different. The common LTP probe has a large size with an inner diameter of several millimetres (mm) and high gas consumption of 400 ml min^{-1} [7,57]. Capillary DBDI has an inner diameter of a few hundred micrometres (μm) and therefore a reduced gas consumption of 150 ml min^{-1} [50].

The discharge processes of a capillary DBDI are shown in Figure 2.5 [38]. Three discharge processes were identified as marked by arrows [38,58-60]. These processes take place at different times and positions. With the application of HV, the capillary is polarised. A displacement current (I_D) is generated during polarisation. Polarisation accelerates the first seed electrons, which in turn excite the discharge gas by collisions. Excited and ionised species decay to their lower energy levels, giving the first emission signals.

The emission signals start at the HV electrode and propagate in two directions. The signal propagating beyond the exit of the capillary into the ambient air is referred to as plasma jet. The other signal propagating towards the grounded electrode inside the capillary is referred to as early plasma, whose emission occurs with the appearance of the displacement current. They were categorised into the first stage (1st stage), the stage of propagation of the first emission phenomenon after the ignition of the plasma by the polarisation effect of the discharge capillary. The generated positive ions form a streamer head that attracts and accelerates electrons toward it, leading to further excitation and ionisation. Such a self-guiding process results in a wave-like development away from the position of the initial polarisation. This development continues until the newly generated ions are unable to sustain the next round of excitation and ionisation. At this point, they eventually extinguish, which is the case of the plasma jet. Alternatively, the development of excitation and

ionisation may reach the grounded electrode, resulting in a new discharge. This is the case with the early plasma.

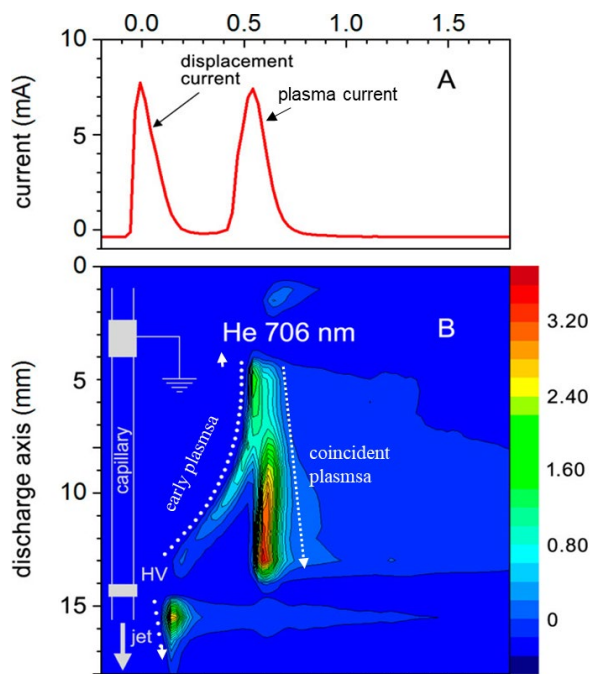


Figure 2.5: Discharge processes of capillary DBDI. The upper part shows the measured current (red). The arrows highlight the displacement current (I_D) and the plasma current (I_{PL}). The lower part shows the spectral emission of He 706 nm. Adapted with permission from [38], Copyright 2016 American Chemical Society.

During the propagation of the early plasma, a quasi-neutral channel filled with free charges, including positive as well as negative particles, is formed gradually. This means that this channel can be considered as a conductor. Once the early plasma reaches the grounded electrode, the channel is short-circuited, leading to a reignition process. Since this emission signal occurs simultaneously with the plasma current (I_{PL}), it is referred to as coincident plasma. It starts at the grounded electrode and propagates towards the HV electrode in the capillary. It was categorised into the second stage (2nd stage) of discharge. This emission signal is more intense and propagates very fast compared to that observed in the 1st stage.

The discharge is usually optimised to meet different demands. In this way, quite different experimental parameters might need to be applied. This makes it difficult to explain exactly why a certain design is suitable for one application but not for another. Noble gases such as *He* and *Ar* are commonly used as discharge gases, which are chemically inert. The impurities such as nitrogen, oxygen, or water are considered to be important for plasma propagation and ionisation of analytes. In both the *He*-driven DBDI and LTP probe, N_2^+ is

Chapter 2 Fundamentals

generated by Penning ionisation, charge transfer, and electron collision. Through cascade reactions, protonated water clusters are produced. They are crucial reactant ions in the soft ionisation process.

In addition, the most striking difference between the capillary DBDI and LTP probe is the electrode configuration. Ionisation sources with different configurations may have differentiated discharge properties, which could affect the ionisation process and thus lead to a distinct analytical performance. It is therefore challenging to fully explain whether the variations in performance observed as a soft ionisation source arise from differences in operational parameters or are caused by fundamental differences between the different discharges. As a result, the demand for further systematic research on DBD remains high.

One solution to these challenges is to keep all the external parameters such as applied voltage, capillary diameter, gas flow rate, the relative positions of the ionisation source and mass spectrometer, etc. constant, with only the operation mode being different. For that, Klute *et al.* proposed a variable dielectric barrier discharge (vDBD) [56]. It allows easy switching between full-dielectric (capillary DBDI) and half-dielectric (LTP) operating modes. The schematic diagrams of the common LTP (A), capillary DBDI (B), and vDBD design (C) are shown in Figure 2.6.

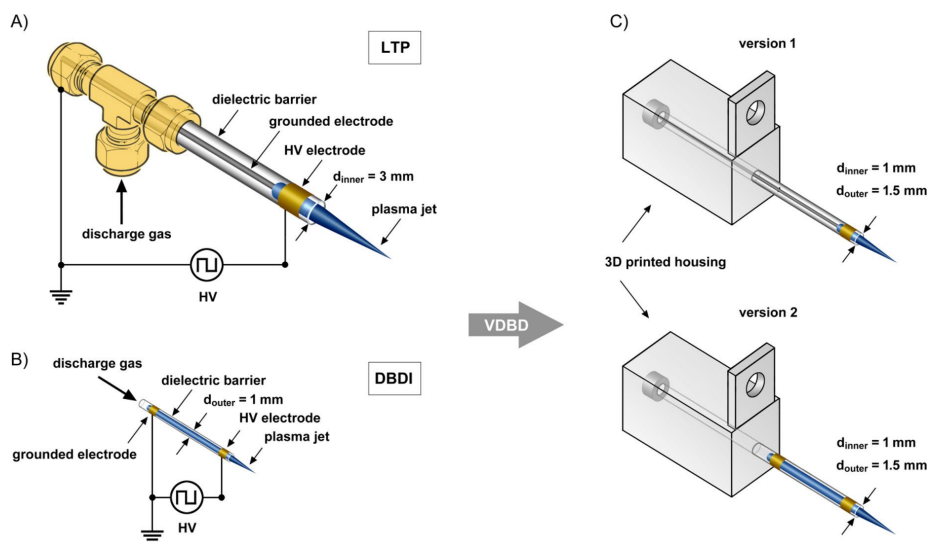


Figure 2.6: Schematics of the LTP (A), DBDI (B) and vDBD (C). The vDBD can be operated in two configurations, the LTP configuration (top) and the DBDI configuration (bottom) representing the electrode configuration of the name giving discharge type. Reprinted with permission from [56], Copyright 2017 American Chemical Society.

2.1 Ionisation Source

In vDBD, the discharge capillary is mounted in a 3D printed housing. It is possible to switch freely between LTP and DBDI configurations with the movable grounded wire and cylindrical electrodes in the same capillary. Consequently, the configuration of LTP in vDBD is reduced in size relative to the conventional LTP and aligns with the dimensions of the capillary DBDI. This design facilitates a systematic investigation and comparison of the discharge behaviour observed in both LTP and DBDI configurations.

Figure 2.7 shows the development of discharge in different configurations using vDBD [61,62]. The DBDI configuration exhibits discharges essentially similar to normal DBDI as explained above (Figure 2.5).

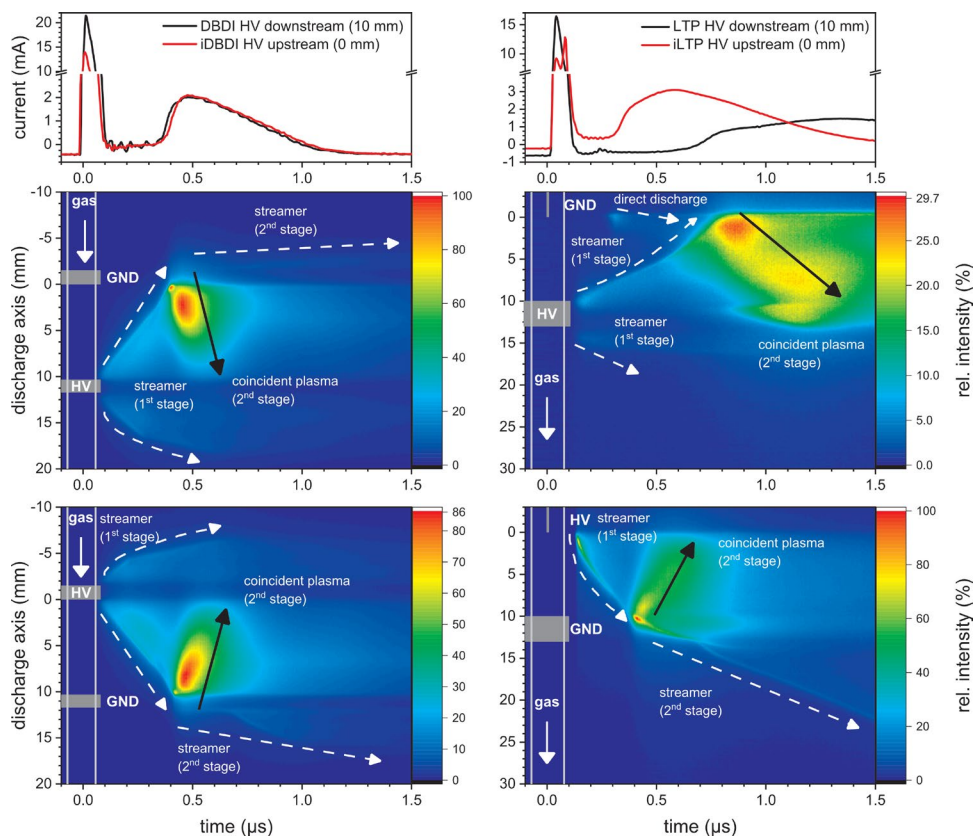


Figure 2.7: Development of the temporally-spatially resolved optical emission of the DBDI (left) and LTP (right) configurations. The top row shows the measured current. The middle row of measurements shows the usual polarity of the electrodes with the HV electrode downstream of the gas flow and the GND upstream. The reverse polarity is shown in the bottom row of measurements. Reprinted with permission from [62], Copyright 2021 Elsevier.

In terms of discharge development in the LTP configuration, the plasma also develops from the initial ignition at the HV electrode, propagating outward and inward to the grounded electrode during the 1st stage, as marked by the arrows. Once one of the developments

Chapter 2 Fundamentals

reaches the grounded electrode, the coincident plasma is initiated. As a result, similar discharge processes were identified in LTP and DBDI.

When the LTP is coupled to the mass spectrometer as an ionisation source, the HV is usually applied to the ring electrode close to the capillary nozzle, while the pin electrode is grounded. In this case, the potential direct discharge between the HV electrode and the mass spectrometer inlet is avoided because of the effective obstruction of the dielectric barrier layer. In contrast, when HV is applied to the pin electrode, a direct discharge between the electrode and the inlet of the mass spectrometer may take place, damaging the instrument.

With the decrease of the discharge diameters, in particular the inner diameter of the discharge capillary, it is possible to change the polarity of electrodes without producing a direct discharge to the mass spectrometer inlet. In other words, the HV is applied to the pin electrode, and the grounded electrode is located in the vicinity of the mass spectrometer inlet. In this manner, the discharge is called inverse LTP (iLTP). Similarly, an inverted DBDI (iDBDI) can be realised when the polarity of the electrodes is changed in normal DBDI. The discharges of iDBDI and iLTP are shown at the bottom of Figure 2.7.

The change in electrode polarity in the symmetric full-dielectric DBDI configuration (left in Figure 2.7) basically changes the direction of discharge development. This causes the emission profile in an iDBDI to look like a mirror image compared to the profile of a DBDI. In addition, only a slightly lower emission intensity is obtained in an iDBDI compared to that in a DBDI. It is resulting from the unidentical two-ring electrodes. Therefore, the change in polarity of the electrodes could only play a minor role in the mechanism of excitation and ionisation of a full-dielectric DBDI configuration [62].

However, in the case of the half-dielectric LTP configuration, the effect of the electrode polarity is much more significant. In addition to the change in the direction of the emission development, the excitation and ionisation wave of the 1st stage in iLTP propagates only in the direction of the grounded electrode. It does not split in the reverse direction, as observed at the HV ring electrodes in the DBDI, iDBDI and LTP configurations. The absence of such a split is due to the asymmetry of the needle electrode. This asymmetry inhibits the propagation in the contrary direction, which thus leads to a focused formation of excitation and ionisation of the 1st stage in one single direction. Such a focusing of the 1st stage results in a stronger emission intensity as well as a higher propagation velocity compared to the LTP configuration.

2.1 Ionisation Source

Anyway, the coincident plasma is present in each of the above configurations. The exploration of a DBDI as a soft ionisation source has demonstrated important findings. It has been shown that the coincident plasma is not suitable for the soft ionisation process. However, it does lead to fragmentation and dissociation of molecules [38]. In order to enhance the application of these ionisation sources in soft ionisation, it is desirable to suppress the coincident plasma from the entire discharge processes and retain only the discharge of the 1st stage.

Adjusting the ratio between the durations of the positive and negative half cycles of the applied square wave voltage, known as the duty cycle, can fulfil such a requirement, where the durations of the positive half cycle are shortened [60]. In this way, the applied voltage drops before the excitation and ionisation wave reaches the grounded electrode, resulting in an incomplete discharge. Such discharge has a higher analytical potential for soft ionisation than fully developed plasma discharge. Moreover, the generation of the coincident plasma can also be avoided by removing the physical ground electrode of the iLTP configuration [9,61,62]. The discharge in the named case is shown in Figure 2.8.

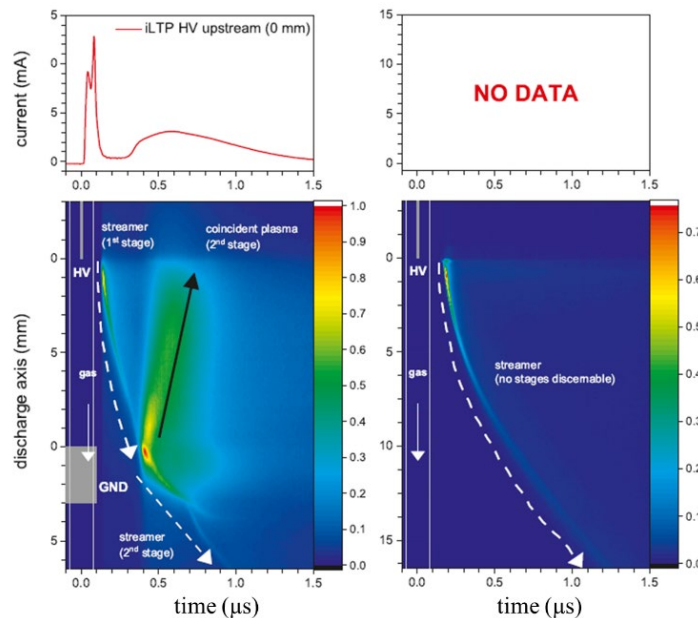


Figure 2.8: Emission measurements of the iLTP configuration and F μ TP. The top row shows the measured current. Adapted with permission from [62], Copyright 2021 Elsevier.

Chapter 2 Fundamentals

Compared to discharge in iLTP, only one discharge development is included. It starts at the HV electrode and propagates towards the capillary exit. The reduction of plasma development to only one discharge also implies that it functions on a basic and easy to interpret mechanism. This could be beneficial for further exploration of soft ionisation mechanisms and potentially provide additional modelling approaches to support such explorations. On the basis of the thorough characterisation of the preceding capillary DBDI, LTP and iLTP, a new design, the flexible micro-tube plasma (F μ TP), was reported as a small footprint and versatile ionisation source [9]. The evolution of electrode configurations from LTP to iLTP and subsequently to F μ TP is simply illustrated in Figure 2.9.

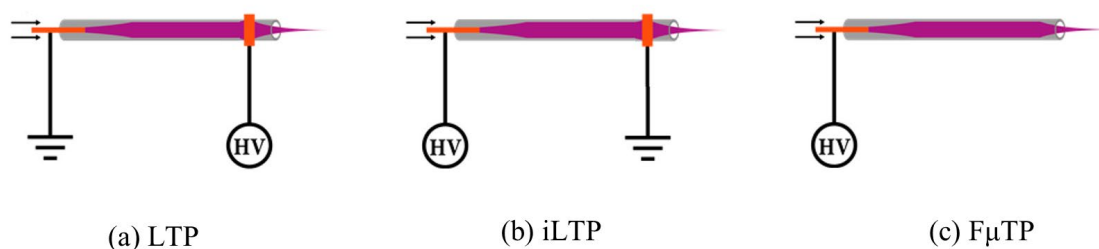


Figure 2.9: The electrode configurations of (a) LTP, (b) iLTP and (c) F μ TP.

2.1.4 F μ TP Ionisation Source

The schematic diagram of the F μ TP ionisation source is shown in Figure 2.10. A flexible polyimide-coated fused silica capillary is used for the construction of the channel of the F μ TP ionisation source with inner and outer diameters of 250 μm and 350 μm , respectively. This small diameter allows low gas flows below 100 standard cubic centimetres per minute (sccm) at ambient pressure.

The flexible nature of the fused silica capillary makes the F μ TP very robust and easy to handle. This facilitates a good coupling of the plasma source to analytical instruments. This flexibility further improves the resistance of F μ TP to accidental breakage and similar damage.

A tungsten wire with a diameter of 100 μm is inserted into the capillary and acts as an electrode. This provides great safety. No physical counter electrode is present in this design. The volume between the electrode tip and the capillary outlet forms the discharge column.

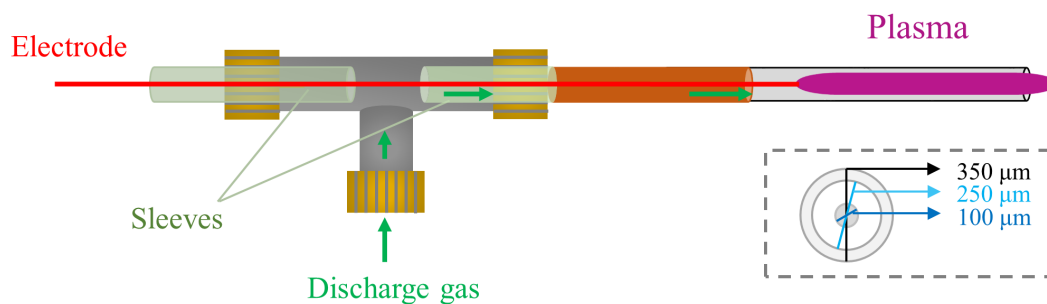


Figure 2.10: Schematic diagram of a F μ TP ionisation source. Inset: Sectional view of a F μ TP ionisation source.

The length of the discharge column can be adjusted to meet a specific application by changing the relative positions of the electrode tip and the capillary outlet with ease. In addition, direct discharge between the electrode and the mass spectrometer inlet is avoided due to the small dimensions of the discharge capillary.

In addition to noble gases, nitrogen or air can also be used as a discharge gas. The discharge can be ignited by applying a square wave power generator with a frequency of 5 kHz to 50 kHz in multiples of thousands of volts.

The F μ TP is a novel, user-friendly, and effective ionisation source for analytical applications such as MS and IMS. It could give superior analytical performance as a soft ionisation source [9]. Nonpolar and low-polar compounds can be efficiently ionised [63-68]. Investigations have been conducted into the combination with a secondary ionisation source concerning analytical performance, such as with an ESI and a paper spray source [69,70]. By employing such a combination, it becomes feasible to successfully analyze low-polarity compounds present in complex biological samples, while simultaneously enhancing the number of compounds detectable within a single measurement. With the flexible and compact design, the F μ TP is well suited for miniaturised arrangements.

Although the F μ TP was proposed and developed through detailed studies of DBD and has been successfully employed in numerous analytical applications as a soft ionisation source with good analytical performance, its discharge mechanism is not yet fully understood. A comprehensive understanding of the discharge mechanism is crucial to advance the exploration of its potential applications. Furthermore, it provides valuable insights into the soft ionisation mechanisms of plasma-based ionisation sources. This thesis systematically investigates discharge mechanism of the F μ TP.

2.2. Optical Emission Spectroscopy

Optical emission spectroscopy (OES) is a reliable analytical technique used for the identification and quantification of elements in a sample by analysing the light emitted from the excited sample [71]. The first definitive application of OES was the use of a prism to disperse light from a flame [72]. It demonstrated that each chemical element emits light at specific characteristic wavelengths. The work was pivotal in the identification of elements on the basis of their emission spectra and marked the beginning of emission spectroscopy as an analytical tool.

OES is also a diagnostic tool for studying the physical and chemical properties of plasmas [73,74]. The critical information about plasma properties, including composition, temperature, density, etc. can be gathered by analysing the light emitted by excited species in a plasma.

Modern OES systems incorporate advanced techniques such as temporally-spatially resolved OES, which can capture transient phenomena in pulsed plasmas. It provides noninvasive, real-time monitoring of the plasma processes. This provides insights into the discharge mechanisms. In the following sections, the fundamentals of emission and the spectrographs used for plasma diagnostics in this thesis are described in detail.

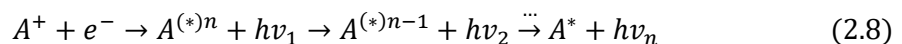
2.2.1 Optical Emission

Optical emission is the process by which matter, such as atoms or molecules, releases energy in the form of light. The emission that occurs primarily involves the excitation and / or ionisation of a particle to an excited and / or ionised state. This is followed by a relaxation from an upper energy state to a lower energy state, releasing a photon [73].

For excited particles, the emission process can be expressed as Equation 2.7.



For ions, the recombination radiation is expressed as Equation 2.8.



The energy carried off by the photon is equal to the energy difference between two states. The frequency of light emitted is a function of the energy of the transition, which is given by Equation 2.9 [75].

2.2. Optical Emission Spectroscopy

$$E_{\text{photon}} = h\nu \quad (2.9)$$

Where E_{photon} is the photon energy, ν is its frequency, and h is the Planck constant.

Since the frequency ν , wavelength λ , and the speed of light c are related by $\nu = c\lambda^{-1}$ [76], the relation between the photon energy and the wavelength can be expressed as Equation 2.10.

$$E_{\text{photon}} = hc\lambda^{-1} \quad (2.10)$$

For each atom or molecule, there are many possible transitions. Each transition has a specific energy difference. This collection of different transitions leads to different radiated wavelengths. These wavelengths make up an emission spectrum. Each particle produces a unique emission spectrum that serves as its “fingerprint”. In a complex system, such as a plasma, the emission spectra of all constituent particles compose the unique fingerprint of the plasma.

2.2.2 USB 4000 Spectrometer

An USB 4000 spectrometer (Ocean Optics, Dunedin, USA) is one of the spectrometers used in this work. It is utilised to explore the types of reactive species in plasmas. An optical fibre is connected to the USB 4000 spectrometer. The components of the spectrometer can be found in its manual [77].

One side of the optical fibre is placed close to the light source to be characterised. Through the slit of the spectrometer, the collected light passes through the filter before entering the optical bench. The filter predetermines the detectable range of wavelengths to a specific region by restricting optical radiation [77]. Afterwards, the light is collimated and reflected by a collimating mirror, which converts the incident divergent beam into a parallel beam. Figure 2.11 a shows the process of how light passes through the optical bench. A parallel beam is directed onto the diffraction grating. The diffraction grating decomposes light into its constituent wavelengths, which can be given by Equation 2.11 [78],

$$m\lambda = d(\sin \alpha + \sin \beta) \quad (2.11)$$

where m is an integer value used to describe the diffraction order, λ is the wavelength and d is the spacing between the grooves on the grating, known as the grating constant, α is the incident angle of the light and β is the diffracted angle of the wavelengths leaving the grating. This is shown in Figure 2.11 b.

Chapter 2 Fundamentals

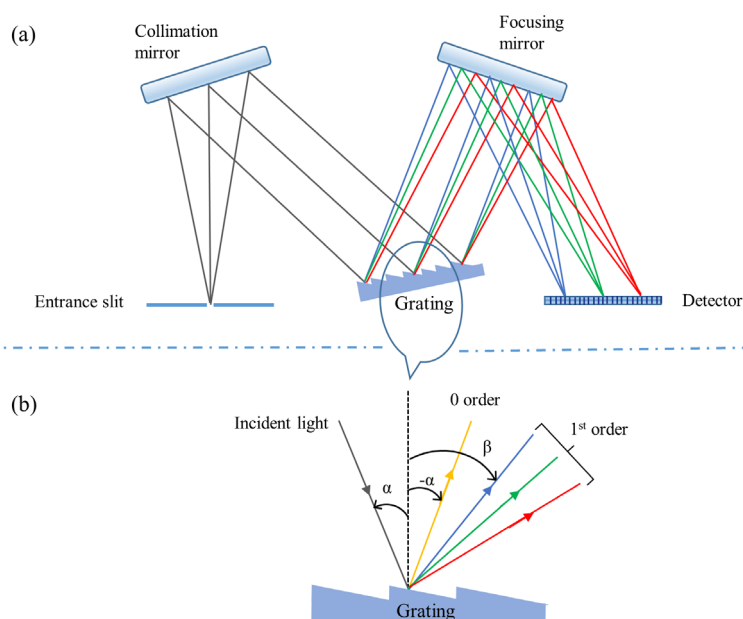


Figure 2.11: (a) The diagram of how light passes through the optical bench. (b) The decomposition of light by a diffraction grating. The diffraction of “0 order” represents some light reflects directly off the grating, other parts of the incident light are diffracted into 1st order based on wavelength.

Gratings are usually specified in terms of their groove densities, namely the number of grooves per unit length, expressed in grooves per millimetre. Typically, a grating contains a few tens of grooves per millimetre or up to thousands of grooves per millimetre. This predetermines the optical resolution of the spectrometer. In addition, the wavelength range covered by a grating is also dependent on the groove density, which is thus another key parameter that determines the detectable wavelength region besides the filter.

The grating directs the diffracted light to the focusing mirror. This mirror focusses the separated wavelengths and directs the first-order (1st) spectra onto the detector plane. Each wavelength is imaged onto a different set of pixels, which allows the device to determine the number of wavelengths in the broadband light source and the abundance of each wavelength. The detector responds to the wavelengths of the light that strike it and converts the optical signal into a digital signal. A common detector is a linear silicon charge coupled device (CCD) array. In this spectrometer, the grating is fixed so that all constituent wavelengths of incident light within the detection range are simultaneously displayed on the detector and detected. The integration time is an important parameter related to the emission intensity of the species. The intensity is proportional to the integration time before the emission intensity saturates.

2.2. Optical Emission Spectroscopy

Through the scope of this thesis, plasmas serve as light sources. A pulsed square wave power generator with a frequency of 20 kHz is applied to generate plasmas. With the USB 4000 spectrometer, the integration time is in the range of milliseconds (ms). Integral spectra are acquired by this spectrometer. This means that the total spectra of thousands of discharge cycles are collected for a given integration time. Furthermore, the acquired information on the emission from a plasma includes the contribution from both the positive and negative half cycles. It is not possible to provide information on the generation and propagation of each species at different moments and at corresponding positions. For this reason, another spectrograph, a Kymera Adaptive Focus Imaging Spectrograph (Kymera 193i, Andor Technology, Belfast, UK) with a fast intensified charge coupled device detector (ICCD camera, Andor DH 720 18F-03, Andor Technology, Belfast, UK), is used to measure the temporally and spatially resolved emission of the reactive species.

2.2.3 Kymera Adaptive Focus Imaging Spectrograph

The temporally and spatially resolved emission spectroscopy is another significant method for the characterisation of discharge properties. This method can provide two-dimensional information of the plasma propagation with a nanosecond and micrometre resolution without disturbing the plasma itself. The main components of this technique used in this thesis include a convex lens, a Kymera Adaptive Focus Imaging Spectrograph, and an ICCD camera. The Kymera Adaptive Focus Imaging Spectrograph is simplified as the Kymera Spectrograph in the following descriptions.

Figure 2.12 illustrates the process by which the incoming light is converged, focused, guided, and shaped by a convex lens before entering the entrance slit of the Kymera Spectrograph. The lens aligns the light path to reduce dispersion and ensures that all relevant spectral features are captured by the Kymera Spectrograph. The optical bench of the Kymera Spectrograph consists of two mirrors and a diffraction grating. The spectroscopic principle is similar to that of the USB 4000 spectrometer, namely, the light passed through the entrance slit is collimated and reflected by a collimating mirror onto the diffraction grating. The grating disperses the incoming light into its constituent wavelengths and reflects them onto a focusing mirror. The focusing mirror focusses these wavelengths onto the detector (see Figure 2.11). It is worth noting that the grating in this system is rotatable, which is favourable for measuring individual wavelength by only adjusting the central wavelength.

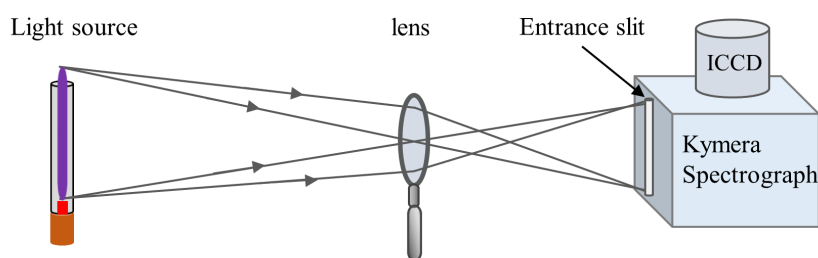


Figure 2.12: Schematic of the optical setup for coupling a light source to a Kymera spectrograph equipped with an ICCD detector. The light emitted by the source is guided and focused by a convex lens onto the entrance slit of the Kymera Spectrograph.

An ICCD camera is attached to the Kymera Spectrograph as the detector. An ICCD combines optical intensification technology with a CCD. The optical window and photocathode, microchannel plate, and CCD are the main components. Light entering through the optical window strikes the photocathode, which converts incoming photons into primary electrons. Primary electrons are accelerated toward the microchannel plate. Inside the microchannel plate, these electrons undergo a cascade of secondary electron production, amplifying the original signal. The amplified electron signal strikes a phosphor screen, where converts the electrons back into an intensified light signal. The light signal is focused onto the CCD via the fibre optical coupler. The CCD chip collects photons as a two-dimensional pixel array and converts the optical signal into an electrical signal, forming a charge packet proportional to the intensity of the light. The charges accumulated in the CCD pixels are digitised and edited as a digital signal.

2.3 Data Acquisition and Processing

2.3.1 Data Acquisition

For the collection of integral spectra, the optical fibre is installed close to the light source. The detailed coordinates of the optical fibre vary depending on the demands. The integration time varies according to the emission intensity of the light. The detailed parameters used in this thesis will be given in the corresponding sections. Since the integration time is related to the emission intensity, the dark background at the set integration time should be subtracted before recording the signal.

2.3 Data Acquisition and Processing

For the temporally and spatially resolved emission spectra, the kinetic series acquisition mode and the external trigger mode are chosen from the operating software. A homemade square wave generator is applied to ignite a plasma. An external signal generator (Musashino, Japan) is applied to give two simultaneous signals used as trigger signals for the power generator and the ICCD detector, respectively. This is shown in Figure 2.13.

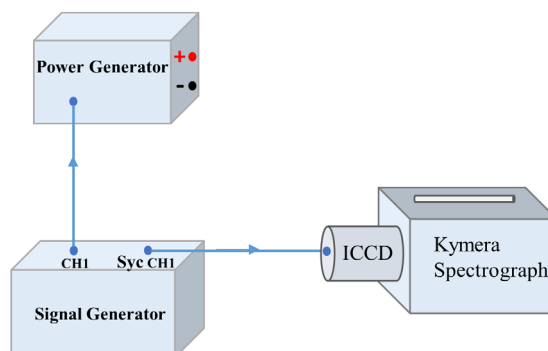


Figure 2.13: Schematic diagram of synchronous a power generator and an ICCD detector. The signal generator provides synchronized trigger signals (CH1 and Sync CH1) to the power generator and ICCD, ensuring precise timing control.

This signal activates the Digital Delay Generator (DDGTM), which is one of the items contained in the detector. So DDGTM can control the intensifier tube for gating applications. The DDGTM itself is activated by the rising edge of the incoming trigger signal. Once DDGTM is activated, the intensifier tube photocathode will be switched on and start acquiring data. The DDGTM region allows to set up parameters that are used to control the intensifier tube operation, including gate pulse delay and gate pulse width.

Even a simultaneous trigger signal is applied to the square wave generator, the generator shows a delay of 900 ns compared to the trigger signal or the ICCD gate as shown in Figure 2.14. This is caused by external factors such as cable lengths and generator response. In order to synchronise the opening of the intensifier tube with the electrical pulse, a gate pulse delay can be introduced into the system by entering the required delay time. This will postpone the time that the intensifier tube is switched on. In this context, a gate pulse delay of 900 ns is configured to achieve synchronization, as depicted in Figure 2.14 (bottom).

In order to examine plasma development within a single discharge cycle, the gate delay width is configured to 900 ns for the positive half cycle and 25900 ns for the negative half cycle, with a frequency of 20 kHz being utilised.

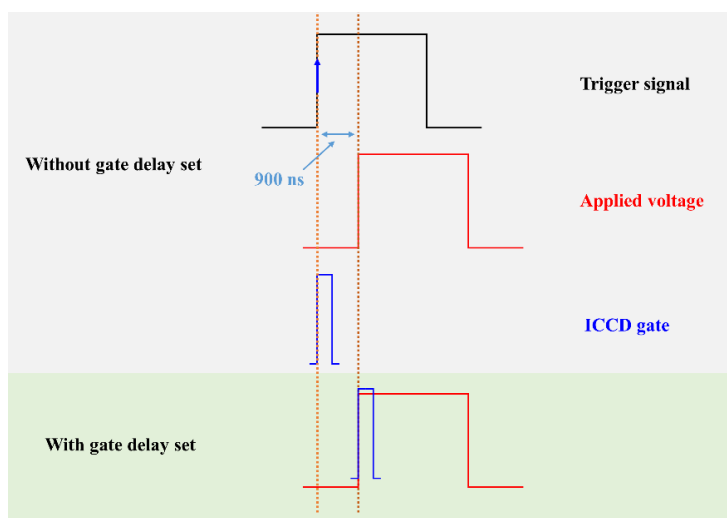


Figure 2.14: The delay among power generator, ICCD gate and trigger signal without delay set (top) and with gate delay set (bottom).

The intensifier tube photocathode has been on for a certain time. This time is determined by the user. Until the intensifier tube receives the off pulse from the DDG™ to instruct it to switch off. The difference in time between the intensity tube switching on and off is called the gate pulse width. The optical signal falls on the CCD sensor during this time. The temporal resolution is predetermined by the gate pulse width.

In the kinetic series acquisition mode, a temporal sequence of signal scans is capable of being sequentially acquired at a predetermined gate pulse width through the establishment of a gate step width. The acquisition sequence scenarios are shown in Figure 2.15.

By setting the gate step width, the moment at which the intensifier tube is switched on can be shifted. Therefore, an additional cumulative delay will be created for the later acquisition. For example, for the second acquisition, a delay of one gate step width is added to the gate pulse delay. For the third acquisition, delays of two step widths are added to the gate pulse delay, and so on.

Therefore, during the positive half cycle, the moment at which the intensifier tube is switched on, as a function of the acquisition sequence, can be expressed as Equation 2.12,

$$gate\ step\ width * (x - 1) = t \quad (2.12)$$

where x is an integer value used to describe the acquisition sequence and t is the moment of the intensifier tube to be turned on.

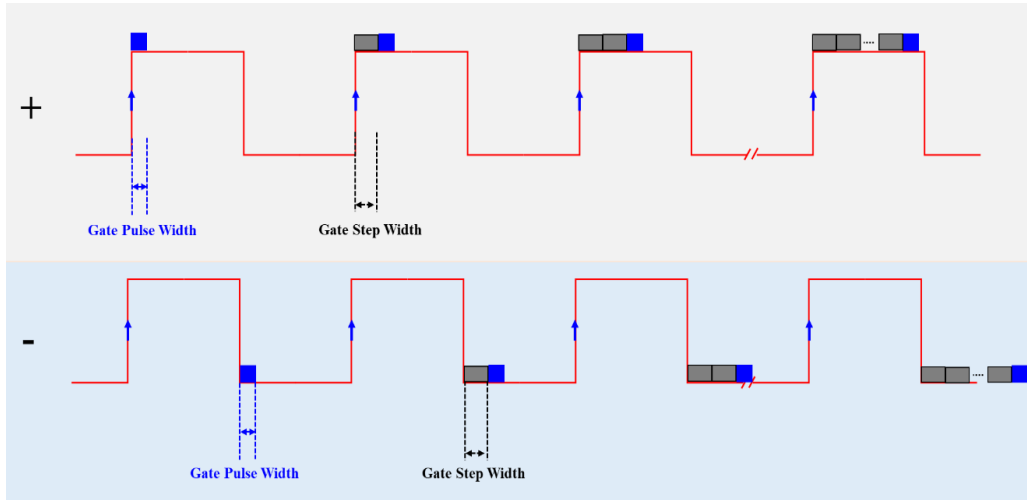


Figure 2.15: Acquisition sequence of ICCD camera during positive (top) as well as negative half cycle (bottom). The blue square represents for the gate pulse width and the dark gray rectangle is for the gate step width.

For the measurements during negative discharge half cycle, gate delay width is set to 25900 ns, the function can be given as Equation 2.13.

$$\text{gate step width} * (x - 1) + 25000 \text{ ns} = t \quad (2.13)$$

On the basis of these formulas, the moment in a discharge cycle corresponding to the acquisition sequence can be easily calculated and vice versa.

The gate step width should be set to at least as long as or even larger than the gate pulse width to avoid repeated acquisition during each gate pulse width frame. The time resolution achieved for measurement is therefore determined by the gate step width as well as the gate pulse width. The settings usually depend on the time period being investigated. For a long discharge frame such as 6 - 8 μs , a full screening of this time period at a temporal resolution of 5 ns (the gate pulse width and gate step width are both set to 5 ns) means that 1200 - 1600 individual images have to be taken. This is a challenge for the camera and data analysis software. In addition, considering the emission intensity of the wavelength and the long exposure times that may be required, a full time period with 1200 - 1600 individual images for the measurement of just one wavelength can take up to several hours. That is not very practical in actual measurement. One solution is to increase the gate step width to reduce the individual images and therefore the total measurement time. For a short discharge frame, such as 1 - 2 μs , a temporal resolution of 5 ns is reasonable for recording the propagation of plasma with taking 200 - 400 individual images. By

Chapter 2 Fundamentals

changing the central wavelength in the operating software (Andor Solis), the propagation of various wavelengths can be recorded.

2.3.2 Data Processing

The data acquired with the Ocean Optics software application (Spectra Suite) is in the form of Excel, which can be plotted directly. The raw data acquired with Andor Solis are not able to get direct information on the plasma ignition and development. Therefore, several data processing steps need to be performed to form a contour of these data, which are summarised in Figure 2.16 and will be described in the upcoming paragraphs [79].

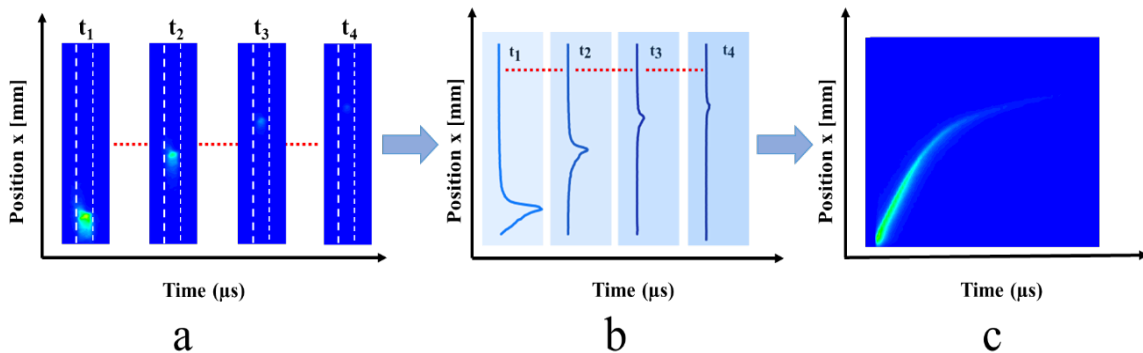


Figure 2.16: Data processing procedure for the spatial and temporal development. a. raw data; b. averaged data; c. contour data. The raw data are acquired by an ICCD camera. The raw data are extracted and averaged by a contour plot analyzer. The contour data is drawn by the commercial Origin software. Adapted with the permission from [79], Copyright 2021 Elsevier.

Raw data at a few selected instants of time ($t_1 - t_4$) are used as an example to illustrate. As shown in Figure 2.16 a, the images show the entire raw data at these four moments, where the regions between the two white dashed lines are the plasma signals to be processed, and the rest is the background signal. The plasma signal is extracted and averaged by transferring the data set shown in Figure 2.16 a to a contour plot analyser, which is a self-programmed software. This procedure reduces the CCD chip dataset for each acquisition to a single data row. It contains only the position pixels and the corresponding emission intensities of the discharge at a certain moment. These 1D data rows along the capillary at corresponding moments can be drawn as line plots, as shown in Figure 2.16 b. Afterward, according to the acquisition sequence, transferring all these one-dimensional data rows to contour form, drawing two-dimensional colour plots using Origin software, which will obtain the spatial and temporal plasma propagation as presented in Figure 2.16 c.

2.4 Gases

Various noble gases such as *He*, *Ne*, *Ar*, *Kr* and *Xe*, as well as gas mixtures such as *He* mixed with N_2 and *Ar* mixed with propane are interesting in this thesis. The purity of *He*, *Ne*, *Ar*, *Kr* and *Xe* is 99.999% (5.0), propane is 99.95% (3.5), and N_2 is 99.9999% (6.0). They were purchased from Westfalen Austria GmbH, Germany.

A gas mixture of *He* with 2000 parts per million (ppm) N_2 and a gas mixture of *Ar* with 10000 ppm propane are prepared in-house using an evacuated gas cylinder. First, the calculated amount of N_2 or propane is injected into the empty cylinder. The cylinder is then filled with *He* 5.0 or *Ar* 5.0 until the pressure reaches 5 bar, yielding the gas mixtures. By mixing the gas mixture and *He* 5.0, any specific concentration of N_2 in *He* between 3 ppm and 2000 ppm can be accessed. Similarly, by mixing the gas mixture and *Ar* 5.0, any specific concentration of propane in *Ar* between 100 ppm and 10000 ppm can also be obtained. The final concentration and additional parameters will be given in the respective sections.

The gas is introduced by a mass flow controller (ALICAT, Tucson, USA) to ensure a stable and controllable gas flow rate. A stable flow rate is essential for the F μ TP ionisation source, as the flow rate has an influence on the propagation of the plasma. The mass flow mode is chosen because in this case the flow controller always supplies the same amount of noble gas atoms per unit time, regardless of the atomic weight. This is beneficial for the investigation of various plasmas such as a *He*-, *Ne*-, *Ar*-, *Kr*-, *Xe*-F μ TP and an *Ar*-propane-plasma. The flow rate of the discharge gas is 50 sccm.

He is used as a diagnosis gas to replace ambient air. The flow rate of a diagnosis gas varies in different measurements. Details will be given in the corresponding sections.

F μ TP Ionisation Source: A Dielectric Guided Discharge ^{P1}

A comprehensive elucidation of the excitation and ionisation mechanisms of the F μ TP ionisation source, which is beneficial and essential for advancing the understanding of the soft ionisation mechanism in the field of analytical chemistry, has not yet been accomplished. Nevertheless, the F μ TP source has been used for several analytical applications as a soft ionisation source with good analytical performance without such knowledge [63-70]. In this sense, it is an ideal starting point for systematic investigation. From this chapter onwards, the discharge mechanism of the F μ TP source will be investigated.

Analysing the emission spectra of plasma offers an effective method to obtain information regarding the propagation of plasma, and thus constitute an essential component of the investigative efforts. A well-defined physical and chemical stable discharge volume

P1: Substantial parts of this chapter are based on the previously published article: Optical characterisation of miniature flexible micro-tube plasma (F μ TP) ionisation source: A dielectric guided discharge by **Tian C**, Ahlmann N, Brandt S, Franzke J, Niu G; it was first published in *Spectrochimica Acta Part B: Atomic Spectroscopy*, 2021 as an open access article and is licensed under Creative Commons Attribution 4.0 International License (<https://creativecommons.org/licenses/by-nc-nd/4.0/>).

Chapter 3 *F μ TP Ionisation Source: A Dielectric Guided Discharge*

facilitates the acquisition of exact information about the plasma [80-82]. For this, it is desirable to keep the plasma completely in the capillary without interference from the surrounding environment. In this chapter, the length of discharge column is 30 mm. The plasma can be completely confined within the capillary for given operation parameters.

He will be used as a discharge gas to investigate the excitation and ionisation mechanisms in one discharge cycle. The integral spectra of a *He* plasma will be presented and discussed. After the identification of the reactive species in a typical *He* plasma spectrum, several species will be chosen on the basis of their importance in the soft ionisation to investigate their generation and propagation in both positive and negative half cycles in detail. The results obtained will be systematically compared not only between different species but also at different discharge half cycles. Furthermore, the discharge processes of *F μ TP* will be compared to those of the capillary DBDI and LTP probe. Finally, the effect of N_2 concentration on discharge and N_2^+ generation will be experimentally explored by changing the concentration of N_2 in discharge gas mixtures. The data shown in this chapter have been published in 2021 [79].

3.1 Experimental Arrangement

The experimental arrangement employed in this chapter is shown in Figure 3.1. The length between the electrode and the end of the capillary is 30 mm, which is the discharge column of the *F μ TP*. *He* 5.0 with a flow rate of 50 sccm is introduced as discharge gas. A home-made square wave HV generator is directly connected to the tungsten electrode to supply power. The HV generator delivers a maximum peak-to-peak voltage of 3.5 kV with a sharp rising edge (50 ns at 1.7 kV). The applied positive bias voltage is kept at 2.3 kV with a frequency of 20 kHz and duty cycle of 50:50.

Under these experimental conditions, the plasma is completely kept within the capillary. This provides a clean environment for plasma generation and propagation. Ambient air diffusion occurs only in the vicinity of the capillary outlet under the given dimension of the *F μ TP* capillary and the flow rate of the discharge gas.

For the measurements by optical emission spectroscopy, the coating of the capillary in the discharge region has to be stripped off to offer a transparent channel. In order to make the experiment more accurate, it is advisable to strip at least 2 - 3 mm of the coating beyond the length of the discharge column. For full spectral information of the reactive species in

3.2 Overview of Species in a He-F μ TP

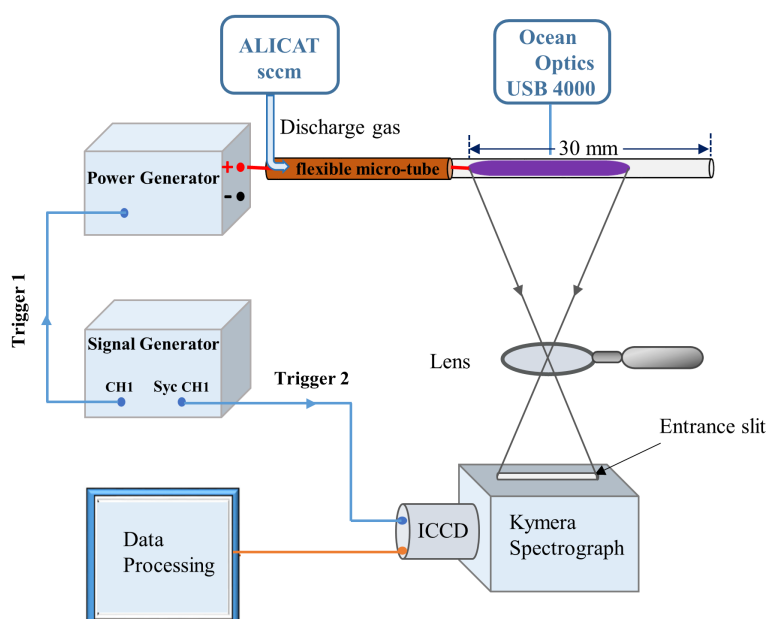


Figure 3.1: Experimental arrangement for the characterisation of the plasmas along the discharge capillary. Adapted with the permission from [79], Copyright 2021 Elsevier.

plasmas, an USB 4000 spectrometer with a wavelength range of 300 - 900 nm is used. The resolution of this spectrometer is 1.9 nm. The optical fibre is installed perpendicular to the discharge capillary at a distance of 1 mm. Detailed coordinates of the optical fibre along the capillary axis will be given in the respective sections. The integration time is 100 ms.

For the temporally and spatially resolved optical emission information of plasmas, a Kymera Spectrograph with ICCD camera is utilised. A quartz convex lens with a focal length of 75 mm lens is placed between the plasma to be measured and the entrance slit of the Kymera Spectrograph. The entrance slit is 200 μ m. The object distance and image distance are around 400 mm and 100 mm, respectively. A diffraction grating comprising 1200 grooves per millimetre is selected. The resolution of this spectrograph is 0.21 nm. In order to gain an adequate emission intensity and an appropriate acquisition time, the gates and step widths of 50 ns and 100 ns are chosen, respectively. Otherwise, a specified description will be given.

3.2 Overview of Species in a He-F μ TP

The initial study of this thesis is an exploration of reactive species in a He-F μ TP. In general, the identification of reactive species in a plasma can provide general information about the

Chapter 3 *F μ TP Ionisation Source: A Dielectric Guided Discharge*

type of species. This facilitates further plasma diagnostics and enhances understanding of soft ionisation mechanisms.

Figure 3.2 a shows the spectra of a *He*- $F\mu$ TP collected by the USB 4000 spectrometer at the electrode tip. The observed species include excited OH, excited N_2 (second positive system, $N_2 C^3\Pi_u \rightarrow N_2 B^3\Pi_g$), ionised N_2 (first negative system $N_2^+ B^2\Sigma_u^+ \rightarrow N_2^+ X^2\Sigma_g$), excited atomic *He* and excited atomic O. Since the diffusion of surrounding air into the capillary takes place only in the vicinity of the capillary exit, all species, except for excited atomic *He*, result from impurities in the discharge gas (*He* 5.0). It contains 3 ppm N_2 , 2 ppm O_2 , and 3 ppm H_2O . In this sense, all species observed in the spectra originate from the discharge gas. These species compose a spectrum of a *He*- $F\mu$ TP, with the highest abundance of N_2^+ 391 nm. It is worth noting that due to the resolution of the spectrometers used, the wavelengths mentioned throughout the text and in the Figures will only be given as integer values.

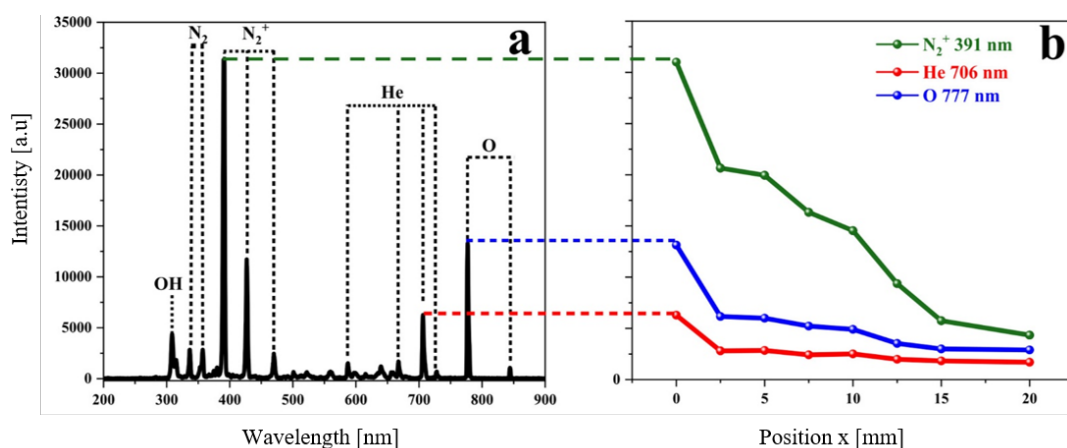


Figure 3.2: (a) The spectra of a *He* plasma measured by an USB 4000 spectrometer at the electrode end. The discharge gas is *He* 5.0 with a gas flow of 50 sccm. The integration time is 100 ms. (b) Progression of the signal intensities of the chosen emission species along the discharge capillary. Adapted with the permission from [79], Copyright 2021 Elsevier.

The emission spectra at different positions along the discharge capillary were also collected by changing the location of the optical fibre. The emission intensities of N_2^+ 391 nm, *He* 706 nm and O 777 nm were picked up from these spectra and plotted. This is shown in Figure 3.2 b, where 0 mm represents the location of the electrode tip. The measured intensities are decreasing with the increase in distance, indicating that the potential and thus the electric field are decreasing along the capillary.

3.3 Temporally and Spatially Resolved Emission Spectra

The temporal and spatial emission spectra of species are carried out by the Kymera Spectrograph with an ICCD camera. The results acquired are given and discussed in the following sections.

3.3 Temporally and Spatially Resolved Emission Spectra

3.3.1 Propagation of the Whole Emission

Figure 3.3 shows the temporal and spatial colour plots of the whole emission measured in a *He*-F μ TP in the positive and negative half cycles. In this thesis, the “whole emission” refers as to the integral emission of all reactive species included in a certain plasma that the spectrometer can measure. The position of 0 mm along the discharge axis represents the location of the electrode tip.

A discharge development is observed during the positive half cycle. It is ignited at the tip of the electrode and propagates toward the end of the capillary with time, as indicated by a white dashed arrow in Figure 3.3 (a). During this half cycle, electrons are attracted by the positive potential applied to the electrode and accelerated in the electric field. The energetic electrons collide with the neutral *He* atoms and other impurity molecules, leading to their excitation and ionisation. With the excitation and ionisation propagating forward, a portion

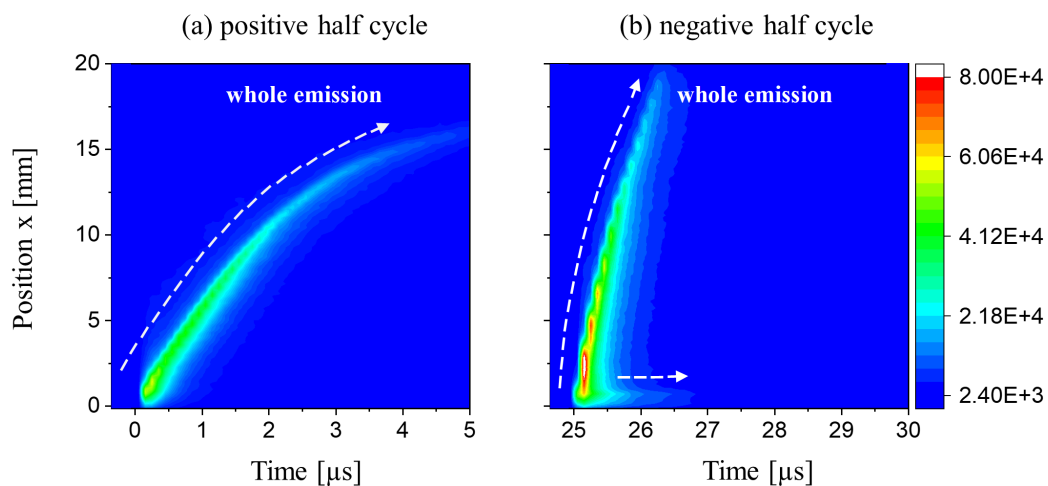


Figure 3.3: Spatial and temporal development of the whole emission in one discharge cycle, (a) positive half cycle and (b) negative half cycle. The discharge gas is *He* 5.0 with a gas flow of 50 sccm. The dashed arrows show the development processes. Adapted with the permission from [79], Copyright 2021 Elsevier.

Chapter 3 F μ TP Ionisation Source: A Dielectric Guided Discharge

of the positive ions attach to the inner wall of the capillary. This results in the formation of charge rings that surround the inner wall step by step. As a result of the absence of the counter electrode, only one electric field from the positive potential to the end of the capillary is created. This electric field dominates the entire discharge process in the positive half cycle.

The negative half cycle begins after 25 μ s. During this half cycle, two discharge developments are observed. One is from the electrode tip towards the end of the capillary and the other remains in the vicinity of the electrode tip, as indicated by white dashed arrows in Figure 3.3 (b). Since the positive bias voltage is applied in this chapter, the metal electrode is grounded during the negative half cycle. The applied square wave voltage is shown in Figure A.1 of the Appendix. The residual charge rings act as a transient “virtual positive electrode”. In this manner, an opposite electric field is created in comparison to that in the positive half cycle. Electrons are now attracted by the “virtual positive electrode”.

A question may arise as to why, despite the electric field is in opposite direction, one of the discharges progresses in the same direction as observed during the positive half cycle, specifically from the electrode to the capillary end. One possible explanation is as follows. As the applied voltage decreases from 2.3 kV to 0.0 kV, the voltage difference between the applied voltage to the electrode and the “virtual positive electrode” is getting larger and larger. Once the voltage difference exceeds the breakdown voltage of a gas, a plasma is ignited. The excited species, positive ions, negative ions, and electrons are generated in the vicinity of the electrode. Electrons are attracted by the “virtual positive electrode” and move away from the metal electrode. In the meantime, positive ions tend to stay near the metal electrode due to the high mass and repulsion of the “virtual positive electrode”. As a result, a cloud of positive ions (potential) in the vicinity of the metal electrode and thus a new electric field is created. The direction of the new electric field is from this potential to the end of the capillary. Such a new electric field dominates the subsequent development of the plasma along the capillary in the negative half cycle. On the basis of the explanation above, the dielectric barrier acts as a charge holder, and the plasma generation in negative half cycle is guided by the charges attached on the inner surface. Therefore, the discharge of the F μ TP can be considered as a dielectric guided discharge.

In addition, another discharge process takes place in the vicinity of the metal electrode in the negative half cycle. It lasts almost the entire plasma propagation process, as indicated by a horizontal arrow in Figure 3.3 (b). This emission might be ascribed to a negative glow discharge caused by secondary electron emission [83,84]. Due to secondary electron

3.3 Temporally and Spatially Resolved Emission Spectra

emission in the negative half cycle, more electrons are accelerated in the electric field. Consequently, there is an increase in collisions between energetic electrons and both discharge gas atoms and impurity molecules during this half cycle, thus leading to a more intense discharge.

To give a direct and overall expression that how the plasma develops step by step during both half cycles, the raw data at different instants of time without any averaging are extracted and plotted, respectively. Figure 3.4 (a) shows the propagation of the whole emission at selected instants of time during the positive half cycle and 3.4 (b) for the negative half cycle. As can be seen in the two subplots, the propagation of the whole emission differs in both half cycles.

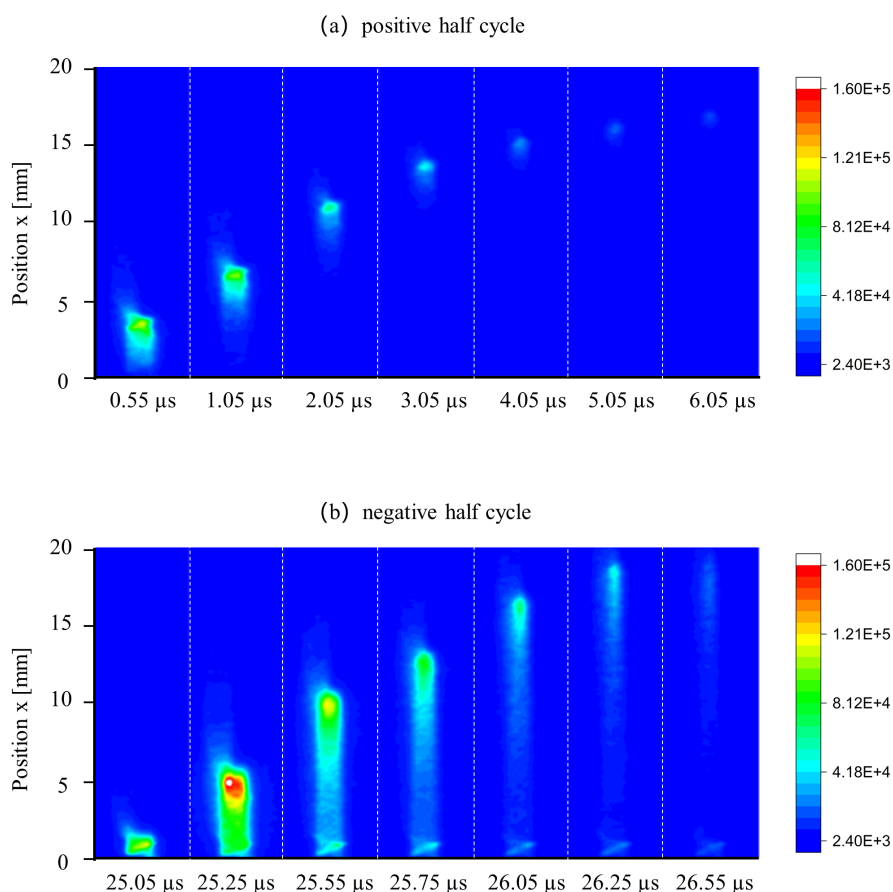


Figure 3.4: Spatial and temporal propagation of the whole emission at different instants of time during the positive (a) and negative (b) half cycle. The inserted numbers are the corresponding instants of time of the plasma propagation along the discharge capillary. The discharge gas is *He* 5.0 with a gas flow of 50 sccm. Adapted with the permission from [79], Copyright 2021 Elsevier.

Chapter 3 *F μ TP Ionisation Source: A Dielectric Guided Discharge*

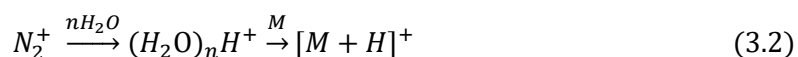
Plasma propagation is more discrete in the positive half cycle while it is more continuous in the negative one. This finding is similar to the case where the plasma jet is maintained by the positive and negative polarity voltages, respectively [85]. In addition, the plasma development along the capillary not only lasts much longer time (6.05 μ s) in the positive half cycle than in the negative one (1.55 μ s, from 25.00 μ s to 26.55 μ s) but also shows a lower emission intensity. These can also be seen in Figure 3.3. These phenomena may result from a stronger discharge in the negative half cycle compared to that in the positive half cycle. A more detailed explanation will be provided in a later section (see Section 4.2.6).

As stated in the chapter **Fundamentals** (see Section 2.1.3), three discharge processes are observed in capillary DBDI and LTP sources in the positive half cycle. The early plasma and the coincident plasma are confined in the capillary between two electrodes, and the plasma jet extends beyond the discharge capillary outlet. In contrast, due to the absence of the ground electrode, no early plasma and coincident plasma are formed in the $F\mu$ TP. Only one discharge development occurs in the positive half cycle. It starts at the HV electrode and propagates forward along the capillary. This may be one of the reasons why the analytical performance of $F\mu$ TP is superior to that of DBDI and LTP [56].

3.3.2 Propagation of Selected Species

Since the whole emission encompasses all reactive species detectable by the given spectrometer, the propagation behaviour of the whole emission can only suggest a trend in the development of an individual specie, rather than represents it with certainty. Reactive species play an important role in various fields of application. Therefore, research on the excitation and ionisation processes of specific species can better direct and expand the applications of the plasma.

Focusing on analytical chemistry, in particular when plasma is used as a soft ionisation source for MS or IMS, the species of *He* metastables (He^M) and N_2^+ are considered to play an essential role for the soft ionisation process of an analyte *M*. The widely accepted process is summarised in Equations 3.1 to 3.3.



3.3 Temporally and Spatially Resolved Emission Spectra

Typically, He^M states with energies of 19.8 eV and 20.9 eV are higher than the $N_2^+ B^2\Sigma_u^+$ state with 18.8 eV. This allows the energy to be transferred from He^M to N_2 molecules in the ground state, generating $N_2^+ B^2\Sigma_u^+$. By the decay of $N_2^+ B^2\Sigma_u^+$, $N_2^+ X^2\Sigma_g^+$ state with 15.6 eV is populated. It is generally accepted that $N_2^+ X^2\Sigma_g^+$ states ionise H_2O molecules with an ionisation energy of 12.6 eV, producing protonated water clusters, although there is an energy difference of 3.0 eV between the $N_2^+ X^2\Sigma_g^+$ state and the ionisation level of H_2O . Finally, protonated analyte ions are generated through proton transfer reactions. It is worth noting that the probability of an effective collision between two substances is strongly related to the energy difference. A large energy difference reduces the probability [86].

In this series of reactions, O_2 does not seem to be involved. However, it was indicated that no protonated water clusters and protonated analyte ions were measured by MS measurements when only N_2 was used as an atmosphere gas in a controlled system. With a slight increase in O_2 concentration in the atmosphere system, the signals have a significant increase [68]. This means that O_2 also participates in the generation of protonated water clusters, which could be O_2^+ .

Figure 3.5 shows the energy states of N_2^+ , O_2^+ and H_2O^+ . The states of the first negative systems (FNS) of N_2^+ and O_2^+ are marked by the red rectangles in their corresponding oscillator systems, and the states of the second negative system (SNS) of O_2^+ are marked by the green rectangles [87,88]. It can be seen that the $N_2^+ B^2\Sigma_u^+$ state is higher than the $O_2^+ b^4\Sigma_g^-$ and $O_2^+ A^2\Pi_u$ states. This means that both the $O_2^+ b^4\Sigma_g^-$ and $O_2^+ A^2\Pi_u$ states are possible to be generated by charge transfer from $N_2^+ B^2\Sigma_u^+$ to O_2 in the ground state. With the transition from upper to lower states, photons with wavelengths of 602 nm and 440 nm are emitted [88]. However, these two wavelengths were not detected. This may be attributed to the short lifetime of $N_2^+ B^2\Sigma_u^+$, resulting in the production of only small amounts of the $O_2^+ b^4\Sigma_g^-$ and $O_2^+ A^2\Pi_u$ states.

With the decay of $N_2^+ B^2\Sigma_u^+$, $N_2^+ X^2\Sigma_g^+$ with a long lifetime is populated. Furthermore, several high vibrational states of $O_2^+ X^2\Pi_g$ are lower than the low vibrational state of $N_2^+ X^2\Sigma_g^+$ and higher than the ionisation level of water, as shown in Figure 3.5. Therefore, it is suspected that the charge transfer from $N_2^+ X^2\Sigma_g^+$ to $O_2^+ X^2\Pi_g$ and then to H_2O^+ may play a role in the generation of H_3O^+ . There are not enough experimental results that can prove this assumption at this moment. Therefore, more work and effort need to be done in the future.

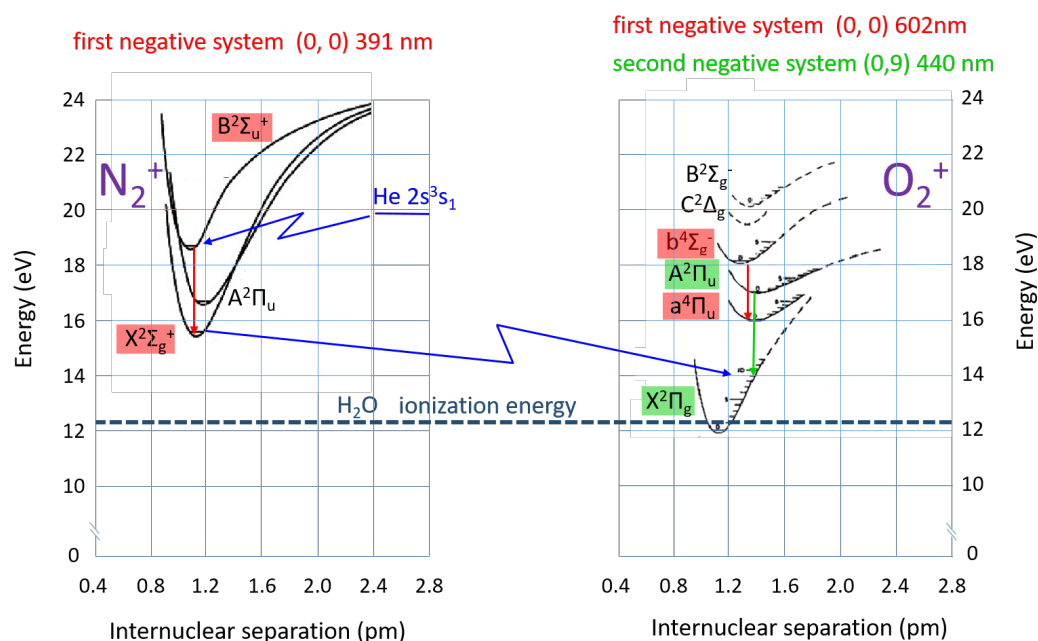


Figure 3.5: Oscillator system of N_2^+ (left), O_2^+ (right) and H_2O^+ (the dark blue dashed line). The red and green arrows show the decay from the upper energy levels to the lower levels of N_2^+ (left) and O_2^+ (right). The blue zigzag arrows indicate the possible energy transfer from the beginning to the end of the arrow.

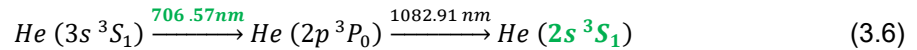
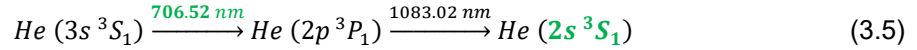
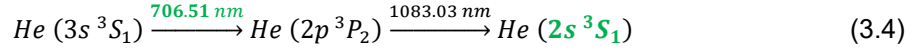
In addition, when the energy difference between He^M and the ionisation energy of analyte M is sufficiently small, He^M can collide directly with analyte M, producing M^+ as given by Equation 3.3.

Based on their important role in the soft ionisation process, He^M and N_2^+ are worth studying in detail. He^M is forbidden to decay to the ground state according to the quantum mechanism selection rules. Therefore, the density of He^M cannot be measured by emission spectroscopy. In principle, the density of He^M can be measured directly by laser diode absorption of He 1083 nm. However, the dimension of F_μTP source with the inner diameter of 250 μm is small. The related measurement on the laser diode absorption of He 1083 nm cannot be carried out.

The spectral line with a wavelength of 706 nm is one of the He spectral lines. There are three distinct wavelengths near 706 nm, which correspond to transitions from the 3s 3S_1 state (He^{**}) to 2p $^3P_{2,1,0}$ states (He^*). The transitions of excited states and the corresponding wavelengths are given in Equations 3.4 to 3.6. However, the resolution of the spectrometers employed in this thesis is insufficient to distinguish these wavelengths. For this reason, He 706 nm is used throughout this thesis. With the decay from He^* to the

3.3 Temporally and Spatially Resolved Emission Spectra

$2s\ ^3S_1$ state (He^M), He^M state with long lifetime is populated. The related transitions are also shown in Figure A.2 of the Appendix. The wavelength of 1083 nm is out of the range of the used spectrometers. It cannot be measured by emission spectroscopy. Therefore, $He\ 706\ nm$ is used to characterise He^M indirectly.



A transition from a vibrational state of $N_2^+\ B\ ^2\Sigma_u^+$ to a vibrational state of $N_2^+\ X\ ^2\Sigma_g^+$, as given in Equation 3.7, results in the emission of a photon with a wavelength of 391 nm.

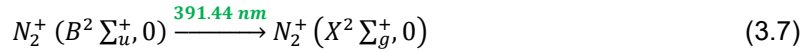


Figure 3.6 shows the temporally and spatially resolved emission of $He\ 706\ nm$ and $N_2^+\ 391\ nm$ in both half cycles. In case of $He\ 706\ nm$, one development process in the positive half cycle and two development processes in the negative half cycle are observed, which is similar to the development of the whole emission. For $N_2^+\ 391\ nm$, the development process along the capillary is clearly observable in both half cycles. However, the development process in the vicinity of the electrode in the negative half cycle is not obvious.

In addition, the temporal shapes of $He\ 706\ nm$ in both half cycles are narrower than those of $N_2^+\ 391\ nm$. One possible explanation for this is that the generation mechanisms of these two species are different. Typically, He^{**} is considered to be generated by the direct collision excitation between the energetic electron and He atoms. These excited He atoms lose their energy by fast transitions to lower states. The He^M with long lifetime loses energy by collision with other partners. N_2 is one of the appropriate collision partners of He^M . He^M collide with the trace N_2 , leading to the production of $N_2^+\ B\ ^2\Sigma_u^+$. Since the lifetime of He^M is longer than that of He^{**} , the generation of $N_2^+\ B\ ^2\Sigma_u^+$ states lasts a longer time scale. As a result, the shapes of $N_2^+\ 391\ nm$ are wider than those of $He\ 706\ nm$.

As mentioned above, $He\ 706\ nm$ emission can be used as an indirect indicator of He^M . In this context, the intensity of $He\ 706\ nm$ emission indirectly represents the density of He^M . In contrast, the emission intensities of $N_2^+\ 391\ nm$ correspond directly to the density of $N_2^+\ B\ ^2\Sigma_u^+$. Since $N_2^+\ B\ ^2\Sigma_u^+$ can be generated through Penning ionisation, it is anticipated that the emission intensity of $N_2^+\ 391\ nm$ will exhibit a correlation with that of $He\ 706\ nm$. Interestingly, the changes in the emission intensities of $He\ 706\ nm$ and $N_2^+\ 391\ nm$ differ.

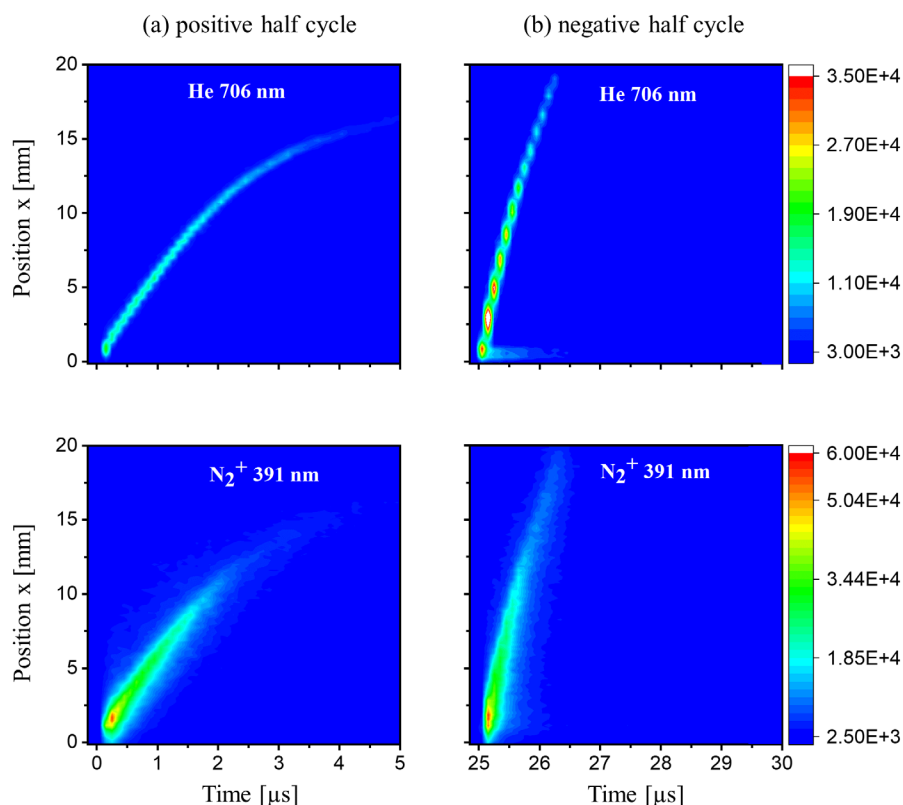


Figure 3.6: Spatial and temporal development of *He* 706 nm (upper) and N_2^+ 391 nm (lower) in the (a) positive positive half cycle and the (b) negative half cycle. The discharge gas is *He* 5.0 with a gas flow of 50 sccm. Adapted with the permission from [79], Copyright 2021 Elsevier.

The emission intensity of *He* 706 nm in the negative half cycle is significantly higher than that observed in the positive half cycle. In contrast, the emission intensities of N_2^+ 391 nm in both half cycles are comparable.

One possible explanation is that a significantly higher density of N_2^+ B $^2\Sigma_u^+$ is generated in the negative half cycle compared to the positive half cycle. The high density of electrons in the negative half cycle driven by secondary electron emission causes a portion of N_2^+ B $^2\Sigma_u^+$ to undergo neutralisation, returning to its ground state. The residual N_2^+ B $^2\Sigma_u^+$ ions decay to the N_2^+ X $^2\Sigma_g^+$ state, emitting radiation at a wavelength of 391 nm. Furthermore, such a neutralisation process reduces the visibility of the N_2^+ 391 nm emission in the vicinity of the electrode. Therefore, only one development process is clearly observed for N_2^+ 391 nm in the negative half cycle.

Although the presence of excited O complicates the mass spectra by yielding a series of oxygen-adduct peaks in addition to protonated molecular ions, the emission of excited O

3.3 Temporally and Spatially Resolved Emission Spectra

serves as an indirect indicator of He^M [89,90]. As given in Equations 3.8 to 3.10, with the transitions from upper excited states to lower excited states, light at different wavelengths are emitted. Similar to He 706 nm, due to the limitations of the resolution of the spectrometers used, O 777 nm is used throughout this thesis.



Figure 3.7 shows the spatial and temporal propagation of O 777 nm in one discharge cycle. The propagation velocity is slower in the positive half cycle than in the negative one. This is similar to the behaviour of both He 706 nm and N_2^+ 391 nm. In addition, it can be seen that not only the emission shape is narrower, but also the emission intensity is weaker in the positive half cycle than in the negative one. This is similar to the behaviour of He 706 nm. Last but not least, the emission in the vicinity of the electrode can be clearly observed. On the basis of these features, it seems that the emission of O 777 nm is mainly caused by the collision of He^M with O_2 in the ground state.

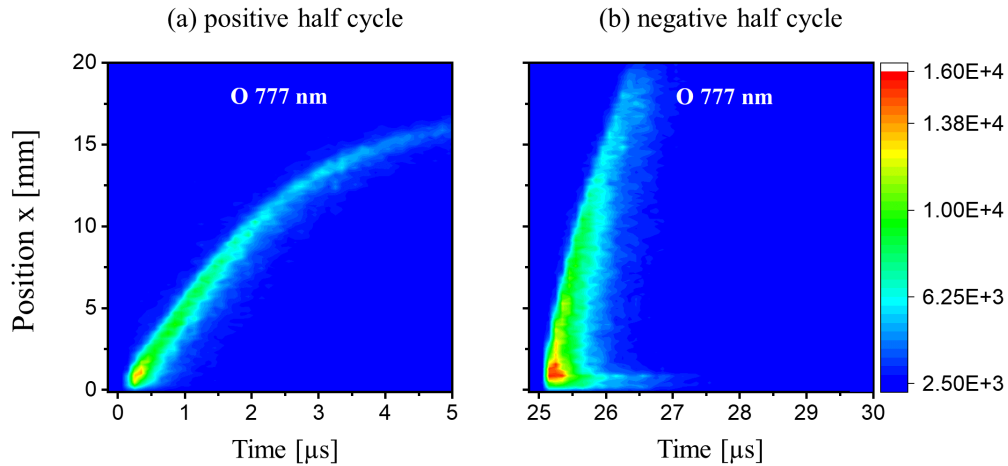


Figure 3.7: Spatial and temporal development of O 777 nm in the (a) positive half cycle and in the (b) negative one. The discharge gas is He 5.0 with a gas flow of 50 sccm. Adapted with the permission from [79], Copyright 2021 Elsevier.

To obtain O 777 nm emission, a species with sufficient energy must first collide with an O_2 molecule, resulting in dissociation into two O atoms. This dissociation process requires an energy input of 5.15 eV. Subsequently, one of the O atoms is excited to the $O^5P_{1,2,3}$ state,

Chapter 3 *FμTP Ionisation Source: A Dielectric Guided Discharge*

which requires additional 10.7 eV. The energy required for this sequence of events is depicted in Figure A.2 of the Appendix. In total, the generation of O 777 nm requires at least 15.85 eV (5.15 eV + 10.7 eV).

Both He^M with energies of 19.8 eV and 20.9 eV, as well as $N_2^+ B^2\Sigma_u^+$ with an energy of 18.7 eV, possess sufficient energy to generate excited O atoms. Moreover, the energy difference between $N_2^+ B^2\Sigma_u^+$ and the energy required for the described collisional reaction is even smaller than that of He^M . This suggests that the possibility of generating excited O through collisions involving $N_2^+ B^2\Sigma_u^+$ might be greater. The detailed generation of excited O has been discussed in recent work [91].

The spatial and temporal colour presentation has a low resolution in position, since the neighbouring positions ($x - m$ and $x + m$) also contribute to the actual intensity. Furthermore, when more than one peak appears at different moments at the same position, the smaller ones (as marked by a green arrow in Figure 3.8) will be covered and not be recognised. To obtain a deeper understanding of the plasma propagation, the emission intensities of the aforementioned species at different positions along the capillary are extracted and replotted to one-dimensional plots. These positions are 5 mm, 10 mm and 15 mm away from the electrode tip.

Figure 3.8 shows the temporal emission of the whole emission, He 706 nm, N_2^+ 391 nm and O 777 nm in both half cycles. The emission intensities of these species decrease along the capillary with increased distance due to the decrease of the electric field along the capillary. This is in accordance with the results shown in Figure 3.2 b. For the positive half cycle (Figure 3.8 a), the time dependent emission appears as discrete peaks, while for the negative half cycle the peaks overlap (Figure 3.8 b).

In addition, it can be clearly seen that their profiles differ. In the case of He 706 nm, the profiles of the increasing and decreasing signal are almost symmetric. This means that the signals of the increasing and decreasing part are contributed by the same process. As explained above, the emission intensity of He 706 nm is proportional to the density of He^{**} generated by direct electron impact. This process depends on the electric field.

The profiles of N_2^+ 391 nm seem significantly asymmetric. A “shoulder” marked by a green arrow is observed in the positive half cycle. It locates on the left side of the maximum of N_2^+ 391 nm peak, which will be investigated in detail in the following section (see Section 3.3.3). In the positive half cycle, the maximum of O 777 is shifted compared to He 706 nm and N_2^+ 391 nm. This offset may be attributed to the two-step process involving the

3.3 Temporally and Spatially Resolved Emission Spectra

dissociation of O_2 into O atoms and the excitation of an O atom to an excited O atom, which will take a longer time.

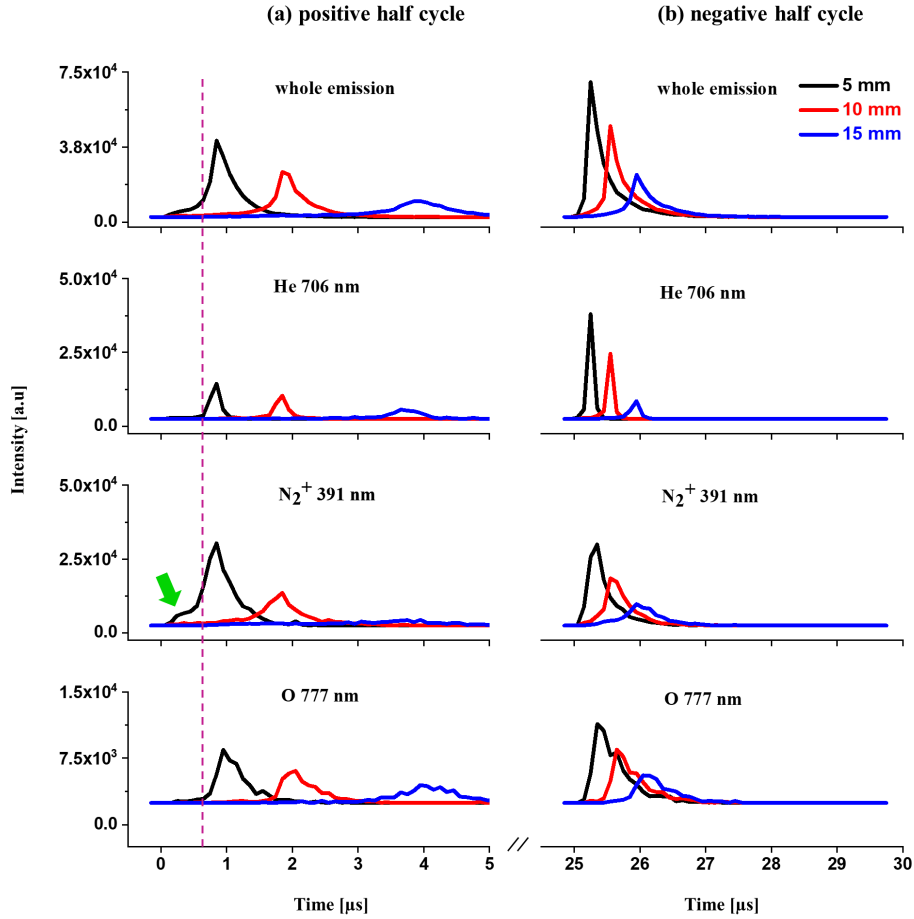


Figure 3.8: Temporal development of the whole emission, He 706 nm, N_2^+ 391 nm, and O 777 nm at different positions along the capillary in the positive (a) and negative (b) half cycle. The pink dashed line indicates the moment when the emission intensity of He 706 nm starts to increase. The green arrow shows a “shoulder” in case of N_2^+ 391 nm. The discharge gas is He 5.0 with a gas flow of 50 sccm. Adapted with the permission from [79], Copyright 2021 Elsevier.

3.3.3 Generation Mechanism of N_2^+

Usually, there are two main pathways for the generation of $N_2^+ B^2\Sigma_u^+$ in a He plasma, the direct collision of energetic electrons with N_2 molecules in the ground state and Penning ionisation. Therefore, the formation of the “shoulder” shown in Figure 3.8 results from the difference in the rates of these two different processes. On closer examination of the moment when the emission of N_2^+ 391 nm appears, it is observed that it initiates simultaneously with the emission of He 706 nm. This indicates that $N_2^+ B^2\Sigma_u^+$ and He^{**} are generated simultaneously. However, as observed on the left side of the pink dashed line,

Chapter 3 *FμTP Ionisation Source: A Dielectric Guided Discharge*

the initial rate of increase for the N_2^+ 391 nm is higher than that for *He* 706 nm. It is considered that the “shoulder” is mainly contributed by direct electron collision. With a population of He^M with a long lifetime, N_2^+ B $^2\Sigma_u^+$ can be generated by Penning ionisation. The following signal of N_2^+ 391 nm is attributed to the contributions of both direct electron collisions and Penning ionisation.

The discrete peaks in the positive half cycle and the overlapping peaks in the negative half cycle of these three species are more obvious compared to the presentation in Figure 3.4. Such overlap makes it difficult to clearly distinguish the processes that generate N_2^+ B $^2\Sigma_u^+$. In this respect, the following experiments of this chapter only focus on the positive half cycle.

As explained above, N_2 molecules present in the discharge gas are involved in the generation of N_2^+ species. Thus, the concentration of N_2 in the discharge gas will have an impact on the generation of N_2^+ species, as well as the gas discharge. To further distinguish the generation processes of N_2^+ species and explore the influence on discharge, several mixtures of *He* with a different amount of N_2 are introduced as discharge gases. In the following measurements, the gate width and step width were adjusted to 10 ns to obtain sufficient resolution on the time and position scales.

Figure 3.9 presents the emission results of *He* 706 nm and N_2^+ 391 nm at different concentrations of N_2 in *He*. Emission intensities are extracted at a position of 5 mm along the capillary. As the concentration of N_2 increases from 3 ppm to 55 ppm, both the emission intensities of *He* 706 and N_2^+ 391 nm increase. Additionally, the timing of their maxima shifts to earlier moments, as shown by black dashed arrows. This indicates that the discharge is enhanced as the concentration of N_2 increases.

However, as the concentration of N_2 further increases to a thousand ppm, the emission intensities of both species decrease. In the meanwhile, their maxima shift to later time points, as shown by black dashed arrows. It can be concluded that a small concentration of N_2 is beneficial for discharge. On the contrary, with a continuous increase beyond a certain concentration, the ionisation of the gas would become more difficult.

One reasonable explanation is that *He* atoms and N_2 molecules are competing against each other. The decrease of the *He* 706 nm signal is caused by a lack of energetic electrons. The energy that an electron can gain in an electric field is related to the strength of the electric field as well as the length of the path that the electron can travel before colliding

3.3 Temporally and Spatially Resolved Emission Spectra

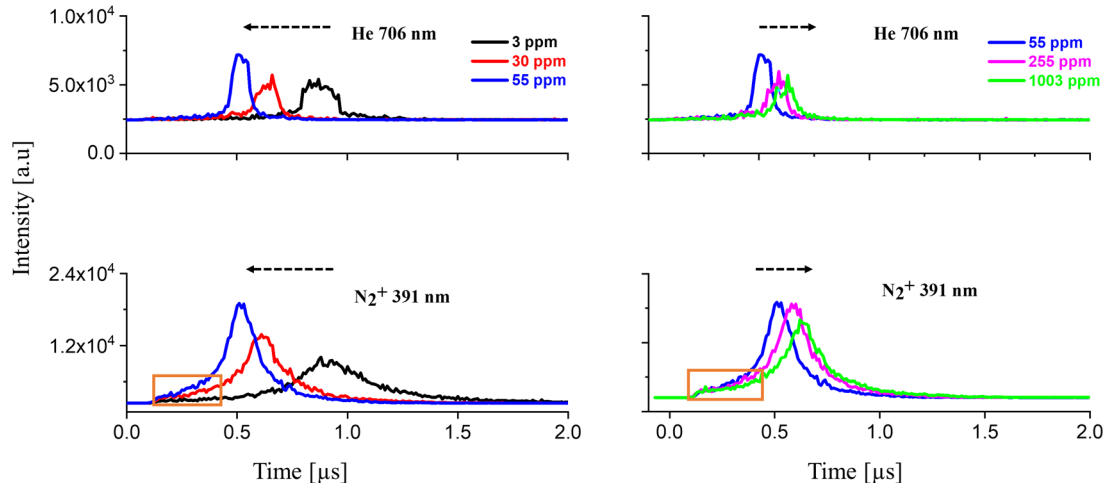


Figure 3.9: Temporal development of He 706 nm (upper) and N_2^+ 391 nm (lower) with different concentration of N_2 as impurity in He in the positive half cycle. The flow rate of the discharge gas is 50 sccm. The position is at 5 mm along the capillary. The orange rectangles show the N_2^+ 391 nm signal that is mainly contributed by direct collision of energetic electrons with N_2 molecules. Adapted with the permission from [79], Copyright 2021 Elsevier.

with a suitable acceptor that matches to the currently available energy of an electron. Because of the high mass difference between an electron and a noble gas atom, the collision between an electron with low energy and an atom is regarded as inelastic. Moreover, there are no He energy states between the ground state and He^M states (19.8 eV and 20.9 eV) that are appreciate acceptors of low energy. Therefore, most of the energy that an electron has gained is retained throughout the collision. An electron can only lose its energy when the energy it has gained through acceleration is sufficient to excite an electron within a He atom to a higher energy state.

N_2 has many excited states between the ground state and the ionised state (15.6 eV). The introduction of N_2 molecules into the gas mixtures means that the electrons have a new collision partner that is available in a lower energy. Therefore, the increase of N_2 to a certain concentration will naturally reduce the number of electrons with high energy and thereby the number of excited He species. This is also the reason why N_2 is harder to be ignited than He 5.0 although the ionisation level of N_2 is lower than the energy level of He^M .

As the excited He decreases, the N_2^+ produced by Penning ionisation decreases correspondingly. However, as marked by the orange rectangle, the “shoulder” of the N_2^+ 391 nm signal becomes visible when the concentration of N_2 in the discharge gas increases in a certain range. This can be explained that the probability of collision between energetic electrons and N_2 molecules increases at higher concentration of N_2 , resulting in an

Chapter 3 *F μ TP Ionisation Source: A Dielectric Guided Discharge*

increased contribution of the electron collision process to the “shoulder”. Therefore, the “shoulder” of the N_2^+ 391 nm signal is mainly contributed by direct collision of energetic electrons with N_2 molecules. While the other areas are a summation of direct electron collisions and Penning ionisation. As a result, the generation process of $N_2^+ B^2\Sigma_u^+$ is prolonged by a superimposing effect of direct electron collisions and Penning ionisation. This further leads to a wide emission shape of N_2^+ 391 nm compared to that of *He* 706 nm.

3.4 Conclusion

The investigation of the discharge development of a *He* driven plasma is the starting point for understanding the discharge mechanism of a *F μ TP* and exploring its further applications as a soft ionisation source. This chapter characterises the reactive species generated in a *He-F μ TP* in the wavelength range of 300 - 900 nm, as well as the temporal and spatial development of several species by optical emission spectroscopic techniques. The whole emission, *He* 706 nm, N_2^+ 391 nm, and O 777 nm, were investigated.

In the positive half cycle, the plasma initially starts at the electrode tip and propagates forward along the discharge capillary. When the positive half cycle ends and the negative half cycle begins, the plasma is ignited once more. Two discharge processes were identified in the negative half cycle. One of the discharge developments propagates in the same direction as the discharge propagation in the positive half cycle. A closer examination revealed that such propagation is more continuous and faster compared to the case of the positive half cycle. This is related to the charges attached to the wall and the electron density. As the plasma propagates forward during the positive half cycle, charges attach on the wall, forming charged rings. These charged rings serve as virtual electrodes, guiding the discharge and propagation forward along the capillary in the negative half cycle. A negative glow discharge was also identified in the vicinity of the electrode caused by the secondary electron emission during the negative half cycle. These electrons are accelerated in the electric field, which further enhances the discharge in this half cycle, leading to a stronger emission and a faster propagation.

Although the *F μ TP* ionisation source originates from a DBD configuration, it is not a dielectric barrier discharge in the strict sense, but rather a dielectric guided discharge. Moreover, no coincident plasma is formed in the *F μ TP* compared to normal dielectric barrier discharges. This improves the soft ionisation capacity of the present source.

3.4 Conclusion

In addition, a controlled amount of N_2 was added to *He* and measurements were carried out using the mixtures as discharge gases. As a result, a small concentration of N_2 in *He* is beneficial for discharge, whereas a continuously increasing concentration of N_2 makes discharge difficult. Furthermore, the generation mechanism of N_2^+ was experimentally identified to be electron collision and Penning ionisation.

Discharge Mechanisms of the

F μ TP *P2, P3, P4, P5*

The investigations of plasma propagation in a *He*-F μ TP have been carried out in a confined environment with a discharge column length of 30 mm in the last chapter. When the F μ TP

P2: Parts of this chapter are based on the previously published article: Soft ionisation mechanisms in flexible μ -tube plasma—from F μ TP to closed μ -tube plasma by Speicher L, Song H, Ahlmann N, Foest D, Höving S, Brandt S, Niu G, Franzke J, **Tian C**; it was first published in *Analytical and Bioanalytical Chemistry*, 2024 as an open access article and is licensed under Creative Commons Attribution 4.0 International License (<http://creativecommons.org/licenses/by/4.0/>).

P3: Substantial parts of this chapter are based on the previously published article: Soft ionisation mechanisms in flexible μ -tube plasma—elucidation of *He*-, *Ar*-, *Kr*-, and *Xe*-F μ TP by **Tian C**, Song H, Ahlmann N, Brandt S, Foest D, Niu G, Franzke J, Speicher L; it was first published in *Analytical and Bioanalytical Chemistry*, 2024 as an open access and is licensed under Creative Commons Attribution 4.0 International License (<http://creativecommons.org/licenses/by/4.0/>).

P4: Parts of this chapter are based on an article under submission: Study of the discharge mode transition in a *Ne*-Flexible μ -Tube Plasma by **Tian C**, Speicher L, Song H, Ahlmann N, Brandt S, Foest D, Niu G, Franzke J; it was first published in *Spectrochimica Acta Part B: Atomic Spectroscopy*, 2025 as an open access and is licensed under Creative Commons Attribution-noncommercial 4.0 international license (<https://creativecommons.org/licenses/by-nc/4.0/>).

P5: Parts of this chapter are based on the previously published article: Elucidation of discharge mechanisms in *He*- and *Ar*-flexible μ -tube plasmas by temporally and spatially resolved plasma optical emission Phoresis spectroscopy by Song H, **Tian C**, Speicher L, Ahlmann N, Brandt S, Niu G, Franzke J; it was first published in *Spectrochimica Acta Part B: Atomic Spectroscopy*, 2024 as an open access and is licensed under Creative Commons Attribution-noncommercial 4.0 international license (<https://creativecommons.org/licenses/by-nc/4.0/>).

Chapter 4 Discharge Mechanisms of the F μ TP

is used as a soft ionisation source in conjunction with a mass spectrometer to analyse analytes, the capillary outlet of the F μ TP is usually located in front of the mass spectrometer inlet. However, when the discharge volume is too long, the plasma cannot reach the end of the capillary. As a result, the ion signals detected by a mass spectrometer are relatively low. Therefore, a short discharge volume is generally chosen for such applications. To be consistent with the actual operation conditions, further investigations of the F μ TP are worth being carried out and discussed. In this chapter, the discharge mechanism of the F μ TP will be investigated in a 3 mm long discharge volume. It is the same length as the discharge cell used in analytical applications [92,93].

Both *He* and *Ar* are used as discharge gases in ambient ionisation sources for analytical applications. In *He*-driven plasmas, N₂⁺ can be generated through Penning ionisation. The ionisation mechanisms seem clear and are assumed to be similar to APCI [3]. However, it remains challenging in *Ar* plasmas. In this chapter, the ionisation efficiencies using not only *He* and *Ar* but also *Ne*, *Kr*, and *Xe* as discharge gases will be investigated preliminarily by MS measurements. The gas is introduced into the same F μ TP source, where the plasmas operated with different discharge gases can be sustained without altering the geometry of the setup.

Furthermore, the discharge behaviours of the named plasmas will be investigated and compared comprehensively. One of the key elements is the analysis of plasma propagation inside the capillary as well as plasma propagation outside the capillary. Another important element is to investigate the propagation of these plasmas during the negative half cycle and to compare them with the development in the positive half cycle.

The aim of the systematic comparison of these plasmas is to identify the commonalities and differences in the discharge of these plasmas. This analysis can provide a reference for further plasma-based applications from the perspective of discharge processes, particularly in elucidating the ionisation mechanisms of plasmas as soft ionisation sources in the field of analytical chemistry. On the basis of the characterisation of these plasmas through mass spectrometry and optical emission spectroscopy, an alternative mechanism for the soft ionisation is proposed. The part of data shown in this chapter have been published in 2024 [91-94].

4.1 Mass Spectrometric Characterisation of the F μ TP

The F μ TP has been used as a soft ionisation source for analytical applications, allowing to outperform other plasma-based ionisation sources such as DBDI and LTP [9]. No matter whether it was used as a single ionisation source [65-67] or a post-ionisation source coupled to other ionisation sources such as paper spray [69], ESI [70] or laser desorption [63,64], it has been successfully used to ionise less polar compounds. In those applications, *He* was used as a discharge gas because of the low breakthrough voltage and the ionisation mechanism thought to be known. To explore the soft ionisation mechanism, noble gases *He*, *Ne*, *Ar*, *Kr*, and *Xe* are used as discharge gases. The F μ TP allows to ignite the plasma with different working gases without changing the configuration.

The ionisation efficiency of a discharge usually depends on many factors. The position of the discharge relative to the mass spectrometer inlet is one of the important factors. Usually, it is difficult to guarantee that the exchanged discharge is in exactly the same position as the previous one. Usual practice is to adjust the discharge position according to the intensity of the signal. This defeats the purpose of a comparative measurement, as this is probably going to result in a completely different optimal position for the exchange discharge. The discharge gas can be easily switched in the case of the F μ TP without affecting the consistency of other conditions. This is therefore good for an objective comparison of the results as it is able to guarantee that all observed differences are caused only by the switching of the discharge gas type. This greatly improves the availability of the F μ TP.

Another factor that can influence the comparison of the measurement is the condition set for the mass spectrometer itself. For the investigation of the ionisation efficiency of different noble gases driven plasmas, the F μ TP source is mounted in front of a Finnigan LTQ mass spectrometer (Waltham, USA). Analyte is supplied externally by head space in the form of vaporised gas to the active regions of the plasma discharge. For all mass spectra measurements, the parameters used are fixed. It ensures that all observed changes are not caused by the different conditions of the mass spectrometer but only by the switching of discharge gas type. The MS parameters used can be found in the original study published in 2024 [93]. The mass spectrometric characterisation was measured by Luisa Speicher at Leibniz-Institut für Analytische Wissenschaften – ISAS – e.V.

The analyte used for testing is 2,5-hexanedione (HexD). It was bought from Sigma-Aldrich. It was chosen because the mass spectra generated by plasmas are rather simple and thus

Chapter 4 Discharge Mechanisms of the F μ TP

easy to analyse. The analyte was placed in a vial. N₂ with a flow rate of 100 sccm passed through the vial. After the vapour pressure balanced, the headspace gas was used as an analyte gas. It was delivered into the reaction region and then ionised. The schematic diagram for the MS measurements is shown in Figure 4.1 a.

The mass spectra of the low-mass ions without analyte were firstly measured. The results are shown in Figure 4.1 b. These spectra are essential to obtain information on the reactant ions and ionisation background. In these plasmas, the mass spectra show a clean background and mainly consist of peaks related to the ion-molecule chemical reactions. The signal corresponding to protonated water clusters, specifically [(H₂O)₂H]⁺ at m/z 37, exhibits the highest intensity within each spectrum, followed by [(H₂O)₃H]⁺ at m/z 55. Figure 4.1 c shows the mass spectra with the analyte. It can be seen that the peak of protonated HexD at m/z 115 is the prominent signal in each case. Additionally, the smaller peak is observed at m/z 132, which belongs to [HexD+OH+H]⁺.

As mentioned in the chapter of **Introduction** (see Section 1.1), the ionisation mechanism of *He* plasma has long been assumed to be similar to APCI due to the fact that N₂⁺ are generated in *He* plasma. In the presence of N₂⁺, protonated water clusters are produced by a series of reactions. When the proton affinity of an analyte is higher than that of neutral water molecules, a proton attaches to a neutral analyte molecule with mass [M] to form a new positively charged molecule with an increased mass of [M+1] [95]. The mass spectra obtained in the *He*-F μ TP make the aforementioned mechanism of a *He* plasma more convincing.

However, when other noble gases such as *Ne*, *Ar*, *Kr* and *Xe* are used for the discharge, the mass spectra obtained of both low mass ions without analyte and with analyte are similar to those measured with the *He*-F μ TP. The similar mass spectra imply that the ionisation of ambient air and HexD in these plasmas follows a very similar mechanism and also produces fundamentally the same ionised species.

In a *He*-F μ TP, there is no doubt that N₂⁺ ions in the upper states (N₂⁺ B ²Σ_u⁺) can be generated by Penning ionisation. Similarly, N₂⁺ X ²Σ_g⁺ can also be produced by Penning ionisation in a *Ne*-F μ TP. The energy states of the relative species are shown in Figure 4.2. That is, the mass spectra obtained with *Ne*-F μ TP as the ionisation source might be explained by the presence of N₂⁺ X ²Σ_g⁺ in the plasma.

In an *Ar*-F μ TP, N₂⁺ B ²Σ_u⁺ and N₂⁺ X ²Σ_g⁺ states cannot be generated by Penning ionisation. This is because their energy levels are higher than those of the *Ar* metastable states (*Ar*^M),

4.1 Mass Spectrometric Characterisation of the F μ TP

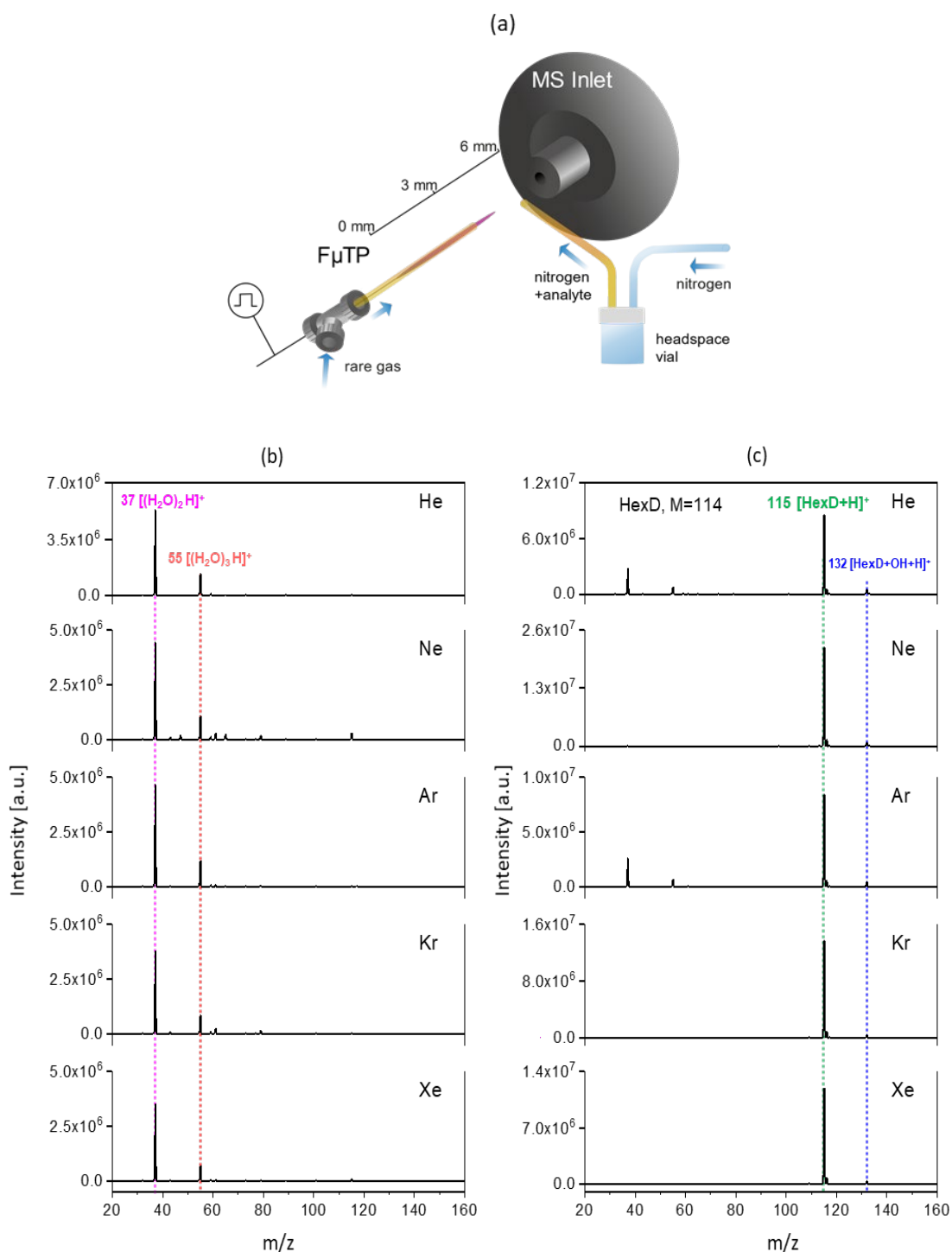


Figure 4.1: (a) Experimental arrangement of a F μ TP for mass spectrometric measurements. (b) Mass spectra of the low-mass ions without analyte using F μ TPs-MS in positive mode. (c) Mass spectra of HexD using F μ TPs-MS in positive mode. The used discharge gas is shown on the corresponding spectrum. The applied voltage for all plasmas is 3.0 kV and the discharge gas flow rate is 75 sccm. Adapted with the permission from [92, 93], Copyright 2024 Springer.

Chapter 4 Discharge Mechanisms of the F μ TP

as shown in Figure 4.2. However, the energy level of Ar^+ is higher than that of $N_2^+ X^2\Sigma_g^+$, the charge transfer between Ar^+ and nitrogen molecules could occur, generating $N_2^+ X^2\Sigma_g^+$. It is worth noting that Ar^+ has a shorter lifetime than Ar^M . Therefore, the generation of $N_2^+ X^2\Sigma_g^+$ by charge transfer is very low.

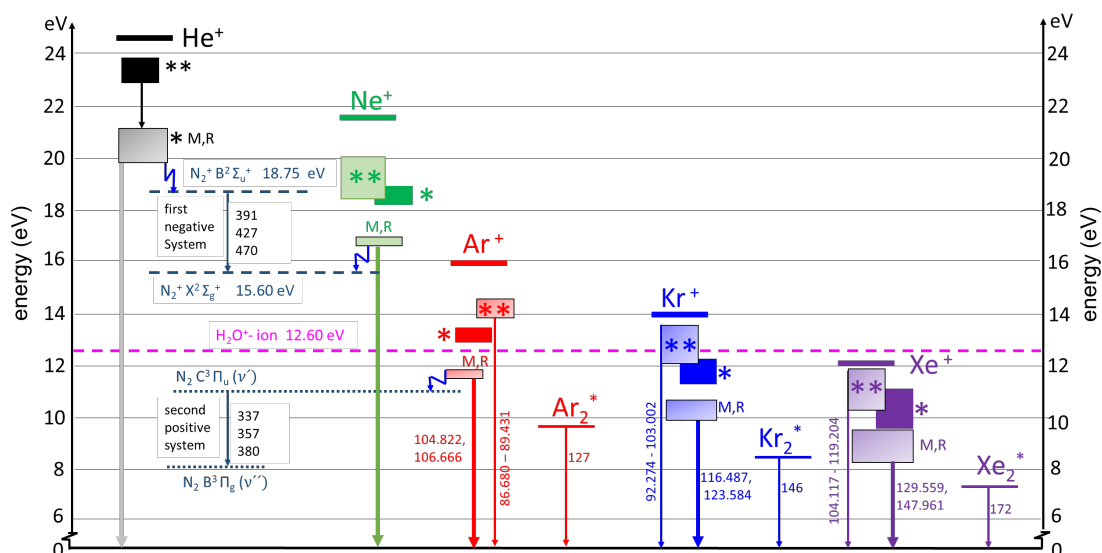


Figure 4.2: Diagram of the excitation and ionisation energy for different noble gases and related nitrogen species. The schematic shows some selected energy levels and associated optical transitions with their respective wavelengths. Numbers at the transitions are the wavelength in [nm]. The blue zigzag arrows indicate the Penning ionisation in case of He and Ne plasmas, and excitation transfer in Ar plasma. Adapted with the permission from [93], Copyright 2024 Springer.

In addition, the $N_2^+ X^2\Sigma_g^+$ might be generated by the collision of energetic electrons with N_2 in an Ar plasma, as the ionisation levels of the Ar atom (15.8 eV) and N_2 (15.6 eV) are close. As explained in last chapter, the energy that an electron can acquire in a certain electric field depends on the strength of the electric field, the acceleration that an electron acquires, and the length of the path that an electron can travel before it collides with an atom or molecule that is suitable to receive the energy it has acquired so far. In this sense, Ar atoms and N_2 are suitable collision partners for energetic electrons. However, only 5 ppm N_2 is present in Ar 5.0. The generation of $N_2^+ X^2\Sigma_g^+$ by electron impact is thus low. Nevertheless, the mass spectra obtained with Ar -F μ TP as ionisation source might also be explained by the presence of $N_2^+ X^2\Sigma_g^+$ in the plasma.

In a Kr -F μ TP, N_2^+ ions are absent. On the one hand, they cannot be generated by Penning ionisation or charge transfer. Any energy state of a Kr plasma is lower than $N_2^+ B^2\Sigma_u^+$ and $N_2^+ X^2\Sigma_g^+$ states. On the other hand, Kr atoms are the more suitable collision partners with

4.1 Mass Spectrometric Characterisation of the $F\mu TP$

lower-energy states available, generating ionic states compared to the nitrogen molecules. Therefore, the generation of N_2^+ by direct electron collisions is negligible in a Kr - $F\mu TP$.

However, the mass spectra obtained with Kr - $F\mu TP$ as an ionisation source are similar to those of the He , Ne , and Ar plasmas, as shown in Figure 4.1 b and c. The most obvious explanation is that the protonated water clusters are generated directly in a Kr - $F\mu TP$. The ionisation level of the water molecule is 12.6 eV. This level is lower than the level of Kr^+ , as shown in Figure 4.2. In principle, charge transfer can take place between Kr^+ and water molecules. However, because of the short lifetime of Kr^+ , the generation of protonated water clusters by charge transfer is very low.

In addition, water molecules are the more suitable collision partners with lower-energy states available, generating ionic states compared to Kr atoms. Therefore, protonated water clusters are probably generated by direct electron impact. Photoionisation by radiation leaving plasmas is another potential path to ionise water molecules in a Kr - $F\mu TP$. The relevant transitions can be seen in Figure 4.2. Correspondingly, the related wavelengths and energies are listed in Table 4.1. The exact wavelengths with three decimal places of atomic transition are given, which are found in the NIST Atomic Spectra Database [96].

Table 4.1: Photoionisation related energy states in a Kr plasma and the ionisation level of H_2O

Type	Transition path	Kr		H_2O
		Wavelength range (nm)	Energy range (eV)	Ionisation energy (eV)
Atomic transition	$Kr^R - Kr^G$	116.487	10.64	12.6
		123.584	10.03	
	$Kr^{**} - Kr^G$	92.274 - 103.002	13.44 - 12.04	
Excimer transition	$Kr_2^* - Kr^G$	147	8.5	

There are two pathways. One starts from the resonant states (Kr^R) to the appropriate ground state (Kr^G). As shown in Table 4.1, all these energies are too low to ionise the water molecule with an ionisation level of 12.6 eV.

Another path is starting from the higher excited states marked by two stars to the corresponding ground states. The energy released during certain transitions in this process

Chapter 4 Discharge Mechanisms of the F μ TP

is sufficient to ionise water molecules. The vacuum ultraviolet (VUV) transitions mentioned above are atomic transitions. At gas pressures higher than 300 mbar, the excimer transitions are observed to increase with increasing gas pressure [26,27,97]. The relevant transitions for atmospheric pressure plasmas are more excimer transitions. In a Kr plasma, the corresponding energy of excimer transition is 8.5 eV with an emission wavelength of 147 nm [98]. This energy is not sufficient to ionise water molecules.

Anyway, it is possible to ionise water molecules by a Kr plasma even if only a few ppm water is present. The mass spectra obtained with a Kr plasma as an ionisation source might be explained by the presence of protonated water clusters.

Surprisingly, the mass spectra obtained with a Xe plasma as an ionisation source are similar to those obtained with other plasmas. It is clear that all states of the Xe plasma are not sufficient to ionise water molecule. It is impossible to ionise water molecules by Penning ionisation, charge transfer, or photoionisation by the Xe plasma, let alone nitrogen.

However, the ionisation efficiencies of these plasmas are surprisingly comparable in the generation of protonated water clusters and protonated analyte. The result is shown in Figure 4.3. The ionisation efficiency is described here simply as the abundance of ions that are generated by a plasma and then measured by the used mass spectrometer. This is surprising because, according to the explanation above, it is considered that significantly fewer signals will be obtained in an Ar- and a Kr-F μ TP and even no signals in a Xe-F μ TP will be yielded. However, the reality is quite the opposite. This is also the reason why Xe is used to study the ionisation mechanism even it is too expensive and not common for

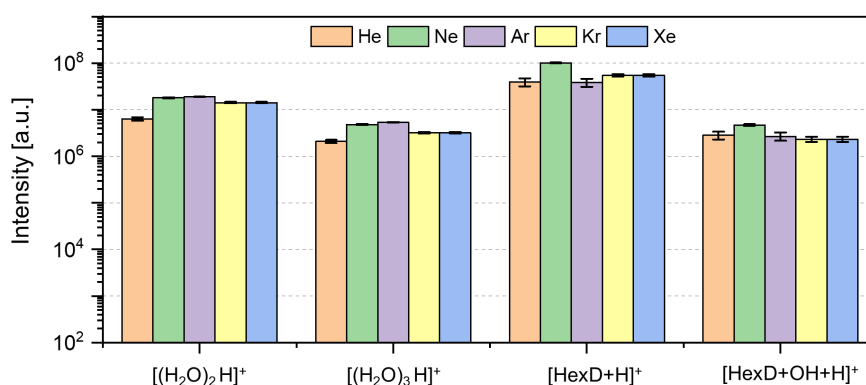


Figure 4.3: Comparison of peak intensities of $[(\text{H}_2\text{O})_2\text{H}]^+$, $[(\text{H}_2\text{O})_3\text{H}]^+$, $[\text{HexD} + \text{H}]^+$ and $[\text{HexD} + \text{OH} + \text{H}]^+$ obtained with He-, Ne-, Ar-, Kr- and Xe-F μ TP. Measured intensities are shown in logarithmic (log) scale for different ionisation sources. The applied voltage for all plasmas is 3.0 kV and the discharge gas flow rate is 75 sccm.

4.2 Spectroscopic Characterisation of the F μ TP

analytical applications. One plausible explanation for the similar mass spectra and comparable ionisation efficiency observed among these plasmas is offered even if the well-accepted Penning ionisation or charge transfer is not applicable to a Xe plasma. It suggests that such processes might not be the predominant ones for *He* and *Ar* plasmas as well. Instead, other mechanisms are responsible for the ionisation. In other words, the ionisation mechanism of *He*-driven plasmas that has long been assumed to be similar to APCI is questioned whether it is correct and complete or not. The results presented above, involving different noble gases, suggest a more complex mechanism responsible for soft ionisation.

It is beneficial to elucidate the discharge of these noble gases to give more understanding on the soft ionisation mechanism. The detailed characterisation of discharge types using all the aforementioned noble gases will be given in the following sections aiming at finding the reason for the comparative ionisation efficiency of these plasmas.

4.2 Spectroscopic Characterisation of the F μ TP

4.2.1 Experimental Conditions

The experimental arrangement used for spectroscopic experiments in this chapter is similar to the one used in the previous chapter (see Figure 3.1). The main differences are the length of the discharge column and the applied voltage.

In this chapter, the length of the discharge column is shortened to 3 mm. The bipolar power generator is used to apply HV. The bipolar square-wave voltage is shown in Figure B.1 of the Appendix. The frequency of applied voltage is 20 kHz and the duty cycle is 50:50. The detailed voltage amplitudes for various plasmas are listed in Table 4.2.

For a Xe-F μ TP, a higher ignition voltage is usually required. To ignite a Xe plasma with the current experimental equipment, an additional metal ring was installed on the coaxial side of the capillary. The ring is grounded and positioned 2 mm behind the electrode tip. The inner diameter of the ring is around 100 μ m. It ensures that the discharge capillary and the ring are not in contact, reducing the effect of the metal ring on the plasma. The schematic is shown in Figure B.2 of the Appendix.

The entrance slit of the Kymera Spectrograph is set at 200 μ m. A diffraction grating comprising 1200 grooves per millimetre is selected. The object distance and image

Chapter 4 Discharge Mechanisms of the F μ TP

distance are around 240 mm and 120 mm, respectively. Various gases are introduced as discharge gases at a flow rate of 50 sccm. The conditions for the different plasmas are listed in Table 4.2. In order to obtain an adequate emission intensity and high temporal and spatial resolution, different gate width, step width and gain are chosen.

For the acquisition of the time integrated emission spectra of the various plasmas, the integration time of 30 ms is applied for *He*, *Ne*, *Ar* and *Kr* driven plasmas and 200 ms for a *Xe* plasma.

Table 4.2: Experimental conditions used for different plasmas

Plasma	Applied voltage (kV)	Gate width (ns)	Step width (ns)	Gain (a.u)
<i>He</i> -F μ TP	2.5	10	10	250
<i>Ne</i> -F μ TP	2.0	10	10	150
<i>Ne</i> -F μ TP	2.5	5	5	150
<i>Ar</i> -F μ TP	3.5	2.5	2.5	200
<i>Kr</i> -F μ TP	3.5	2.5	2.5	250
<i>Xe</i> -F μ TP	3.3 plus a ring	2.5	2.5	255
^a <i>Ar</i> -propane-F μ TP	2.2	5	5	250

^a“a” the concentration of propane in *Ar* is 2000 ppm

4.2.2 Overview of Species in Different Plasmas

Each plasma has a unique emission spectrum. Measurement of the emission spectra of different plasmas can provide information about which species within the detection range of the spectrometer are involved in the plasmas. This is essential for the further characterisation of an individual plasma. For this reason, *He*, *Ne*, *Ar*, *Kr* and *Xe* are introduced into the F μ TP and the emission spectra of the corresponding plasmas are measured with an USB 4000 spectrometer.

The optical fibre was perpendicular to the discharge axis and positioned in the middle of the discharge column (at $x = 1.5$ mm). The optical emission spectra of these named plasmas are shown in Figure 4.4 (left) showing that the reactive species generated in these plasmas differ. The inserted figures are the spectra for a *Kr*- and *Xe*- F μ TP with higher

4.2 Spectroscopic Characterisation of the F μ TP

sensitivity in the visible range. The photos of these plasmas are also shown in Figure 4.4 (right).

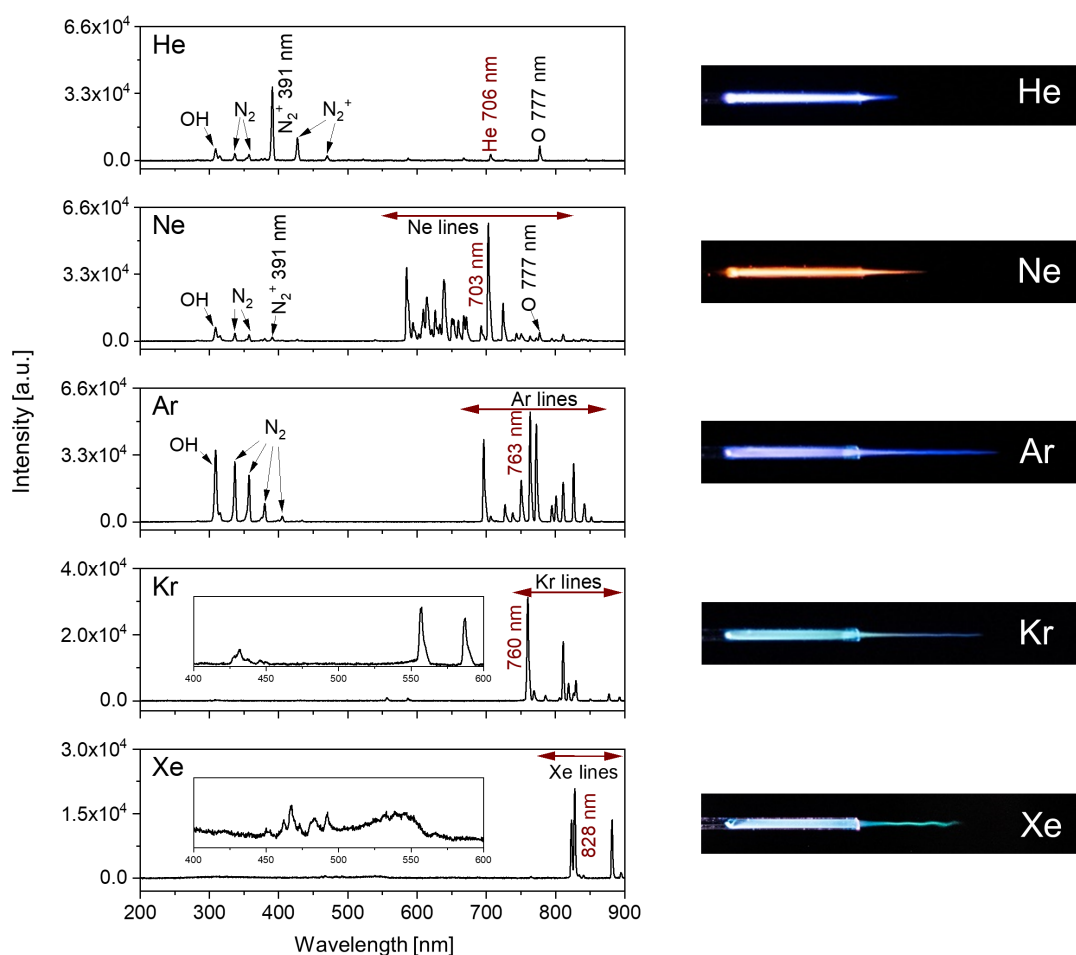


Figure 4.4: The time integrated emission spectra of *He*-, *Ne*-, *Ar*-, *Kr*- and *Xe*-F μ TP obtained by an optical fiber spectrometer (left) and photos of named plasmas (right). The inserted figures are the spectra for a *Kr*- and *Xe*--F μ TP with higher sensitivity in the visible range. The fiber is positioned at $x = 1.5$ mm of the capillary. The applied voltages are 2.5, 2.0, 3.5, 3.5, 3.3 kV with a grounded ring, respectively. The *Xe* plasma had a grounded ring around the capillary in the vicinity of the electrode. The integration time for case of *He*-, *Ne*-, *Ar*- and *Kr*-plasma is 30 ms, for *Xe*-plasma it is 200 ms. The gas flow is 50 sccm. Adapted with the permission from [93], Copyright 2024 Springer.

The emission of excited OH and excited N₂ (SPS, N₂ C ³ $\Pi_u \rightarrow$ N₂ B ³ Π_g) is observed in the *He*-, *Ne*- and *Ar*-F μ TP. Under experimental conditions with a gas flow of 50 sccm and an inner diameter of 250 μ m, ambient air diffuses only in the vicinity of the capillary nozzle. Therefore, these species originate from impurities in discharge gases. H₂O and N₂ are also included as impurities in *Kr* and *Xe*, while the emission of excited OH and excited N₂ is not observed in a *Kr*- and *Xe*-F μ TP. Although there are differences in the contents of the

Chapter 4 Discharge Mechanisms of the F μ TP

different components in these noble gases, as shown in Table 4.3, such a difference probably has a minor impact on the emission intensities of these species.

Table 4.3: Components of different noble gases

Components	<i>He</i>	<i>Ne</i>	<i>Ar</i>	<i>Kr</i>	<i>Xe</i>
N ₂	3 ppm	2 ppm	5 ppm	5 ppm	5 ppm
O ₂	2 ppm	1 ppm	2 ppm	1 ppm	0.5 ppm
H ₂ O	3 ppm	2 ppm	3 ppm	2.5 ppm	2 ppm
Hydrocarbons	1 ppm	-	0.2 ppm	2 ppm	1 ppm

“-” without hydrocarbons

The main reason for these results is the energy differences between these excited species and the excited noble gas atoms, especially the metastable states of these noble gases. The metastable states have a high population in cold plasmas and a long lifetime. Therefore, the probability of collisions with other molecules or atoms is significantly higher. In contrast, other excited states lose their energy by fast transitions to lower states, resulting in a short lifetime. The collisions between these states and other species is minimal.

As shown in Figure 4.2, the energy levels of the metastable states of *Kr* (Kr^M) and *Xe* (Xe^M) are lower than those of N₂ C ³Π_u. It is impossible to produce N₂ C ³Π_u in a *Kr*- and *Xe*-F μ TP by excitation transfer, resulting in the emission of the SPS. The energy of Ar^M is sufficient to generate N₂ C ³Π_u by excitation transfer. Furthermore, the energy differences between the metastable states and N₂ C ³Π_u in an *Ar*-F μ TP are much smaller than those in a *He*- and *Ne*-F μ TP. Therefore, the emission of SPS is more obvious in an *Ar*-F μ TP than in other plasmas. It is worth noting that the absolute emission intensity of the same wavelength measured in different plasmas should not be directly compared because of the different experimental conditions used in these plasmas.

The emission of N₂⁺ (FNS, N₂⁺ B ²Σ_u⁺ → N₂⁺ X ²Σ_g⁺) is observed in a *He*- and *Ne*-F μ TP. It is more obvious in a *He*-F μ TP than in a *Ne*-F μ TP. As explained in the last chapter, the generation of N₂⁺ B ²Σ_u⁺ in a *He*-F μ TP is composed of two pathways. One is contributed by the electron impact and the other by Penning ionisation, of which Penning ionisation contributes the greater part. In a *Ne*-F μ TP, the energy of Ne^M is lower than that of N₂⁺ B ²Σ_u⁺. Thus, N₂⁺ B ²Σ_u⁺ cannot be generated by Penning ionisation. The generation of N₂⁺ B ²Σ_u⁺ in *Ne*-F μ TP will be discussed in detail in Section 4.2.3. The energy level of N₂⁺ B ²Σ_u⁺ is higher than all states of *Ar*, *Kr* and *Xe* plasmas, as shown in Figure 4.2. In addition, the

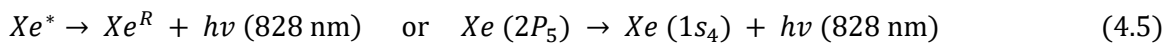
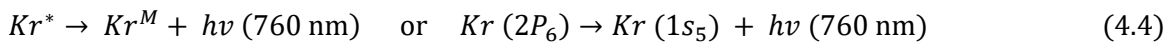
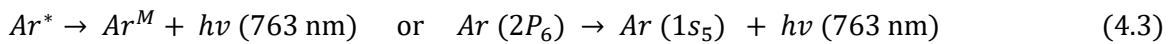
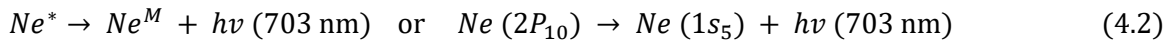
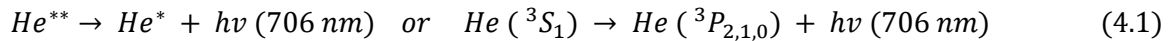
4.2 Spectroscopic Characterisation of the F μ TP

electrons have suitable acceptors with lower energy states available, which are *Ar*, *Kr* and *Xe* atoms in these three discharges. Therefore, $N_2^+ B^2\Sigma_u^+$ cannot be generated.

The emission of excited O at 777 nm is observed and distinguishable in a *He*- and *Ne*-F μ TP. As explained in the previous chapter, the required energy for the excitation of O is 15.85 eV in total. It includes the dissociation energy of molecular oxygen (5.15 eV) into two O atoms and the subsequent excitation energy of one of them to the excited state (10.7 eV). In these plasmas, only He^M and Ne^M can meet the energy needs. Therefore, O 777 nm can only be observed in a *He*- and *Ne*-F μ TP, rather than in an *Ar*-, *Kr*- and *Xe*-F μ TP.

Reactive species related to excited noble gases are marked in wine in each spectrum of Figure 4.4. In case of a *He*-F μ TP, the wavelength at 706 nm has a greater emission intensity compared to other wavelengths. The light at this wavelength is emitted after the decay from the upper excited *He* state (He^{**}) to the lower excited *He* state (He^*) as given in Equation (4.1). It is used as a representative to characterise a *He* plasma.

A series of *Ne* lines from around 580 nm to 820 nm, *Ar* lines in the wavelength range of 690 nm to 850 nm, *Kr* lines in the range of 750 nm to 900 nm, and *Xe* lines in the range of 810 nm to 900 nm are observed. These are the emission lines that decay from the upper excited states to the corresponding metastable or resonant states. The transitions from the upper excited state to one of the metastable states for a *Ne*-, *Ar*- and *Kr*-F μ TP and to one of the resonant states for a *Xe*-F μ TP are picked up as given below. The corresponding wavelengths are *Ne* 703 nm, *Ar* 763 nm, *Kr* 760 nm, and *Xe* 828 nm with the highest measured intensity.



In addition to knowing the types of reactive species in plasmas, the generation and propagation of these species within the capillary as well as their transition to ambient air are also important for advancing the study of the soft ionisation mechanism. To figure out these processes, the temporally and spatially resolved plasma emission information were obtained by means of the Kymera Spectrograph with an ICCD camera. The wavelengths

Chapter 4 Discharge Mechanisms of the F μ TP

of He 706 nm, Ne 703 nm, Ar 763 nm, Kr 760 nm, and Xe 828 nm were chosen as the representative of the individual plasma for further measurements.

The temporal and spatial emission spectra of these species are shown in Figure 4.5 (left). Additionally, the temporal and spatial emission spectra of N₂⁺ 391 nm measured in a He-F μ TP as well as a Ne-F μ TP are also shown in Figure 4.5 (right). No N₂⁺ 391 nm signal is probed in an Ar-, Kr- and Xe-F μ TP.

The most obvious difference between these temporal and spatial emission spectra is the emission width. The profiles of He 706 nm, and Ne 703 nm operated at 2.0 kV, as shown in Figure 4.5 a and b, are thin. While the profiles of Ar 763 nm, Kr 760 nm, and Xe 828 nm as presented in Figure 4.5 d, e, and f are wide. When the applied voltage for Ne-F μ TP is increased from 2.0 kV to 2.5 kV, the profile of Ne 703 nm becomes wide. This is shown in Figure 4.5 c. It is closer to Ar 763 nm, Kr 760 nm, and Xe 828 nm than to He 706 nm. In addition, the profile of N₂⁺ 391 nm is also wide.

The emission shapes of Ne 703 nm measured at 2.5 kV, Ar 763 nm, Kr 760 nm and Xe 828 nm seem like a temporal and spatial superposition of He 706 nm and N₂⁺ 391 nm multiplied with different factors. That is, He and Ne driven plasmas operated at a low voltage seem to have similar discharge behaviour, whereas Ne operated at a high voltage, Ar, Kr and Xe driven plasmas share another discharge behaviour.

In addition, it can be seen clearly from the two-dimensional colour plots of these species that there is no emission in the first tens of nanoseconds of the discharge for each wavelength. As mentioned above, a homebuilt square wave generator was used to apply the high voltage. It does not reach the setting voltage immediately but takes a short time. As a result, the discharge is not initiated until the applied electric field exceeds the breakdown threshold of a discharge gas. As a grounded ring is applied to the Xe-F μ TP, which speeds up the change of the electric field. The ignition of the Xe plasma as well as the emission of Xe 828 nm is thus earlier.

Usually, the temporally and spatially resolved data are presented as a two-dimensional colour plot in propagation time and position of a plasma as shown on the left side of Figure 4.6. However, this kind of colour plot has a low resolution for the time as the emission before and after the instant of time ($t - n$ and $t + n$) are also contributing to the actual intensity. Furthermore, when more than one peak is present at different positions at the same moment, the smaller ones will be covered and not recognised. Therefore, the optical

4.2 Spectroscopic Characterisation of the F μ TP

emission intensities of species at different instants of time are extracted and replotted as one-dimensional line plots, namely the emission intensities as a function of position for multiple moments.

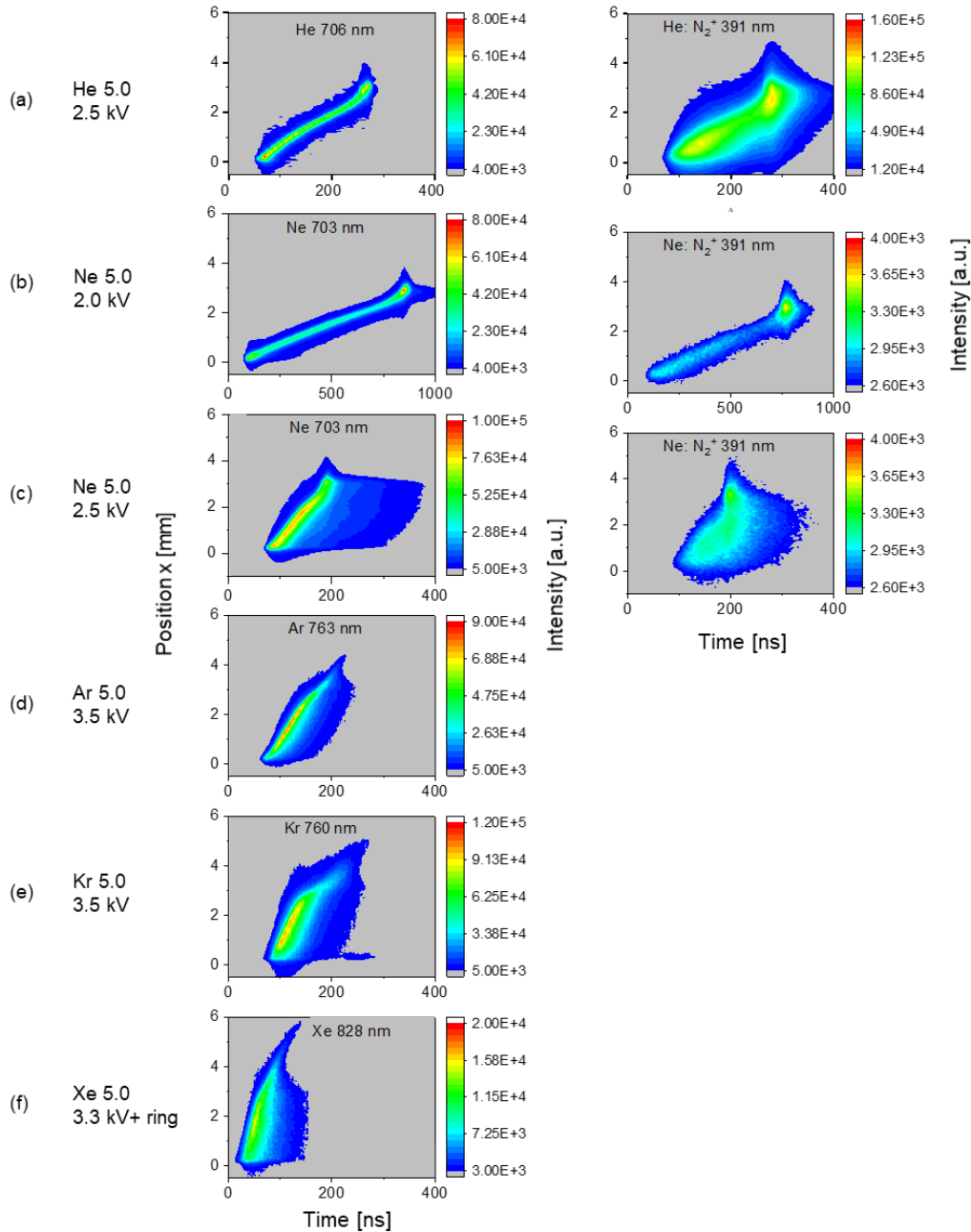


Figure 4.5: Spatial and temporal development of various noble gases driven plasmas during the positive half cycle. (a) He 706 nm and N₂⁺ 391 nm measured in He-F μ TP at 2.5 kV, (b) Ne 703 nm and N₂⁺ 391 nm measured in Ne-F μ TP at 2.0 kV, (c) Ne 703 nm and N₂⁺ 391 nm measured in Ne-F μ TP at 2.5 kV, (d) Ar 763 nm measured in Ar-F μ TP at 3.5 kV, (e) Kr 760 nm measured in Kr-F μ TP at 3.5 kV, (f) Xe 828 nm measured in Xe-F μ TP at 3.3 kV with a grounded ring.

4.2.3 Plasma Development Within the Capillary

This section will discuss in detail the ignition and propagation of a *He*, *Ne*, *Ar*, *Kr* and *Xe* driven plasma inside the capillary during the positive half cycle.

Figure 4.6 shows the two-dimensional colour plots on the left side as well as the position-dependent plots on the right side for *He* 706 nm and N_2^+ 391 nm signals. The light blue background represents the positions inside the capillary. The position of 0 mm represents the electrode tip and 3 mm is the end of the discharge capillary, with further positions ($x > 3$ mm) extending outside of the capillary into the ambient surrounding. The corresponding instants of time are inserted in the subgraphs.

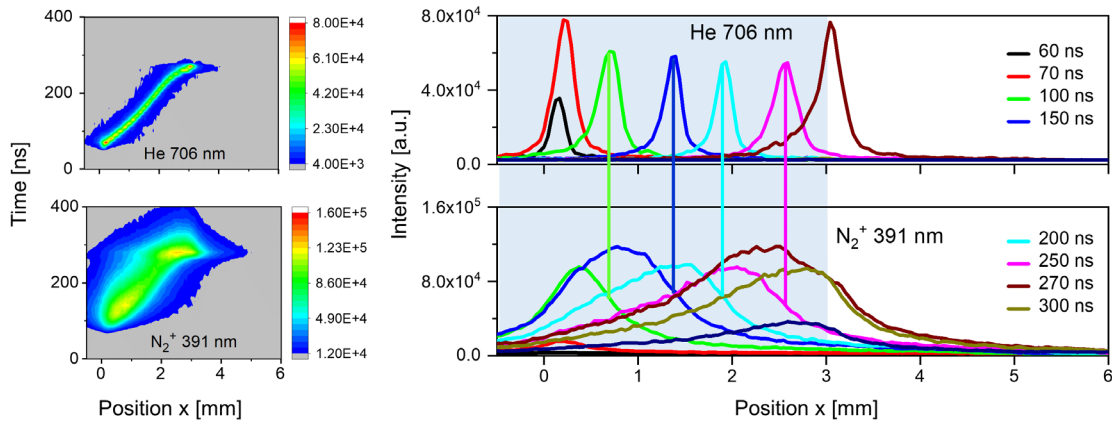


Figure 4.6: Two-dimensional colour plot in time and position as well as the position dependent plots at different instants of time in the positive half cycle for *He* 706 nm and N_2^+ 391 nm in a *He* plasma. The applied voltage is 2.5 kV. The flow rate of discharge gas is 50 sccm. Adapted with the permission from [91], Copyright 2024 Elsevier.

The shapes of *He* 706 nm are almost symmetric as can be seen in the position-dependent subgraph. The shape and the constant position-full width at half maximum (p-FWHM) of *He* 706 nm are stable, which only shift in time. The peak of *He* 706 nm reaches the capillary end ($x = 3$ mm) at 270 ns.

The emission intensity of *He* 706 nm is an indirect measurement of the density of He^M as explained in Section 3.2.2. Since the N_2^+ B $^2\Sigma_u^+$ state can be produced by Penning ionisation and the signal of N_2^+ 391 nm is then measured by the transition from N_2^+ B $^2\Sigma_u^+$ to N_2^+ X $^2\Sigma_g^+$, information about He^M can be supplemented by measuring and understanding the signal of N_2^+ 391 nm.

4.2 Spectroscopic Characterisation of the F μ TP

The emission intensities of He 706 nm and N₂⁺ 391 nm are increasing in the vicinity of the electrode tip from 60 ns. Between 100 ns and 270 ns, the peaks of both species shift along the capillary. The maximum of He 706 nm is always in front of the maximum of N₂⁺ 391 nm ($x_{He} > x_{N_2^+}$) as marked by vertical lines. This is related to the generation mechanisms of He^{**} and N₂⁺ B ²Σ_u⁺.

When the positive half cycle begins, a positive potential is applied at the tip of the electrode and reaches the set voltage ($t_1 > 0$, $x = 0$), forming an electric field. The electrons are attracted by the positive potential and accelerated in the electric field. He atoms will be excited by collisions with energetic electrons to He^{**}, He^{*} and He^M ($x_1 > 0$). He^{**} decays to He^{*} by emitting light at a wavelength of 706 nm and further to He^M. Through Penning ionisation, N₂⁺ B ²Σ_u⁺ are generated at the position of x_1 .

A new transient potential is created with N₂⁺ at the position of x_1 . This is responsible for the next round of excitation of He^{**}, He^{*} and He^M at the next position x_2 ($x_2 > x_1$). A further potential will be initiated by that new He^M at the position of x_2 . As a result, the excitation and ionisation waves move forward. Until a transient potential is not sufficient to sustain the next round of excitation. In this sense, the plasma development is the propagation of the excitation and ionisation waves. The stationary plasma visible to the naked eye is the repetitive development process of the excitation and ionisation waves [99-102]. A portion of the N₂⁺ ions attach on the capillary inner wall during the propagation along the capillary.

The characteristic of a Ne-F μ TP was first investigated when the voltage was applied at 2.0 kV. The shapes of Ne 703 nm are almost symmetric at each time, as shown in Figure 4.7.

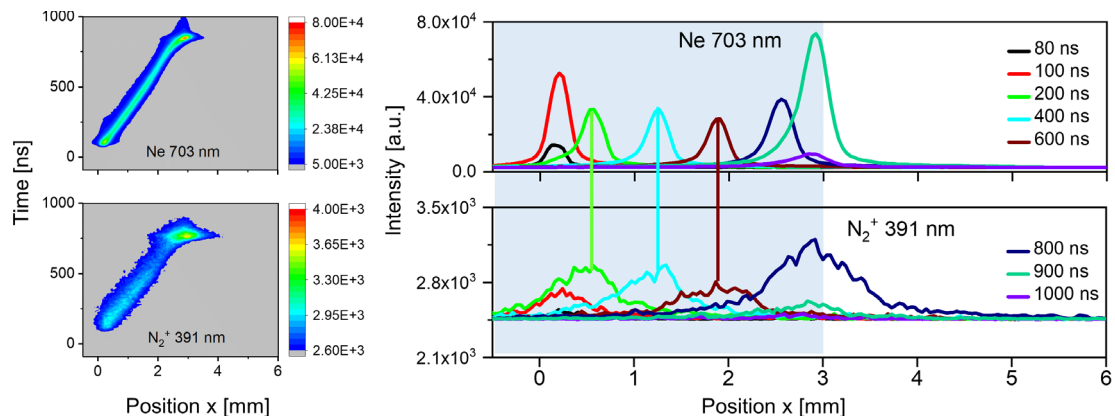


Figure 4.7: Two-dimensional colour plot in time and position as well as the position dependent plots at different instants of time in the positive half cycle for the Ne 703 nm and N₂⁺ 391 nm line in a Ne plasma. The applied voltage is 2.0 kV. The flow rate of discharge gas is 50 sccm. Adapted with the permission from [94], Copyright 2025 Elsevier.

Chapter 4 Discharge Mechanisms of the F μ TP

This is similar to the shape of *He* 706 nm measured in a *He*-F μ TP. By comparing the maximum intensity of *Ne* 703 nm and N₂⁺ 391 nm, it is observed that they reach the same position at the same instant of time, as marked by coloured vertical lines. As given in Equation 4.2, radiative transition of *Ne*^{*} to a specified excited state of *Ne*^M results in the emission of radiation with a wavelength of 703 nm. This means that *Ne*^{*} and N₂⁺ B ²Σ_u⁺ are produced at the same time.

Usually, the excited states of a noble gas are considered to be generated by the collisions of energetic electrons with noble gas atoms. In addition, the energy levels of *Ne*^{*} and N₂⁺ B ²Σ_u⁺ are close as shown in Figure 4.2. That is, both N₂ and *Ne* atoms are suitable collision partners for energetic electrons, generating *Ne*^{*} and N₂⁺ B ²Σ_u⁺ directly. As the concentration of N₂ in *Ne* 5.0 is 3 ppm, only a small number of N₂⁺ B ²Σ_u⁺ is produced. Even if *Ne*^M have a long lifetime, their energy levels are lower than those of N₂⁺ B ²Σ_u⁺. Therefore, N₂⁺ B ²Σ_u⁺ cannot be generated by Penning ionisation as in a *He* plasma. This is also the main reason why the emission intensity of N₂⁺ 391 nm is low in a *Ne*-F μ TP.

The energy level of N₂⁺ X ²Σ_g⁺ (15.6 eV) is lower than those of *Ne*^M (16.6 eV and 16.7 eV) and the energy difference between them is small (1.0 eV and 1.1 eV). This is beneficial for Penning ionisation. However, the presence of N₂⁺ X ²Σ_g⁺ cannot be detected directly by spectroscopy. On the one hand, the wavelengths associated with the transition of N₂⁺ X ²Σ_g⁺ to lower energy levels are missing or unknown. It is impossible to detect them by emission spectroscopy. On the other hand, the dimension of the F μ TP source with an inner diameter of 250 μm is small. The laser diode absorption spectroscopy measurements cannot be carried out. Nevertheless, it is reasonable to expect that a large amount of N₂⁺ X ²Σ_g⁺ is generated by Penning ionisation, as N₂⁺ B ²Σ_u⁺ is generated in a *He* plasma.

Similar to N₂⁺ B ²Σ_u⁺, which guides the excitation propagation of a *He*-F μ TP within the capillary, N₂⁺ X ²Σ_g⁺ could also form a transient potential. Such potential is responsible for the propagation of the excitation through the capillary in a *Ne*-F μ TP. Therefore, *He*-F μ TP and *Ne*-F μ TP operated at 2.0 kV have the same discharge mode that N₂⁺ are the main ions responsible for the development of excitation and ionisation inside the capillary.

The two-dimensional colour plots and position-dependent plots of *Ar* 763 nm, *Kr* 760 nm and *Xe* 828 nm are presented in Figure 4.8. The shapes of these species exhibit obvious asymmetry and wide p-FWHM compared to the emission profiles of *He* 706 nm and *Ne* 703 nm. They exhibit an obvious wing on the left side of the maximum intensity. Specifically, the wing always lags behind the respective maximum of each signal at the same time within the capillary.

4.2 Spectroscopic Characterisation of the F μ TP

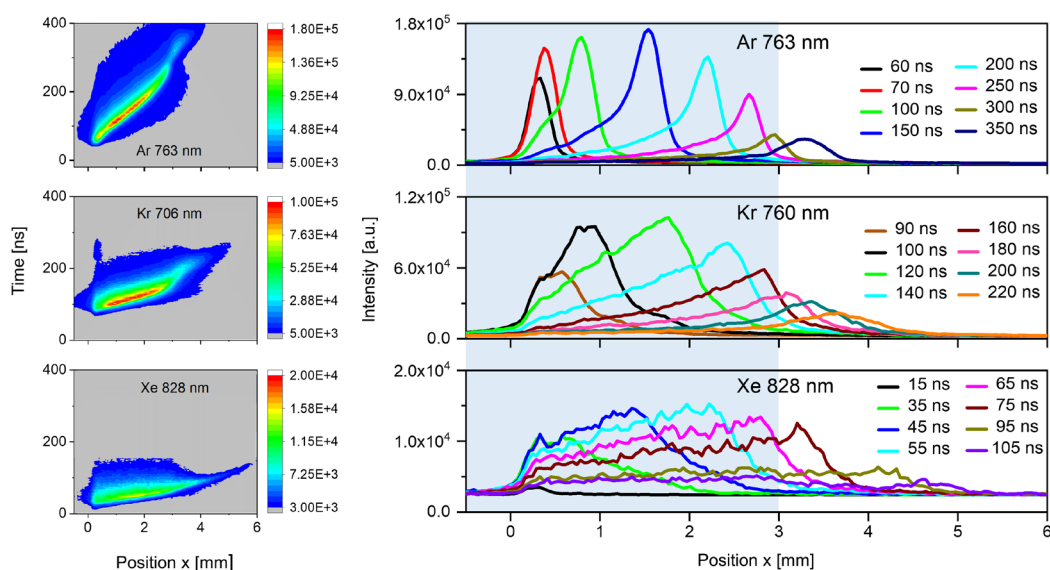


Figure 4.8: Two-dimensional colour plots in time and position and the position dependent plots at different instants of time in the positive half cycle for Ar 763 nm, Kr 760 nm, Xe 828 nm. The applied voltage is 3.5 kV, 3.5 kV and 3.3 kV with a grounded ring for Ar-, Kr and Xe-F μ TP, respectively. The flow rate of discharge gas is 50 sccm.

In an Ar-, Kr- and Xe-F μ TP, no $N_2^+ B^2\Sigma_u^+$ are generated. Based on the finding that a small amount of $N_2^+ B^2\Sigma_u^+$ is produced by electron collisions in a Ne-F μ TP, it is reasonable to assume that a small amount of $N_2^+ X^2\Sigma_g^+$ will be produced by electron collisions in an Ar-F μ TP. This possibility arises from the comparable ionisation energies of Ar atoms and nitrogen molecules. In a Kr- and Xe-F μ TP, $N_2^+ X^2\Sigma_g^+$ for sure is absent as explained above. Therefore, in an Ar-, Kr- and Xe-F μ TP, neither $N_2^+ B^2\Sigma_u^+$ nor $N_2^+ X^2\Sigma_g^+$ play a significant role in the propagation of excitation and ionisation inside the capillary, but other ions.

In order to figure out the excitation and ionisation propagation of Ar, Kr and Xe plasmas, Ar 763 nm is selected as a representative. This choice is based on the similar spatial emission behaviour observed for Ar 763 nm, Kr 760 nm and Xe 828 nm. The position dependent plots of Ar 763 nm are reshown in Figure 4.9 (left). At each time point, the emission intensity is normalized to the maximum value of each spectrum, with the measured maximum intensities annotated in the upper right corner of each subplot. The corresponding moments are given in ns and inserted into subplots. In addition, the position dependent plots at several instants of time for He 706 nm (black line) and N_2^+ 391 nm (red line) measured in a He-F μ TP at 2.5 kV are also reshown in Figure 4.9 (right) to give a direct comparison between these plasmas.

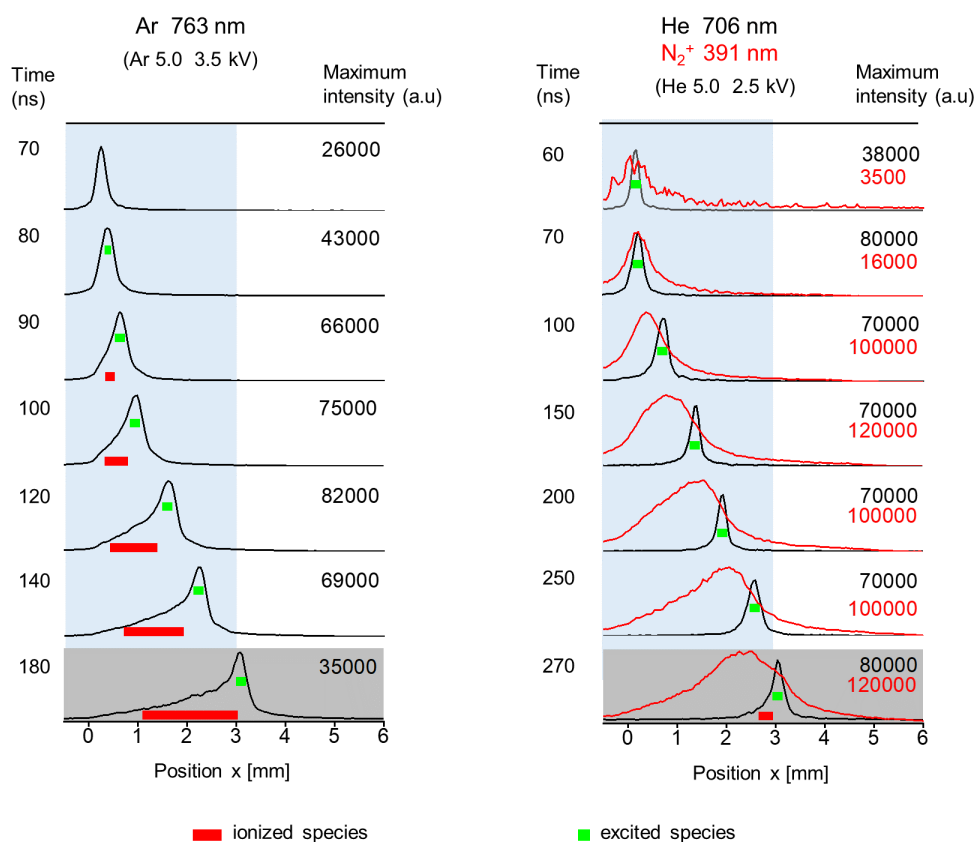


Figure 4.9: The propagation of *Ar* and *He* driven plasmas inside the discharge capillary in the positive half cycle. The position dependent plots at different instants of time for *Ar* 763 nm measured in an *Ar* driven plasma at 3.5 kV (left), *He* 706 nm (black line) and N_2^+ 391 nm (red line) measured in a *He* driven plasma at 2.5 kV (right). The flow rate of discharge gas is 50 sccm. The subplot with grey background represents the excitation propagation reaching the end of the capillary. The red rectangles represent the ionised species and the green dots represent the excited species. Adapted with the permission from [93], Copyright 2024 Springer.

The excitation reaches the end of the capillary ($x = 3$ mm) at 180 ns in an *Ar*-F μ TP. The plots of *Ar* 763 nm have broader shapes than those of *He* 706 nm. There is an obvious wing on the left side of the maximum of *Ar* 763 nm, as marked by a red bar, leading to a distinctly asymmetric shape. The maximum of N_2^+ 391 nm also locates behind the maximum of *He* 706 nm. The distributions of *Ar* 763 nm are analogical to the superposition of N_2^+ 391 nm and *He* 706 nm multiplied with different factors. A simulated result of superimposing two Gaussian peaks is shown in Figure B.3 of the Appendix.

As given in Equation 4.3, radiation with a wavelength of 763 nm is emitted during the transition from the Ar^* to the Ar^M state. This means that Ar^* is generated and detected at the same time in continuous positions. One possible interpretation is that, in addition to the

4.2 Spectroscopic Characterisation of the F μ TP

Ar^* state produced directly by collisions of energetic electrons with Ar atoms, higher laying states of Ar capable of decaying to Ar^* and thereby to Ar^M might also be produced along the capillary. In opposite to the excited and even higher excited states of Ar , Ar^+ is charged and therefore is to be expected at another position than Ar^* . Furthermore, the production of excited species depends on the presence of the potential formed by ions, as learned in a He -F μ TP. In this sense, the wing of Ar 763 nm might be contributed by Ar^+ .

In a He -F μ TP, a high amount of N_2^+ can be generated by Penning ionisation. N_2^+ ions are considered to be the key ions that guide the plasma propagation forward. However, no suitable molecules or atoms with an ionisation energy lower than that of Ar^M are present in Ar 5.0. Consequently, none could fulfil the conditions for Penning ionisation, as in a He -F μ TP, to guide Ar plasma propagation forward.

A dopant can be added to Ar 5.0 to ensure that the resulting mixture satisfies the conditions required for Penning ionisation. The ionisation level of the dopant should be lower than that of the Ar^M to ensure effective ionisation. Furthermore, the energy difference between the two should be as small as possible, as the probability of an effective collision between two substances is greatly influenced by the energy disparity [86].

In this thesis, propane (C_3H_8) with an ionisation energy of 10.9 eV is selected as the dopant. This energy is lower than the energy of Ar^M with 11.5 eV and 11.7 eV, as shown in Figure 4.10. In addition, the energy difference between Ar^M and the ionisation level of propane is small. The propane molecules in Ar perform the same reaction as the N_2 molecules in He ,

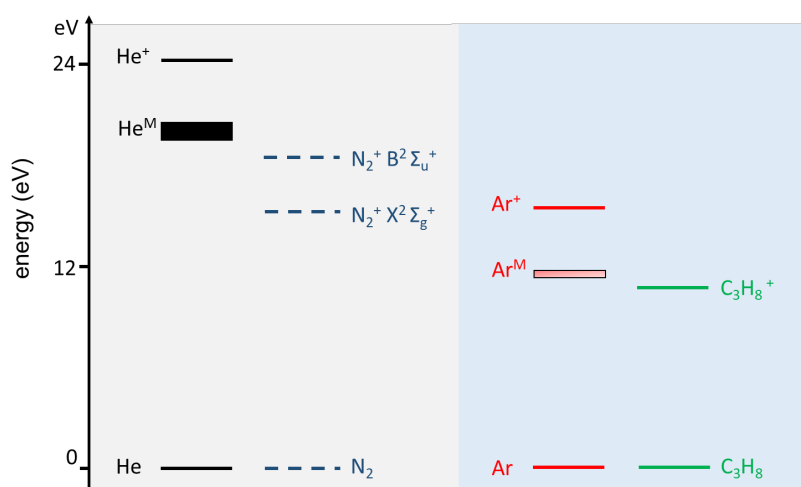


Figure 4.10: Graphical illustration of energy levels for Penning ionisation processes with He - N_2 (left, light grey background) and Ar - C_3H_8 mixtures (right, light blue background).

Chapter 4 Discharge Mechanisms of the F μ TP

where the energy level of $N_2^+ B^2\Sigma_u^+$ with 18.8 eV is lower than He^M with 19.8 eV and 20.9 eV, as shown in Figure 4.10. Therefore, propane molecules can be Penning ionised by Ar^M . Propane was primarily used as an ignition aid to decrease the ignition voltage of an Ar driven plasma and was furthermore responsible for ionisation [103-105].

Figure 4.11 shows the position dependent plots of Ar 763 nm measured under different conditions. To make a visual comparison, the applied voltage for Ar-F μ TP is changed from 3.5 kV used above to 2.8 kV. In comparison with the Ar 763 nm measured in an Ar-F μ TP, the profiles of Ar 763 nm measured in an Ar-propane-F μ TP are narrower and closer to the profiles of He 706 nm. Specifically, the wing of Ar 763 nm becomes less distinct. In this case, propane ions play a role in the propagation of plasma. In conjunction with the analysis above, it suggests that the species represented by the wing of Ar 763 nm supports the plasma propagation in an Ar-F μ TP. That is, the wing of Ar 763 nm is contributed to Ar^+ .

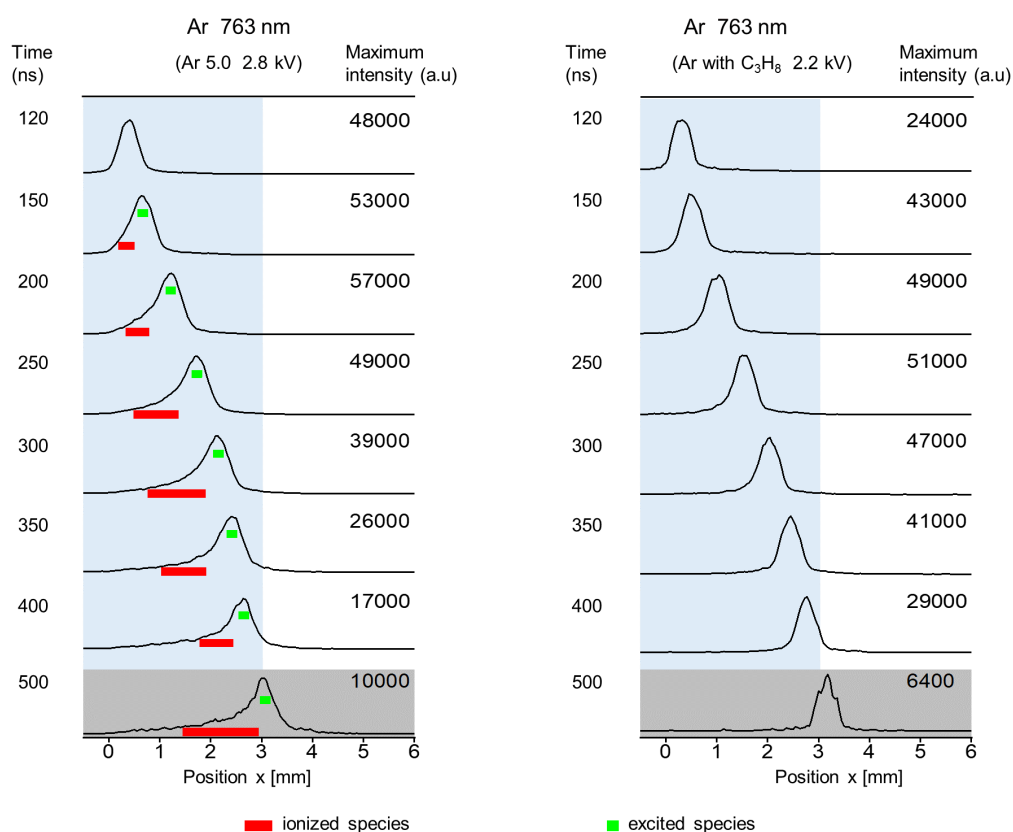


Figure 4.11: The propagation of Ar and Ar with 2000 ppm propane driven plasmas inside the discharge capillary in the positive half cycle. The position dependent plots at different instants of time for Ar 763 nm measured in Ar-F μ TP at 2.8 kV (left) and in Ar-propane-F μ TP at 2.2 kV (right). The subplot with grey background represents the excitation propagation reaching the end of the capillary. The red rectangles represent the ionised species and the green dots represent the excited species. The flow rate of discharge gas is 50 sccm. The concentration of propane in Ar is 2000 ppm. Adapted with the permission from [91], Copyright 2024 Elsevier.

4.2 Spectroscopic Characterisation of the F μ TP

The excitation reaches the end of the capillary ($x = 3$ mm) at 500 ns in an *Ar*-F μ TP driven at 2.8 kV and an *Ar*-propane-F μ TP with 2000 ppm propane driven at 2.2 kV. The average propagation velocity of an *Ar*-F μ TP is considered to be comparable to that of an *Ar*-propane-F μ TP. It is well established that the propagation velocity is related to the potential through the capillary. The higher the potential, the stronger the resulting electric field. This stronger field accelerates electrons more rapidly to a necessary kinetic energy. Consequently, the excitation and ionisation reach a specific position earlier. In this sense, the potential of an *Ar*-propane-F μ TP with 2000 ppm propane at 2.2 kV is comparable to that of the *Ar*-F μ TP at 2.8 kV. Pure *Ar* cannot be ignited with an applied voltage of 2.2 kV.

Due to the contribution of propane ions generated through Penning ionisation, the ignition and maintenance voltage for an *Ar*-propane-F μ TP is relatively low. In order to generate and sustain the same amount of Ar^+ in an *Ar*-F μ TP as Ar^M in an *Ar*-propane-F μ TP, a higher electron density with higher energy is needed for *Ar*-F μ TP. These electrons can be realised with a higher voltage. The high voltage needed in an *Ar*-F μ TP further reveals that Ar^+ is responsible for plasma propagation in the *Ar* plasma.

The transition of a positive ion (A^+) to a high-energy neutral excited state (A^{**}) involves electron capture, followed by radiative deexcitation to lower excited states (A^*) through near-infrared (NIR) photon emission [106,107]. This is also suitable for Ar^+ . Ar^+ is depopulated by NIR emission to Ar^* , with the transition of Ar^* to Ar^M , the signal of 763 nm can be detected once more. Thus, Ar^+ is measured in addition to the excited *Ar* states. Although propane ions are generated in an *Ar*-propane-F μ TP and guide the excitation and ionisation of the plasma, the shapes of *Ar* 763 nm are still not perfectly symmetric. This means that Ar^+ is still generated in an *Ar*-propane-F μ TP.

Going back to the shapes of *He* 706 nm (black line) shown in Figure 4.9, even if they are almost symmetric, a small wing on the left side of the maximum is still visible in the subgraph at 270 ns. It is marked with a red bar. At this moment, the plasma propagates to the end of the capillary. The wing could be attributed to He^+ , as a small amount of Ar^+ is still generated and detected in *Ar*-propane-F μ TP. Similar to Ar^+ , He^+ captures an electron and then is depopulated by NIR emission to He^{**} . With the transition of He^{**} to He^* , the signal of 706 nm can be detected once more. The emission of He^+ and He^{**} overlaps to some extent at this position, leading to a higher emission intensity of *He* 706 nm than at lower positions.

Similarly, Kr^+ and Xe^+ can also capture electrons and are depopulated by NIR emission to Kr^* and Xe^* , respectively. With the transition of Kr^* to Kr^M and Xe^* to Xe^R , as given in Equations 4.4 and 4.5, these ions are detected. These ions and excited atoms are

Chapter 4 Discharge Mechanisms of the F μ TP

generated by collisions between the high energy electrons and atoms at ground state. As verified that the wing of Ar 763 nm is attributed to Ar⁺, the wings of Kr 760 nm and Xe 828 nm are attributed to the corresponding noble gas ions. The maxima are attributed to excited states. These noble gas ions play an important role in the propagation of the excitation and ionisation. A portion of them attach to the capillary inner wall.

Since the excitation energy of Ne^M (16.6 eV and 16.7 eV) with a long lifetime is lower than the energy level of He^M (19.8 eV and 20.9 eV), it is easy to explain why the ignition voltage of Ne is lower than that of He. From that point of view, the ignition voltages of He, Ne, Ar, Kr and Xe should decrease in sequence, but the actual measurements show that the ignition voltage of Ar is higher than that of He. This contradiction can be explained by the correlation of the energy levels of He^M, Ar^M, N₂⁺ and the lifetime of Ar⁺.

In an Ar plasma, the Ar^M states do not have ion states of other species, such as N₂⁺ B ²Σ_u⁺ state in the case of He^M below their states. As a result, no ions of other species can be generated through Penning ionisation to sustain the plasma. It has been demonstrated that Ar atoms need to be ionised to sustain plasma propagation. The lifetimes of the excited states are shorter than those of the metastable states [41]. This is also appropriate for the Ar⁺ state. Due to the long lifetime of He^M, a large number of N₂⁺ B ²Σ_u⁺ are generated by Penning ionisation in a He plasma. In order to generate and maintain the same amount of Ar⁺ in an Ar plasma as N₂⁺ in a He plasma, the Ar plasma needs a higher electron density. This is usually achieved by an increase of the applied voltage.

This in turn would verify the supposed generation and importance of Ar⁺ for the excitation and ionisation of Ar plasmas in an indirect way. This is the first time that the element ions can be distinguished from excited noble gas species by means of emission spectroscopy in cold plasmas like these, which are employed for soft ionisation.

Noble gas ions play a significant role in the propagation of the excitation and ionisation in Ar, Kr and Xe plasmas. As their ionisation energies decrease progressively from Ar to Xe, the ignition voltages for them should decrease sequentially. In contrast, the ignition voltages are increasing in order for Ar, Kr, and Xe plasmas. This might be related to the diameters of these noble gas atoms.

With the same mass flow through the capillary, the same number of atoms moves through the capillary for each of the discharge gases. It is known that the cross section of Ar, Kr, and Xe is getting bigger. That is, the mean free path of electrons is getting shorter, so that the electrons will not gain enough energy in a certain electric field to ionise atoms. One

4.2 Spectroscopic Characterisation of the F μ TP

common solution is to increase the applied voltage and thus the electric field. Further efforts are needed to understand this well. It exceeds the scope of this thesis.

An ionisation source such as F μ TP is used as a soft ionisation source for MS and IMS applications. Its stable operation is crucial for achieving reliable results over several hours. Specifically, the source should maintain consistent propagation in time, emission intensity, and discharge behaviour for several hours. It is not the case when Ne is used for the working gas operated at 2.0 kV. The 2D colour plots as well as the time dependent plots of Ne 703 nm measured at different operation times are shown in Figure B.4 of the Appendix. To keep the plasma stable for hours, even days, the operation voltage for Ne-F μ TP was increased from 2.0 kV to 2.5 kV. The gate width and the step width were set to 5 ns in the case of a Ne-F μ TP at 2.5 kV to gain a higher temporal and spatial resolution.

Figure 4.12 shows the position dependent emission plots of Ne 703 nm measured at different applied voltages. To visually compare the discharge behaviour of the Ne-F μ TP

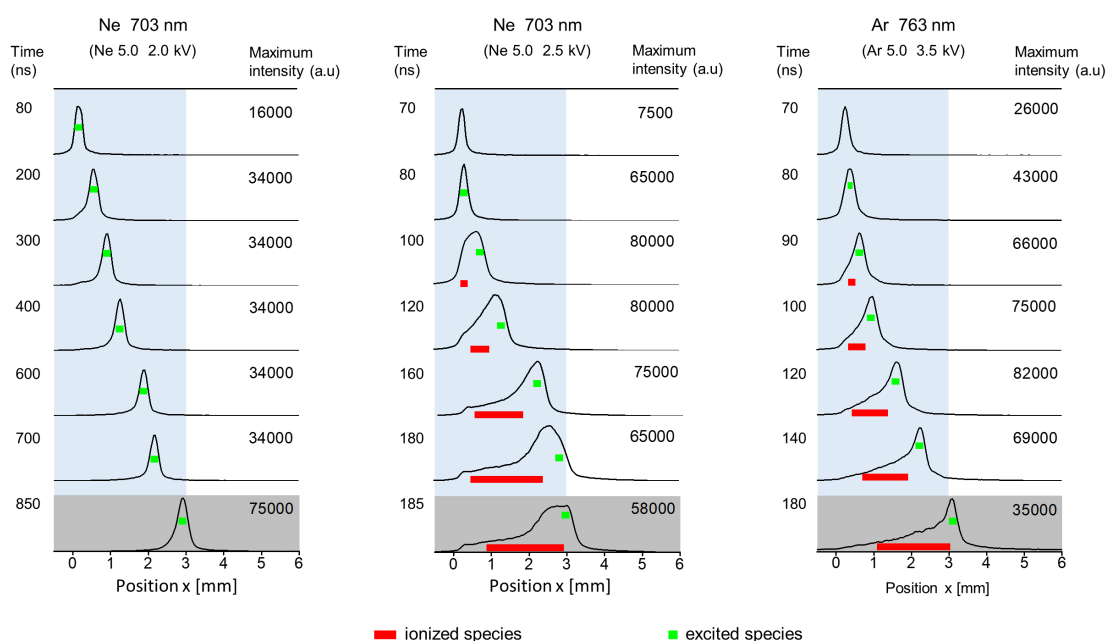


Figure 4.12: Comparison of discharge behaviour of Ne driven plasmas operated at different voltages inside the discharge capillary in the positive half cycle. The position dependent plots at different instants of time for Ne 703 nm measured in Ne-F μ TP at 2.0 kV (left) and 2.5 kV (middle), and Ar 763 nm measured in Ar-F μ TP at 3.5 kV (right). The subplot with grey background represents the excitation propagation reaching the end of the capillary. The red rectangles represent the ionized species and the green dots represent the excited species. The flow rate of discharge gas is 50 sccm. Adapted with the permission from [94], Copyright 2025 Elsevier.

Chapter 4 Discharge Mechanisms of the F μ TP

operated at different voltages, the position dependent plots of Ar 763 nm measured in an Ar-F μ TP at 3.5 kV are added to Figure 4.12.

The propagation velocity of the excitation and ionisation at a voltage of 2.5 kV is significantly increased compared to the case of 2.0 kV. As a result, the time required for the excitation to reach the end of the capillary is reduced from 850 ns to 185 ns. This is nothing new, but the signal of Ne 703 nm measured at 2.5 kV exhibits a completely different shape compared to the signal of Ne 703 nm obtained at 2.0 kV. The emission shape of Ne 703 nm is changing from a shape similar to He 706 nm to that of Ar 763 nm, Kr 760 nm and Xe 828 nm. At 100 ns, a wider shape of Ne 703 nm in a Ne_{2.5 kV}-F μ TP is beginning to observe. The wing becomes very visible afterwards, as marked by red bars. This means that the discharge behaviours of Ne plasmas operated at different voltages differ.

In a Ne_{2.5 kV}-F μ TP, a significant amount of Ne⁺ can be generated in addition to excited Ne species. This is attributed to the higher electron density and electron energy compared to the Ne_{2.0 kV}-F μ TP case. Similar to other noble gas ions, Ne⁺ captures an electron and then is depopulated by NIR emission to Ne^{*}. With the transition from Ne^{*} to Ne^M, Ne⁺ is measured by the 703 nm emission.

Although Ne⁺ is generated inside the capillary in the case of a Ne_{2.5 kV}-F μ TP, the emission intensity of N₂⁺ 391 nm is still very low. The 2D colour and position dependent plots of Ne 703 nm as well as N₂⁺ 391 nm measured in Ne_{2.5 kV}-F μ TP are shown in Figure 4.13. The maximum intensities of Ne 703 nm and N₂⁺ 391 nm do not appear simultaneously at the same position as observed in Ne_{2.0 kV}-F μ TP. Instead, the Ne 703 nm peak is in front of the N₂⁺ 391 nm peak, as indicated by the vertical lines. This is similar to He 706 nm and N₂⁺ 391 nm measured in a He-F μ TP.

As explained above, N₂⁺ B ² Σ_u^+ and Ne^{*} are generated simultaneously by electron impact in a Ne_{2.0 kV}-F μ TP. This mechanism causes them to be produced at the same time. In other words, the generation mechanism of N₂⁺ B ² Σ_u^+ in a Ne_{2.5 kV}-F μ TP varies from that in a Ne_{2.0 kV}-F μ TP. As is known that N₂⁺ B ² Σ_u^+ are mainly generated by the collisions of He^M and N₂ in a He-F μ TP. Such collisional processes result in a position delay at the same moment. In other words, collisions between Ne species and N₂ X ¹ Σ_g^+ take place in a Ne_{2.5 kV}-F μ TP, generating N₂⁺ B ² Σ_u^+ . However, the emission intensity of N₂⁺ 391 nm is very low. Therefore, the amount of N₂⁺ B ² Σ_u^+ is very low in Ne_{2.5 kV}-F μ TP. For the same reason, it is reasonable to conclude that only a very small fraction of N₂⁺ X ² Σ_g^+ in an Ar-F μ TP and protonated water clusters in a Kr-F μ TP are produced. Nevertheless, the ionisation efficiencies of an Ar- and

4.2 Spectroscopic Characterisation of the F μ TP

Kr-F μ TP are comparable with those of a He- and Ne-F μ TP. Therefore, Penning ionisation and charge transfer outside the plasma are not the main mechanisms for soft ionisation.

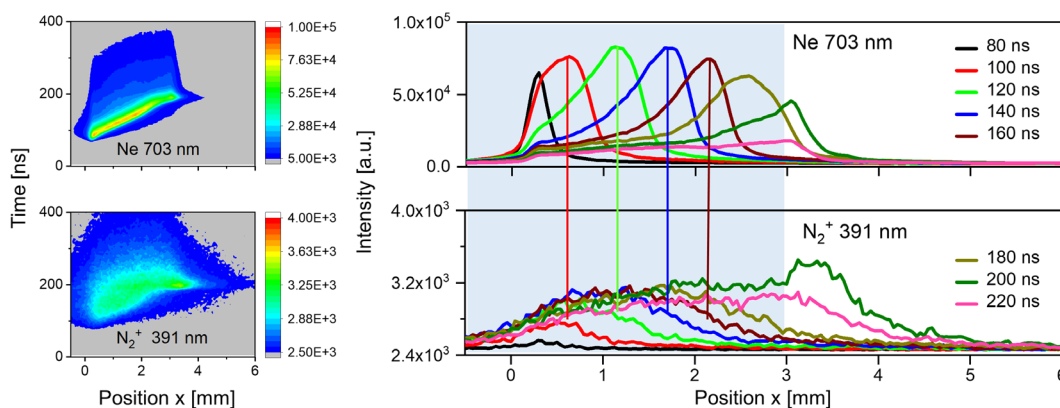


Figure 4.13: Two-dimensional colour plot in time and position and the position dependent plots at different instants of time in the positive half cycle for the Ne 703 nm (upper) and N₂⁺ 391 nm (lower) in a Ne plasma. The applied voltage is 2.5 kV. The flow rate of discharge gas is 50 sccm. Adapted with the permission from [94], Copyright 2025 Elsevier.

Similar to Ne 703 nm, the wing of He 706 nm becomes obvious when the applied voltage is increased in a He-F μ TP. The two-dimensional colour plots and position dependent plots of He 706 nm operated at various voltages are shown in Figure B.5 of the Appendix. That is, more He⁺ is generated at higher applied voltages. The appearance of distinct wings of Ne 703 nm as well as He 706 nm at higher applied voltages is a further piece of evidence that noble gas ions are generated and can be identified from the excited states.

Based on these results, the F μ TP can be divided into two discharge categories. He- and Ne-F μ TP operated at low voltage fulfill the first category. In this case, N₂⁺ are the main ions guiding the propagation of the excitation and ionisation in the capillary. The second category is that the noble gases must be ionised so that their charges create a transient potential. With such a transient potential, noble gas atoms can be excited by electrons accelerated in the electrical field initiated by the potential. Ar-, Kr- and Xe-F μ TP belong to the second category. He- and Ne-F μ TP fulfil characteristics of both categories when the applied voltage is increased.

A conclusion of the excitation and ionisation propagation process within the capillary is that the excitation propagation is in front of the ionisation propagation. In other words, the propagation of excitation is driven by the propagation of ionization.

Usually, the analytes are delivered by external setups such as gas chromatography headspace to the reaction region, where the analytes are ionised. The ions are then

Chapter 4 Discharge Mechanisms of the F μ TP

transported and detected by mass spectrometer. Therefore, the investigation of the propagation of the excitation and ionisation in front of the detector is of great interest to provide a better understanding on the ionisation of analytes.

4.2.4 Plasma Development to Ambient Surrounding

This section focuses on the propagation of the excitation and ionisation to ambient surrounding during the positive half cycle.

Figure 4.14 shows the propagation of He 706 nm (black line) and N $_2^+$ 391 nm (red line) from the inside of the capillary to the ambient air. Compared to the Figure 4.9, the

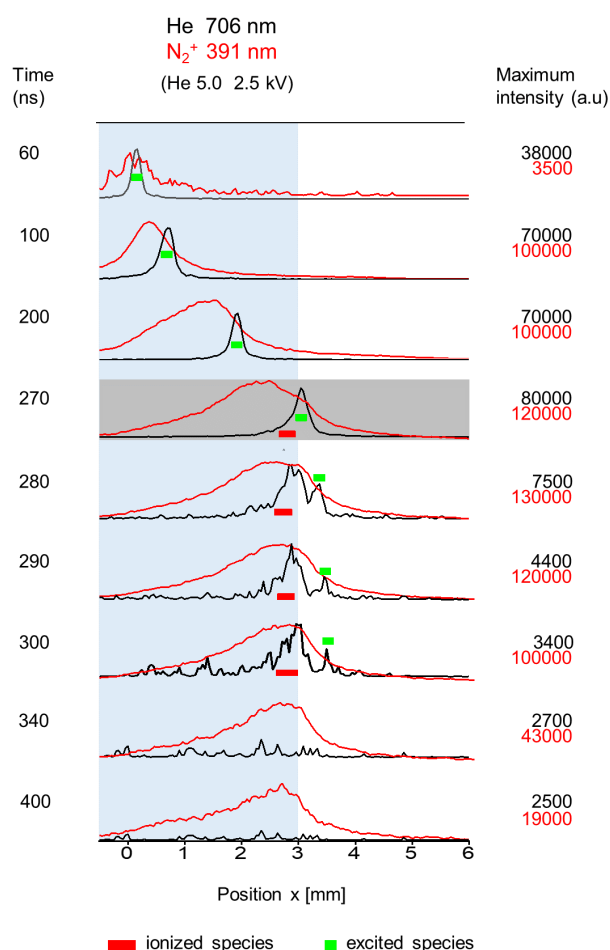


Figure 4.14: The propagation of a He driven plasma from inside the capillary to ambient surrounding. The position dependent plots at different instants of time for the 706 nm (black line) and N $_2^+$ 391 nm (red line) measured in He-F μ TP at 2.5 kV. The subplot with grey background represents the excitation propagation reaching the end of the capillary. The red rectangles represent the ionised species and the green dots represent the excited species. The flow rate of the discharge gas is 50 sccm. Adapted with the permission from [93], Copyright 2024 Springer.

4.2 Spectroscopic Characterisation of the F μ TP

propagation of excitation and ionisation at later instants of time is added. The grey background shows that the excitation reaches the end of the capillary at the given instant of time at 270 ns. The *He* 706 nm signal is split into two signals starting at 280 ns. One reaches in the vicinity of the capillary outlet at 300 ns and stops propagating further, as marked by a red bar. The other, marked by a green square, moves into the ambient surrounding until it vanishes.

Following the track of N₂⁺ 391 nm signal, the maximum stops in front of the capillary outlet and begins to decrease from 280 ns. This occurs despite the fact that the concentration of N₂ is increasing ($x > 3$ mm). It can be seen clearly that the shapes of N₂⁺ 391 nm remain constant. Only the emission intensity diminishes from 280 ns, ultimately declining to zero. Such signal results from the recombination of N₂⁺ B ²Σ_u⁺ attached to the inner wall of the discharge capillary.

Similar to the N₂⁺, it is suspected that the signal of *He* 706 nm stopping in the vicinity of the capillary outlet is attributed to the recombination of *He*⁺. On the contrary, the signal observed beyond the capillary probably attributes the emission of *He*^{**}. On the one hand, the shape of *He* 706 nm outside the capillary is narrow. On the other hand, the ionisation level of the *He* atom is higher than its excitation level. Therefore, it is considered that *He*^{**}, rather than *He*⁺, is generated by the collision of energetic electrons with *He* atoms in the ambient surrounding.

It is interesting that even if the ionisation wave of *He*⁺ and N₂⁺ B ²Σ_u⁺ does not propagate in ambient surrounding, the development of excitation wave (green squares) continues to proceed in ambient surrounding, as shown in the subplots from 280 ns to 300 ns. Based on the understanding of the propagation of excitation and ionisation within the capillary, where the propagation of ionisation drives the propagation of excitation. A transient potential must develop outside the capillary. Such potential attracts electrons, which are accelerated and then collide with *He* atoms, generating excited *He* species. Otherwise, the propagation of excitation will also stop in the vicinity of the capillary outlet and dissipate over time.

As the concentration of *He* is decreasing and the concentration of the air components is increasing with increasing position in the ambient surrounding ($x > 3$ mm), N₂⁺ X ²Σ_g⁺ and ions of other species might be generated in the ambient surrounding. Additionally, the energy of these N₂⁺ X ²Σ_g⁺ states can be quenched due to collisions with air components such as O₂ and H₂O, forming ions such as O₂⁺ and H₃O⁺. These ions can also create a

Chapter 4 Discharge Mechanisms of the F_μTP

potential in the ambient surrounding, eventually leading to the excitation of *He* atoms and the ionisation of air components. This process continues until the created potential is no longer sufficient to sustain the excitation of *He* atoms. However, the ion species of air components cannot be measured directly because of missing or unknown emission wavelengths. Figure 4.15 shows the propagation of Ne 703 nm from inside of the capillary to ambient surrounding.

Compared to the Figure 4.12, the propagation of excitation and ionisation at later instants of time is added. Similar to a *He* plasma, the propagation of ionisation wave of Ne⁺ stops

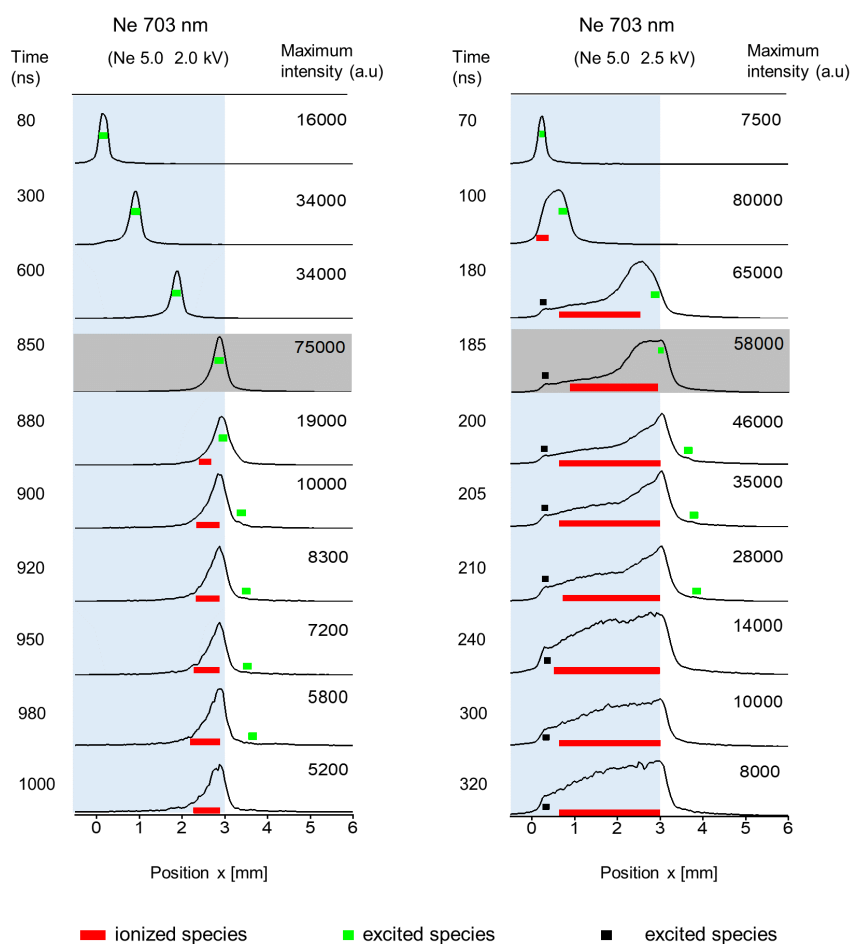


Figure 4.15: The propagation of Ne driven plasma from inside the capillary to ambient surrounding. The position dependent plots at different instants of time for Ne 703 nm measured at 2.0 kV (left) and at 2.5 kV (right). The flow rate of the discharge gas is 50 sccm. The subplot with grey background represents the excitation propagation reaching the end of the capillary. The red rectangles represent the ionised species. The green dots represent the excited species propagated along the discharge capillary to ambient air. The black dots represent the excited species located in vicinity of the electrode tip. Adapted with the permission from [94], Copyright 2025 Elsevier.

4.2 Spectroscopic Characterisation of the $F\mu TP$

in the vicinity of the capillary outlet as marked by red bars. While the excitation of *Ne* still develops beyond the capillary into the ambient surrounding over time as marked by the green squares. In the case of *Ne*- $F\mu TP$, the propagation of the excitation in ambient air is not obvious.

In the case of an *Ar*-, *Kr*- and *Xe*- $F\mu TP$, Ar^+ , Kr^+ and Xe^+ are the main ions of the ionisation propagation that guides the excitation to advance inside the capillary as explained above. Figure 4.16 shows the propagation of excitation and ionisation of *Ar*-, *Kr*- and *Xe*- $F\mu TP$ from inside the capillary to ambient surrounding. Compared to Figure 4.8, the emission intensity is normalized to the maximum value of each spectrum, with the measured maximum intensities annotated in the upper right corner of each subplot. The corresponding moments are given in ns and inserted into subplots. At 180 ns, 180 ns and 70 ns, the propagation of excitation reaches the end of the capillary, respectively. At later

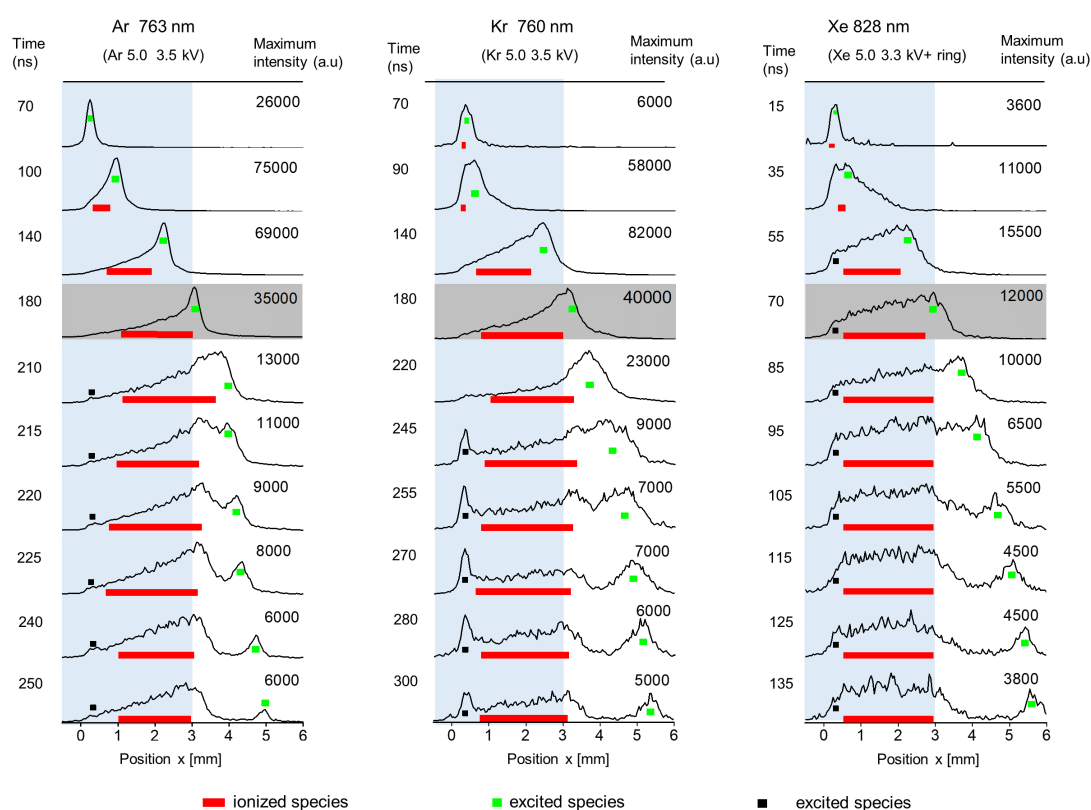


Figure 4.16: The propagation of *Ar*, *Kr* and *Xe* driven plasmas from inside the capillary to ambient surrounding. The position dependent plots at different instants of time for *Ar* 763 nm at 3.5 kV (left), *Kr* 760 nm at 3.5 kV (middle) and *Xe* 828 nm at 3.3 kV with a grounded ring (right). The subplot with grey background represents the excitation propagation reaching the end of the capillary. The flow rate of the discharge gas is 50 sccm. Adapted with the permission from [93], Copyright 2024 Springer.

Chapter 4 Discharge Mechanisms of the F μ TP

instants of time, the excitation of these three noble gas atoms propagates further into the ambient surrounding, while the ionisation of these atoms stops propagating forward.

In these cases, the separation of the ion signal (red bar) and the excited peak (green square) is more obvious than in case of a *He*- and *Ne*-F μ TP. In case of an *Ar*-F μ TP, the signals attributed to *Ar*⁺ and *Ar*^{*} can be distinguished completely from 215 ns. Similarly, this distinction occurs at 255 ns for a *Kr*-F μ TP and at 85 ns for a *Xe*-F μ TP.

In addition to the signals of noble gas ions (red bars) and excited species (green squares) moving forward in time in the capillary, a signal marked by black squares is always observed in the vicinity of the electrode. It does not propagate over time. These peaks are narrower than the emission of the noble gas ions. Thus, they cannot be classified as ions but should be the excited species. Interestingly, these peaks are not observed in the emission distributions of *He* 706 nm and *Ne* 703 nm at low applied voltage. This might be related to the discharge mode or the applied voltage. The reason for this emission is not yet understood. But it occurs in the capillary, which is not responsible for the soft ionisation in ambient surrounding. Therefore, an in-depth investigation will not be performed in this thesis.

4.2.5 Proposed Ionisation Mechanism in Ambient Surrounding

As found above, in all cases the excitation of noble gas atoms propagates further outside the capillary ($x > 3$ mm), whereas the observed propagation of ionisation wave stops in the vicinity of the capillary outlet. Then the question becomes of how the excitation could continue to develop forward. As explained above, the propagation of excitation can only take place when the propagation of ionisation occurs. Since the concentration of noble gas decreases and the concentration of ambient air increases at further positions, components of ambient air have to be ionised to guide further propagation of excitation in an open surrounding. The ion species might be N_2^+ , O_2^+ , H_3O^+ , etc.

The required energies for $N_2^+ X^2\Sigma_g^+$ is 15.6 eV, 12 eV for $O_2^+ X^2\Pi_g^+$ and 12.6 eV for H_2O^+ . In case of an *Ar*-, *Kr*- and *Xe*- F μ TP, the energies of the appropriate metastable states with long radiative lifetime are 11.5 eV and 11.7 eV, 9.9 eV and 10.6 eV, 8.3 eV and 9.4 eV, respectively. They are all lower than the required energies of N_2^+ , O_2^+ and H_2O^+ . Thus, none of these ions can be generated by Penning ionisation in these three cases.

Although the energy of *Ar*⁺ (15.8 eV) is higher than any of these ions, and the energy of *Kr*⁺ (14.0 eV) is also higher than those of both O_2^+ and H_3O^+ , the propagation of ionisation wave

4.2 Spectroscopic Characterisation of the F μ TP

of Ar⁺ and Kr⁺ stops in the vicinity of the capillary outlet. Consequently, the charge transfer between these species cannot be realised in the ambient surrounding. Furthermore, the energy of Xe⁺ (12.1 eV) is even lower than that of N₂⁺, O₂⁺, H₂O⁺. It is impossible to generate these ions by charge transfer. However, the intensity of reactant ions such as (H₂O)_nH⁺ (n = 2, 3) measured by MS is in the same range for all the plasmas mentioned above. Therefore, the Penning ionisation and charge transfer between components of the plasmas and these of ambient air outside the capillary are not the primary pathways for the production of ions that guide the propagation of the excitation forward as well as the reactant ions for soft ionisation.

One reasonable explanation is that the positive ions generated in the vicinity of the capillary outlet create a temporally and spatially limited potential and thereby an electric field. Electrons are accelerated in the electric field. Once the energy of the electrons is sufficient, the new excited noble gas species at the next position (x_n) can be generated by collision of the energetic electrons with the noble gas atoms. With the decay of the upper excited states to lower states, the emission signals are measured. Furthermore, as the concentration of ambient air components increases in ambient air, air components can be ionised by direct collision with these energetic electrons, generating ions such as N₂⁺, O₂⁺, H₃O⁺, etc.

These newly produced ions create a transient potential. This potential decreases in the space that an electric field is created, in which the electrons are accelerated again. As a result, the new excited species of noble gases and the ionised components of air are produced at the next position (x_{n+1}). This process is repeated in the open air until the transient potential is too low to support the next round of excitation and ionisation.

These ions generated in the open air on the one hand create a transient potential that facilitates the propagation of the excitation in the ambient surrounding. In the absence of the transient potential, the excitation of noble gas atoms would likely remain stationary, resulting in a gradual decrease in the emission intensities of the excited species. Alternatively, the excitation may shift to progressively lower positions over time until it is eventually extinguished, rather than continuing to advance. On the other hand, these ions are responsible for the soft ionisation. As a result, the soft ionisation is independent of the type of noble gas used for the discharge, but dependent on the number of ions forming the potential. Based on these results, it is assumed that a transient potential is responsible for the soft ionisation.

Unfortunately, these ions cannot be measured by emission spectroscopy. An attempt was made to measure the density of N₂⁺ X ²Σ_g⁺ in ambient air by diode laser absorption, but

there was no signal. It might be quenched by O₂ and H₂O in air. In order to validate the assumption that a transient potential is responsible for soft ionisation in the ambient surrounding, a noble gas will be used as a substitute for ambient air. A detailed investigation will be carried out in the next chapter.

4.2.6 Plasma Development During the Negative Half Cycle

The negative half cycle starts after 25 μ s. In the following 25 μ s will always be subtracted from the real time when the spectra were recorded. The time of 80 ns in the negative half cycle inserted into the Figure corresponds to 25 μ s + 80 ns in the full discharge cycle. The propagation of the excitation and ionisation during the negative half cycle is clearly different from the positive half cycle. One of the most obvious differences is the emission shapes of reactive species. The two-dimensional colour plots and position dependent plots of He 706 nm and N₂⁺ 391 nm measured in a He-F μ TP during the negative half cycle are shown in Figure 4.17 a and b.

Compared to the signal obtained in the positive half cycle, the shapes of He 706 nm show more than one peak and have a six times broader p-FWHM than in the positive half cycle. At least two peaks are observed at 80 ns and 90 ns, along with three peaks between 100 ns and 140 ns. This indicates that the decay from He^{**} to He^{*} takes place at two or three different positions simultaneously.

Owing to the higher electron density resulting from secondary electron emission in the negative half cycle, it is suspected that, in addition to the excitation of He atoms, ionisation of He atoms also takes place. The peak attributed to He⁺ propagates towards the end of capillary, following the He^{**} peak, which is noticeable between 100 ns and 140 ns. As a result, the shapes of He 706 nm in the negative half cycle are wider than observed in the positive half cycle. Returning to the time at 90 ns, the peaks attributed to He⁺ and He^{**} overlap. This leads to a higher emission intensity of He 706 nm in the negative half cycle compared to that observed in the positive half cycle. In addition, as a result of the recombination of He⁺, one peak is always measured in the vicinity of the electrode.

The emission intensity of N₂⁺ 391 nm decreases drastically along the capillary in the negative cycle. In contrast to the propagation behaviour during the positive half cycle, where the peak of N₂⁺ 391 nm is propagating forward along the capillary to the outlet of the capillary, the highest emission intensity of N₂⁺ 391 nm during the negative half cycle remains localised in the vicinity of the electrode at all times. The bipolar voltage is applied

4.2 Spectroscopic Characterisation of the F μ TP

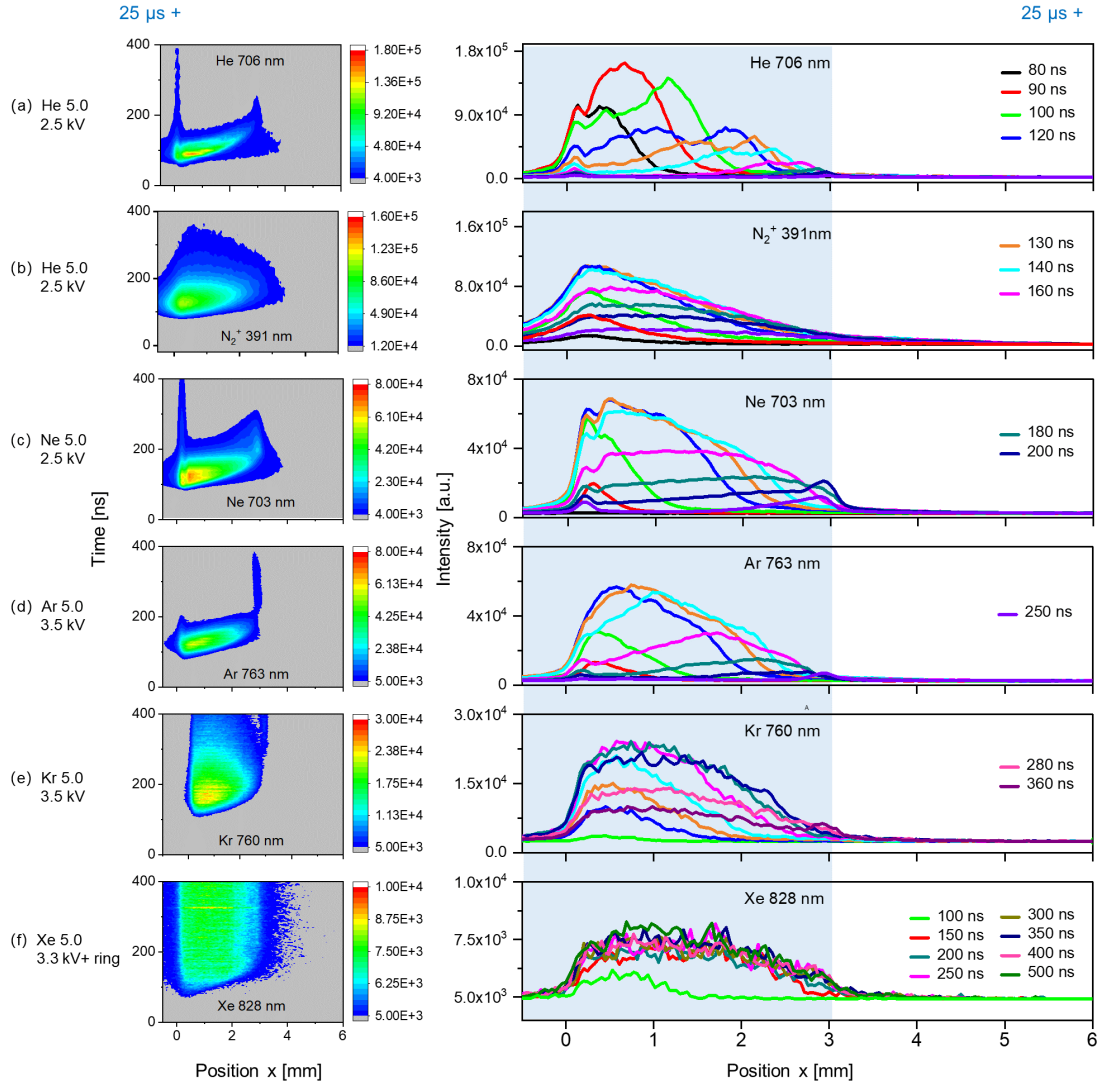


Figure 4.17: Spatial and temporal development of various noble gases driven plasmas during the negative half cycle. Two-dimensional colour plot in time and position and the related position dependent plots at different instants of time for *He* 706 nm, N_2^+ 391 nm, *Ne* 703 nm, *Ar* 763 nm, *Kr* 760 nm and *Xe* 828 nm. (a) *He* 706 nm and (b) N_2^+ 391 nm measured in a *He*-F μ TP at 2.5 kV, (c) *Ne* 703 nm measured in a *Ne*-F μ TP at 2.5 kV (d) *Ar* 763 nm measured in an *Ar*-F μ TP at 3.5 kV, (e) *Kr* 760 nm measured in a *Kr*-F μ TP at 3.5 kV, (f) *Xe* 828 nm measured in a *Xe*-F μ TP at 3.3 kV with a grounded ring. The flow rate of the discharge gas is 50 sccm.

in this chapter as shown in Figure B.1 of the Appendix. In this manner, the metal electrode is applied with a negative voltage during the negative half cycle. This negative electrode attracts positive ions, resulting in less positive ions reaching the outlet of the capillary.

The temporal-spatial emission plots and the position dependent plots of *Ne* 703 nm, *Ar* 763 nm, *Kr* 760 nm and *Xe* 828 nm measured in a *Ne*-, *Ar*-, *Kr*- and *Xe*-F μ TP are shown in Figure 4.17 c, d, e and f. The shapes are quite different from those measured in the positive

Chapter 4 Discharge Mechanisms of the F μ TP

half cycle. As explained in the positive half cycle, noble gases ions are generated and guide the excitation and ionisation propagation along the capillary, especially in an Ar-, Kr- and Xe-F μ TP. Both noble gas ions and excited states contribute to the shape of respective wavelengths.

Similar to the emission profiles of He 706 nm, a broadening of the emission shape is observed as the contribution of noble gases ions to the corresponding emission wavelengths increases. These noble gas ions are attracted by the negative electrode and accumulate in the vicinity of the electrode, forming a potential. This potential facilitates the continued progression of excitation and ionisation.

The attraction of the negative electrode to the positive ions in the negative half cycle results in a weak positive potential in the vicinity of the capillary outlet, and thereby creating a weak electric field. This field is not sufficient for accelerating electrons to the energies necessary for exciting and ionising molecules or atoms beyond the capillary. As a result, neither excited species nor ions are generated in the ambient air. This is consistent with the observed phenomena that both the ions and the excited species are all confined inside the capillary. Therefore, even if a higher energy dissipation takes place in the negative half cycle, each reaction occurs inside the capillary. It is not involved in the protonation processes outside the capillary.

4.3 Conclusion

In this chapter, the ionisation efficiencies of He-, Ne-, Ar-, Kr- and Xe-F μ TP as soft ionisation sources were investigated by MS measurements. Furthermore, the excitation and ionisation propagation of these plasmas within the capillary, as well as their transitions into ambient air, were systematically elucidated using temporally and spatially resolved emission spectroscopy.

The emission shapes of He 706 nm and Ne 703 nm are almost symmetric at low applied voltage. In contrast, the shapes of Ar 763 nm, Kr 760 nm and Xe 828 nm show a significant asymmetry. Two discharge categories were divided inside the discharge capillary. In a He- and Ne-F μ TP operated at low applied voltage, N₂⁺ are the main ions to facilitate the propagation of the excitation and ionisation along the discharge capillary. N₂⁺ are not involved in an Ar-, Kr- and Xe-F μ TP, where noble gas ions are generated and play a role

4.3 Conclusion

in the propagation of the excitation and ionisation. With an increase in the applied voltage, noble gas ions can also be generated in a *He*- and *Ne*-F μ TP.

The ionisation wave of detectable ions stops in the vicinity of the capillary outlet, and the excitation continues propagating in the ambient surrounding in the positive half cycle. A reasonable explanation for that is that the charged species are produced in ambient air. It was suggested that the components of air such as nitrogen, oxygen, water might be ionised. The ions generated in the process serve a dual purpose. They facilitate the continued propagation of the excitation and also act as the primary ions in the formation of protonated water clusters. These ions cannot be tracked by optical emission spectroscopy because of missing or unknown emission wavelengths.

According to the finding that the ionisation efficiency of a *Xe*-F μ TP is comparable with other noble gas driven plasmas, it was concluded that Penning ionisation, charge transfer and photoionisation between the plasmas and ambient air are not the main ionisation processes. All ionisation waves of the measurable ions stop in the vicinity of the capillary outlet, where a transient potential could be created. It was assumed that this potential is responsible for the possible ionisation of the air components and thus the protonation in the positive half cycle. It is independent of the type of discharge gas but on the amount of the ions. In contrast to the case of positive half cycle, positive ions are attracted by the negative electrode, leading to fewer ions being located in the vicinity of the capillary outlet. No ions or excited species are observed outside the capillary. The potential is too low to function on protonation in the ambient surrounding in the negative half cycle.

However, such potential cannot be measured directly without disturbing the plasma itself. Further careful considerations are needed to test this assumption. Detailed investigations in these directions will be carried out in the next chapter by designing different experimental arrangements. A diagnosis gas with known emission wavelengths will be applied to replace the ambient air.

Excitation and Ionisation of a Diagnosis Gas ^{P2, P6}

So far, investigations on the propagation of the excitation and ionisation within and outside the capillary have been carried out. It has been demonstrated that the propagation of ionisation is crucial for the propagation of excitation.

Within the discharge capillary, N_2^+ in a *He*- and *Ne*-F μ TP operated at low applied voltage or noble gas ions in an *Ar*-, *Kr*- and *Xe*- F μ TP support the excitation and ionisation propagation forward. The ionisation waves of these ions stop in the vicinity of the capillary outlet. It was supposed that a transient potential in the vicinity of the capillary outlet and

P2: Parts of this chapter are based on the previously published article: Soft ionisation mechanisms in flexible μ -tube plasma—from F μ TP to closed μ -tube plasma by Speicher L, Song H, Ahlmann N, Foest D, Höving S, Brandt S, Niu G, Franzke J, **Tian C**; it was first published in *Analytical and Bioanalytical Chemistry*, 2024 as an open access article and is licensed under Creative Commons Attribution 4.0 International License (<http://creativecommons.org/licenses/by/4.0/>).

P6: Substantial parts of this chapter are based on the previously published article: Excitation and ionisation of a diagnosis gas in front of the flexible μ tube plasma and in a diagnosis tube by Song H, **Tian C**, Speicher L, Ahlmann N, Foest D, Höving S, Brandt S, Niu G, Franzke J; it was first published in *Spectrochimica Acta Part B: Atomic Spectroscopy*, 2024 as an open access article and is licensed under Creative Commons Attribution 4.0 International License (<http://creativecommons.org/licenses/by/4.0/>).

Chapter 5 Excitation and Ionisation of a Diagnosis Gas

therewith an electric field is created by these ions. This electric field region is an excellent chemical reaction place producing reactive species such as excited states O^* , OH^* , N_2^* , excited noble gas species, and ionised species for example N_2^+ , O_2^+ , H_3O^+ , etc. when the corresponding atoms or molecules are present [102]. However, these ions cannot be measured directly by emission as the transitions of these species are unknown or missing in the wavelength range of the spectrometers used. When attempting to measure the density of the $N_2^+ X^2\Sigma_g^+$ state by diode laser absorption, no signal could be measured. This may be quenched by O_2 and H_2O in air. It was also not possible to measure such potential directly, as there is only one electrode in the F μ TP and conductors in the vicinity of the plasma can affect the plasma itself.

In this chapter, a diagnosis gas with known emission wavelengths will be introduced to substitute the surrounding air to validate the assumption. In order to make the measurements convincing, *He* will always be used as the diagnosis gas. The energy level of the excited state (*He***) is higher than that of each state of the other noble gases. For that, different experimental setups will be arranged. The last part of this chapter presents a new ionisation source resulting from the findings of this thesis. It is a plasma-based ionisation source without gas consumption, and the patent has been authorized [108]. The parts of data shown in this chapter have been published in 2024 [92,109].

5.1 Experimental Arrangement

Figure 5.1 shows the initial experimental arrangement used in this chapter. A diagnosis tube without any electrode is introduced to deliver a diagnosis gas. The inner and outer diameters of the diagnosis tube are 1.0 mm and 1.2 mm, respectively. The length of this tube is 30 mm.

For the ignition of plasma in the discharge capillary, a bipolar square wave generator is applied. Various noble gases are introduced as discharge gases at a flow rate of 50 sccm. Detailed voltages are listed in Table 5.1. For a Xe-F μ TP, an additional metal ring is installed on the coaxial side of the capillary, as mentioned in the previous chapter and shown in Figure B.2 of the Appendix. *He* is used as the diagnosis gas. Different flow rates are used, which will be given in the respective sections.

Similar to the characterisation of the plasmas along the discharge capillary, the USB 4000 spectrometer with an optical fibre and the Kymera Spectrograph with an ICCD camera are

5.1 Experimental Arrangement

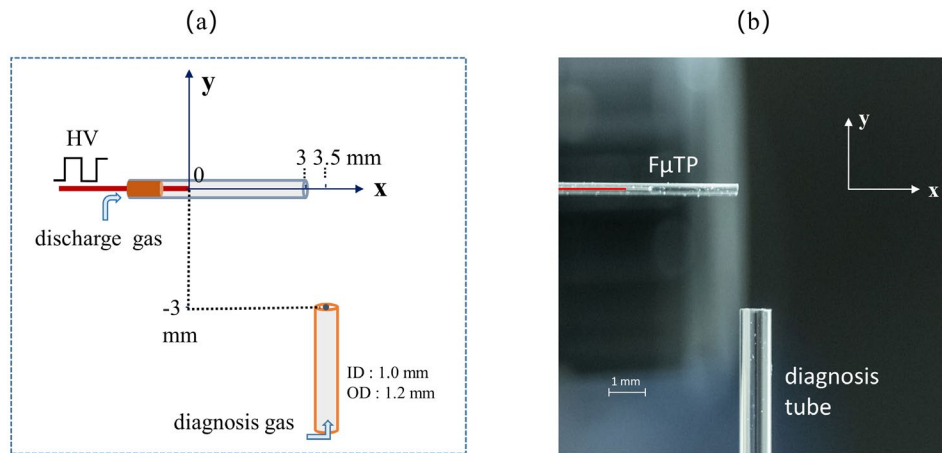


Figure 5.1: The initial experimental setup for the introduction of the diagnosis gas. (a) Schematic of the experimental setup. Reprinted with the permission from [109], Copyright 2024 Elsevier. (b) Photograph. The discharge gas flow and the diagnosis gas flow contact to each other at the coordinate of (3.5 mm, 0 mm).

used to investigate the generation and propagation of the plasma along the diagnosis tube. In this chapter, the USB 4000 spectrometer is used to capture not only reactive species of the plasmas along the discharge capillary, but also the plasmas along the diagnosis tube by changing the coordinates of the optical fibre. For the imaging system, an external signal generator is still used to synchronise the ICCD camera and the power generator applied on F μ TP. The object distance and image distance are around 400 mm and 100 mm, respectively. A diffraction grating comprising 1200 grooves per millimetre is selected.

Table 5.1: Experiment conditions for different plasma types

Discharge Plasma	Diagnosis gas	Applied voltage (kV)	Gate width (ns)	Step width (ns)	Gain (a.u)
He-F μ TP	He	2.5	10	10	250
Ne-F μ TP	He	2.5	10	10	250
Ar-F μ TP	He	3.0	10	10	250
Kr-F μ TP	He	3.1	10	10	250
Xe-F μ TP	He	3.3 +ring	-	-	-

“-” do not measure

The relative position of the lens, the entrance slit of the Kymera Spectrograph and the diagnosis tube changes, which will be described in the corresponding sections. The

entrance slit of the Kymera Spectrograph is set to 300 μm , otherwise, a specific description will be given.

5.2 Diagnosis Plasma Ignition in Front of the F μ TP

When the F μ TP is applied as a soft ionisation source, it is usually located in front of the mass spectrometer inlet. Analytes are delivered between the ionisation source and the mass spectrometer inlet to be ionised. In the following measurements, a diagnosis gas is transported to the place where the analytes are usually located to gain a better understanding of the soft ionisation mechanism. In this case, the discharge gas flowing through the F μ TP capillary and the diagnosis gas delivered by the diagnosis tube are in contact with each other.

Figure 5.2 shows the temporal and spatial evolution of the whole emission from the discharge capillary, along with the subsequent ignition and propagation along the diagnosis tube (y axis) at selected instants of time during the positive (Figure 5.2 a) and negative half cycles (Figure 5.2 b). In the following descriptions, to distinguish between these two plasmas, the plasma generated along the discharge capillary is referred as to the discharge plasma and the plasma along the diagnosis tube is termed the diagnosis plasma.

In this case, both the discharge and diagnosis gas is *He*. The flow rate is 50 sccm and 500 sccm for discharge gas and diagnosis gas, respectively. To acquire the data along the discharge capillary and the diagnosis tube to understand how the diagnosis plasma is ignited and develops, the entrance slit of the Kymera Spectrograph was parallel to the discharge capillary and set at a maximum of 2500 μm . The white background region in the subgraphs is the area outside the detection coverage of the entrance slit, thus only a portion of the diagnosis signal was recorded.

In the positive half cycle, the discharge plasma propagates outside the capillary, and then the diagnosis gas is ignited. The diagnosis plasma propagates along the diagnosis tube in two directions, both with (+ y) and against (- y) the diagnosis flow, as marked by magenta arrows. The emission signal propagating with the direction of the diagnosis flow disappears earlier than the signal developing against the diagnosis gas flow. This result arises from the lower concentration of the diagnosis gas atoms with the diagnosis gas flow direction in comparison to their concentration against the diagnosis gas flow.

5.2 Diagnosis Plasma Ignition in Front of the $F\mu TP$

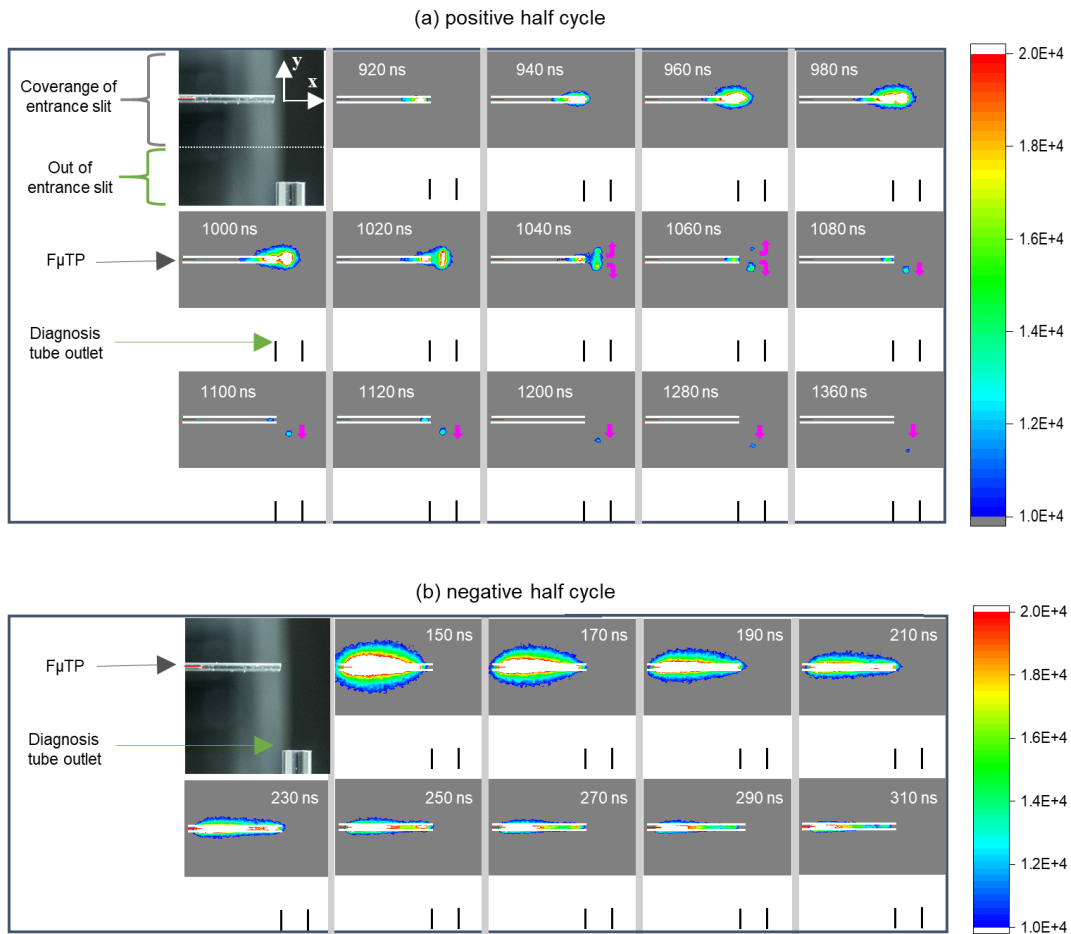


Figure 5.2: Emission contour plots of the whole emission at different instants of time for a He - $F\mu TP$ with He as diagnosis gas in the positive (a) and negative (b) half cycles. The applied voltage is 2.5 kV. The flow rate of the discharge gas is 50 sccm and 500 sccm for the diagnosis gas. The magenta arrows show the plasma propagation along the diagnosis tube. Adapted with the permission from [109], Copyright 2024 Elsevier.

In the negative half cycle, the discharge plasma propagates along the discharge capillary and extinguishes over time when it reaches the outlet. No propagation of the whole emission along the diagnosis tube is observed. In this sense, it can be concluded that the protonation process only occurs in the positive half cycle when the $F\mu TP$ ionisation source is located in front of the mass spectrometer inlet.

When a $F\mu TP$ is operated with noble gas such as Ar , Kr and Xe instead of He , the emission of the diagnosis plasma along the diagnosis tube is more pronounced, even when He is used as the diagnosis gas. In these cases, the diagnosis plasma propagates not only to the diagnosis tube nozzle but also enters the diagnosis tube. The results are shown in Figure 5.3 a. This phenomenon occurs only when the applied voltage is high. The length of the diagnosis plasma depends on the applied voltage.

Chapter 5 Excitation and Ionisation of a Diagnosis Gas

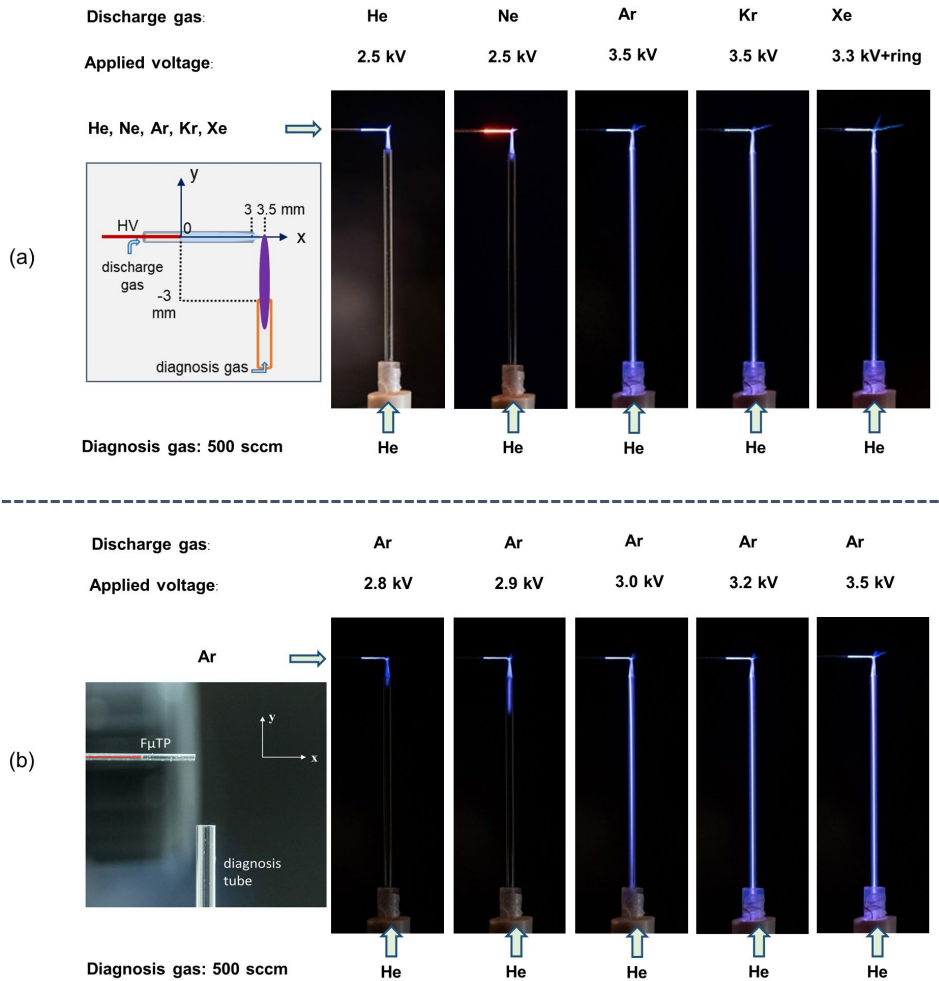


Figure 5.3: The ignition of *He* as diagnosis gas by different noble gas driven plasmas in front of the discharge capillary outlet. (a) Photographs of the plasma emission with the discharge gas *He*, *Ne*, *Ar*, *Kr* and *Xe*. Adapted with the permission from [93], Copyright 2024 Springer. (b) Photographs of the plasma emission with the discharge gas *Ar* under different operation voltages. The flow rate of the discharge gas is 50 sccm and 500 sccm for the diagnosis gas. Adapted with the permission from [109], Copyright 2024 Elsevier.

In this instance, taking an *Ar*-F μ TP as an example, when the applied voltage is 2.8 kV, the diagnosis plasma only propagates to the diagnosis tube nozzle. When the applied voltage is increased, the emission along the diagnosis tube gets longer as shown in Figure 5.3 b. This phenomenon also applies to a *He*-F μ TP and *Ne*-F μ TP. However, the emission behind the electrode tip can also be observed at higher voltages in case of *He*-F μ TP and *Ne*-F μ TP. This is related to the lower breakthrough voltages of *He* and *Ne* compared to those of *Ar*, *Kr* and *Xe*. This process steals energy from the system and, consequently, that is no longer available for the system. Therefore, when *He* and *Ne* are used as discharge gases, a voltage of 2.5 kV is applied.

5.2 Diagnosis Plasma Ignition in Front of the F_uTP

In order to determine how the diagnosis plasma is ignited, the optical emission spectra of the discharge plasma and the diagnosis plasma were measured first using an USB 4000 spectrometer with an optical fibre. *Ar* is introduced as the discharge gas, and *He* is used as the diagnosis gas. The experimental setup and the spectra at multiple positions along both the discharge capillary and the diagnosis tube are shown in Figure 5.4. The corresponding coordinates of the optical fibre located are inserted into the middle of the figure.

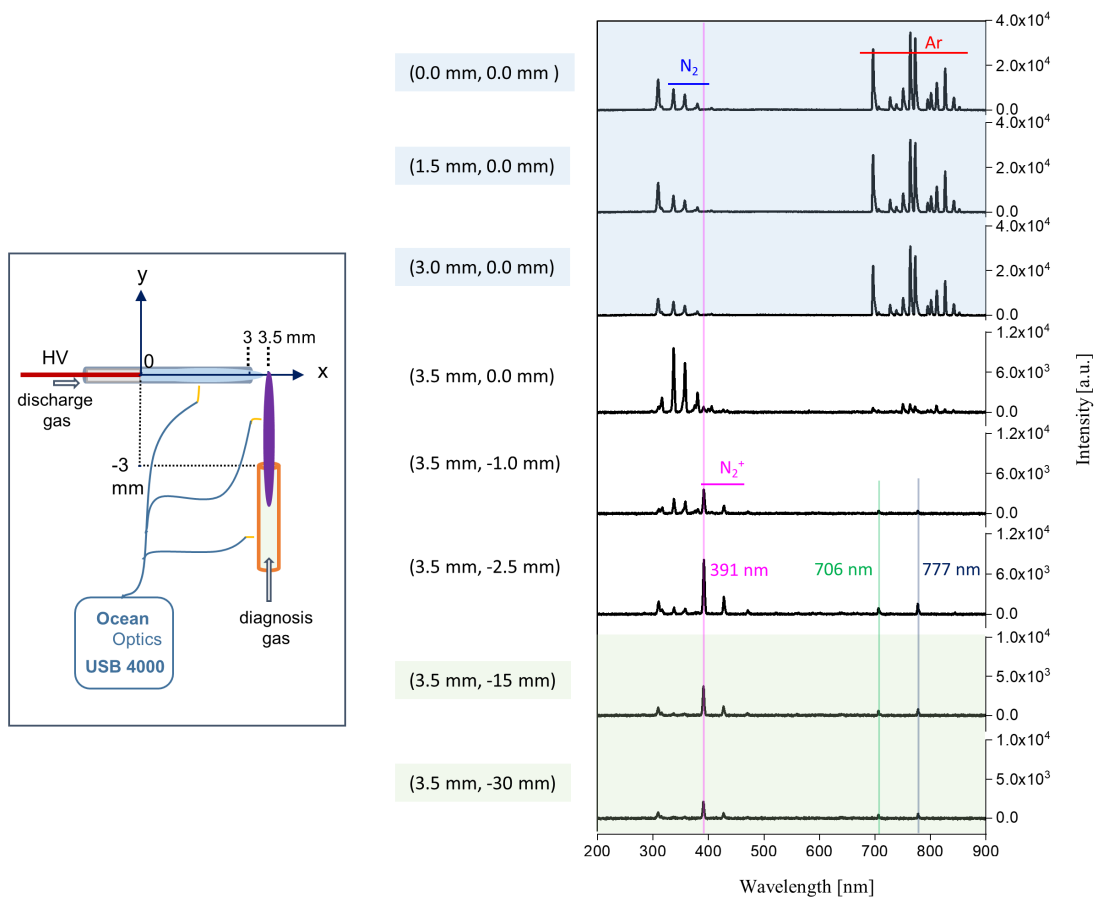


Figure 5.4: The integrated emission spectra of the discharge plasma and the diagnosis plasma at different positions obtained by an USB 4000 spectrometer. The respective positions of optical fiber are indicated by the coordinates shown in the middle parts of the diagrams. *Ar* with a flow rate of 50 sccm is used as discharge gas and *He* with a flow rate of 500 sccm is used as diagnosis gas. The voltage applied to the electrode is 3.0 kV. The integration time is 10 ms. The wavelengths at 391 nm, 706 nm and 777 nm are marked by colourful lines. Adapted with the permission from [109], Copyright 2024 Elsevier.

The spectra collected along the discharge capillary (light blue background area) show the excited OH emission, the excited N₂ (SPS, N₂ C ³Π_u → N₂ B ³Π_g) and the characteristic *Ar* lines as marked by the red horizontal line. These spectra match the spectra obtained in the

Chapter 5 Excitation and Ionisation of a Diagnosis Gas

Ar-F μ TP explained in the last chapter (see Figure 4.4). The emission intensities of *Ar* lines are the highest. As the position of the optical fibre is shifted from the end of the discharge capillary (3.0 mm, 0.0 mm) to the interaction point (3.5 mm, 0.0 mm) of two gases, the emission intensities of these *Ar* lines decrease and those of SPS increase. This result is caused by the decrease in the density of *Ar* atoms and the increase in the concentration of air components.

In the region between the crossing point (3.5 mm, 0.0 mm) and the diagnosis tube nozzle (3.5 mm, 3.0 mm) (white background area), the ionised N_2 (FNS, $N_2^+ B \ ^2\Sigma_u^+ \rightarrow N_2^+ X \ ^2\Sigma_g^+$) is observed. This region is referred to as the “open area” in the following descriptions. Moreover, the closer the distance to the diagnosis tube nozzle, the higher the emission intensity of FNS. The wavelengths of *He* 706 nm and O 777 nm can also be observed.

Keep shifting the optical fibre along the diagnosis tube away from the diagnosis tube nozzle (light green background area), the types of emission lines do not change compared to those measured in the open area. Only the emission intensities of them decrease. These spectra match the emission spectra measured in a *He-F μ TP* (see Figure 4.4). This means that the *He* is indeed ignited by an *Ar* plasma.

Interestingly, the energy levels of Ar^M (11.5 eV and 11.7 eV) and even Ar^+ (15.8 eV) are significantly lower than that of the lowest excited of the *He* state (19.6 eV). As a result, Penning ionisation and charge transfer between these species and *He* atoms are not feasible. Nevertheless, *He* atoms in the open area and inside the diagnosis tube are still excited. This suggests the presence of alternative mechanisms responsible for the excitation of *He* atoms.

For that, temporally and spatially resolved emission measurements of diagnosis plasma were performed. *He*, *Ne*, *Ar* and *Kr* are introduced as a discharge gas to ignite a diagnosis plasma. In the following sections, measurements focus on the generation and propagation of the diagnosis plasma. The Kymera Spectrograph is rearranged to make its entrance slit parallel to the vertical axis of the diagnosis tube. The slit is set to 300 μ m. As the diagnosis gas is excited by *F μ TP* only during the positive half cycle, the following measurements will focus only on the propagation of excitation and ionisation during the positive half cycle.

Figure 5.5 shows the propagation of the diagnosis plasma ignited by *He-*, *Ne-*, *Ar-* and *Kr-F μ TP*, respectively. The top two graphs represent the two-dimensional colour plots of *He* 706 nm and N_2^+ 391 nm measured in each case. The abscissa shows the development along the diagnosis tube and the ordinate shows the time. The lower graphs show the

5.2 Diagnosis Plasma Ignition in Front of the F μ TP

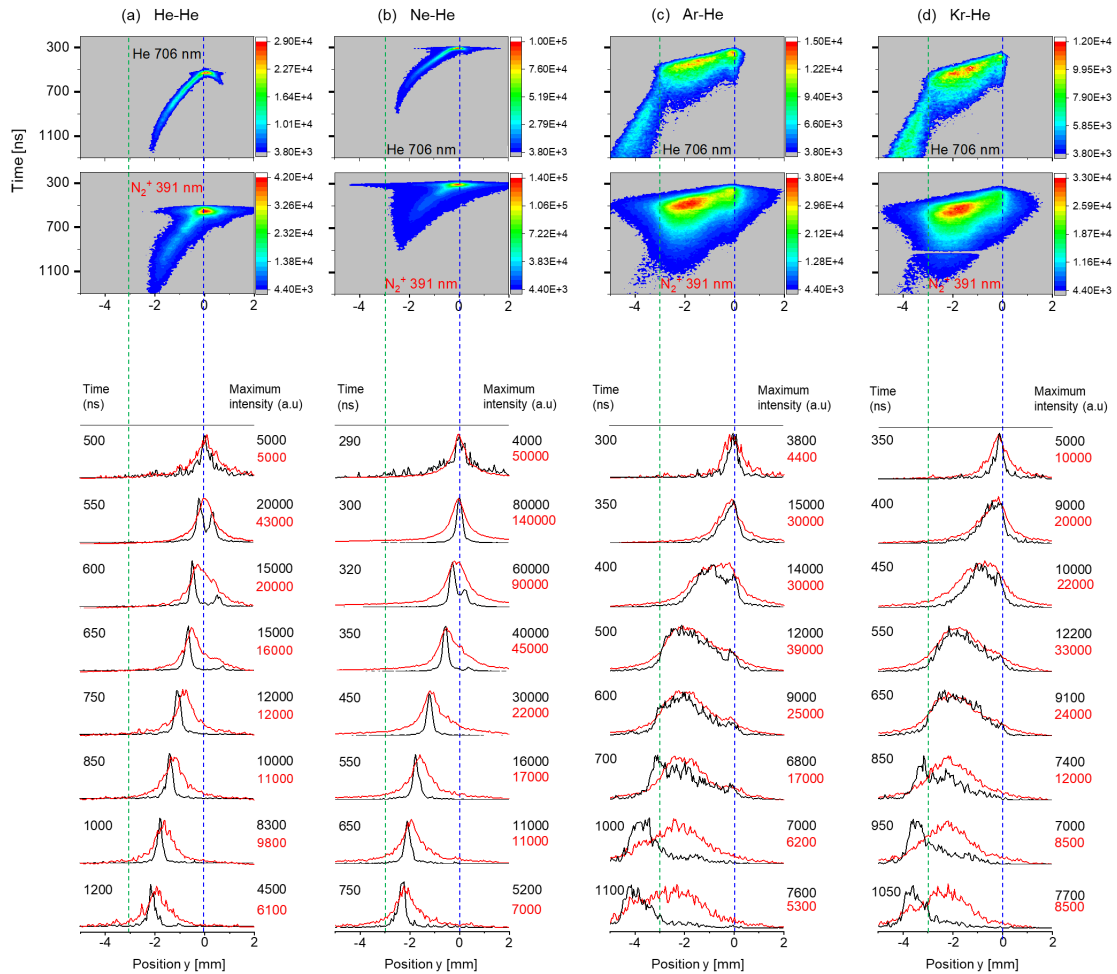


Figure 5.5: The ignition and propagation of diagnosis plasmas in front of the F μ TP. Two-dimensional colour plots and position dependent plots at different instants of time for the He 706 nm (black line) and N $_2^+$ 391 nm (red line) ignited by different plasmas. (a) He-F μ TP at 2.5 kV, (b) Ne-F μ TP at 2.5 kV, (c) Ar-F μ TP at 3.0 kV, (d) Kr-F μ TP at 3.1 kV. The discharge and diagnosis gas flow rates for all cases are 50 sccm and 500 sccm, respectively. The blue dashed line represents the crossing point of the axis of diagnosis tube and discharge capillary along y axis ($y = 0$ mm). The green dashed line represents the diagnosis tube nozzle ($y = 3$ mm). Adapted with the permission from [109], Copyright 2024 Elsevier.

position dependent emission intensities of He 706 nm (black line) and N $_2^+$ 391 nm (red line) at different instants of time. The scale of emission intensity in each subgraph is individually normalised to its maximum value, with the maximum measured value indicated in the upper right corner of each subgraph for reference. The corresponding instant of time is inserted on the left side of each subplot. Note that the position $y = 0$ mm marked by the blue dashed line through the graphs represents the crossing point of the axis of the diagnosis capillary and the discharge tube, while the position $y = -3$ mm marked by the green dashed line represents the diagnosis tube nozzle.

Chapter 5 Excitation and Ionisation of a Diagnosis Gas

Starting at the graphs of *He* 706 nm as shown in Figure 5.5 a, the emission develops to both directions from the point of $y = 0$ mm, positive y ($y > 0$ mm) with the direction of diagnosis gas flow as well as negative y ($y < 0$ mm) against the direction of the diagnosis gas flow. The emission intensity of *He* 706 nm in positive y decreases to zero after around 200 ns (from 550 ns to 750 ns). The propagation length is greater than 0.5 mm but less than 1 mm.

In the case of *Ne-He* (Figure 5.5 b), the propagation length of *He* 706 nm in positive y -side is less than 0.5 mm, which is shorter than in the case of *He-He*. In the case of *Ar-He* and *Kr-He* (Figures 5.5 c and d), the propagation of *He* 706 nm in the positive y -side is not observed. Instead, it remains confined to the position $y = 0$ mm for a while. This might be mainly related to the density of *He* atoms in the positive y -direction.

With the same mass flow through the discharge capillary, the same number of atoms passes through the capillary for each of the noble gases. Typically, with the same particle density of the discharge gas atoms, the momentum of the discharge particles increases with increasing mass of the discharge gas atoms. The discharge gas stream acts as a kind of curtain perpendicular to the axis of the diagnosis gas flow, whose permeability decreases with increasing momentum. Therefore, the greater the mass of the discharge gas atoms, the fewer diagnosis gas atoms can pass through this curtain to the other side of the discharge gas stream, namely the positive y -side. This also leads to a higher accumulation of diagnosis gas atoms on the negative y -side.

In case of *He-He* and *Ne-He*, the propagation of *He* 706 nm and N_2^+ 391 nm occurs mainly in the open area. They do not propagate into the diagnosis tube. A close examination of the two-dimensional colour plots of *He* 706 nm, it can be seen that the temporal width is narrow for all positions. In addition, the p-FWHM of *He* 706 nm as shown in position dependent graphs is also narrow (about 500 μm).

Furthermore, the shapes of *He* 706 nm are almost symmetric, suggesting that almost no He^+ or only a small amount of He^+ are produced. Consequently, the effect of He^+ on the shape of *He* 706 nm is negligible. Based on the understanding gained in the case of *He-FuTP* that when the N_2^+ B $^2\Sigma_u^+$ is mainly produced by Penning ionisation, the maximum of the *He* 706 nm signal locates at the largest derivative of the N_2^+ 391 nm signal [91]. The maximum of the *He* 706 nm signal along the diagnosis tube in these two cases is only slightly in front of the maximum of the N_2^+ 391 nm signal. This suggests that there is another origin for N_2^+ B $^2\Sigma_u^+$ besides Penning ionisation.

5.2 Diagnosis Plasma Ignition in Front of the F μ TP

Although a large number of *He* atoms accumulate on the negative *y*-side, the concentration of N_2 molecules in the open area is higher than that of N_2 in the discharge capillary with *He* 5.0 (3 ppm N_2). This difference arises from the diffusion of air into the open area. As a result, a certain degree of electron impact also contributes to the generation of $N_2^+ B^2\Sigma_u^+$ in this area. It is suspected that these N_2^+ form a temporal and spatial dependent potential, which in turn is responsible for the next round of excitation and ionisation. After 700 ns and 460 ns in case of *He-He* and *Ne-He* respectively, the excitation and ionisation propagation stop. In other words, at that instant of time, the transient potential is not sufficient to sustain the next excitation and ionisation any longer.

In case of *Ar-He* and *Kr-He*, not only the temporal width for all positions but also the p-FWHM of *He* 706 nm (about 2 mm) are wider than that of *He* 706 nm measured in the case of *He-He* and *Ne-He*. Focusing on the p-FWHM of $N_2^+ 391$ nm, which is also wider in the case of *Ar* and *Kr* driven plasmas than those of *He* or *Ne* driven plasma. As explained above, because of the effects of the curtain formed by the discharge gas stream, there is a higher accumulation of the diagnosis gas in the negative *y*-side in the case of *Ar* and *Kr* driven plasmas compared to *He* and *Ne* driven plasmas. As a result, more *He* atoms as well as N_2 molecules are excited and ionised.

Taking a closer look at the position dependent subgraphs from 300 ns to 600 ns in case of the *Ar* driven plasma and from 350 ns to 650 ns in case of the *Kr* driven plasma, the distributions of *He* 706 nm signal and $N_2^+ 391$ nm signal are almost overlapping. Coincidentally, during these instants of time, *He* 706 and $N_2^+ 391$ nm propagate within the open area. This suggests that the contribution of direct electron ionisation to the generation of $N_2^+ B^2\Sigma_u^+$ species becomes larger compared to the cases of *He* and *Ne* driven plasmas.

Interestingly, a spatial offset of the maxima of both *He* 706 nm and $N_2^+ 391$ nm emission towards the nozzle of the diagnosis tube is observed in the case of *Kr-He*. These maxima are located around $y = 2$ mm (550 ns). It is expected that the same phenomenon should be observed in the case of the *Ar-He*. However, the maximum of $N_2^+ 391$ nm is observed at $y = 2$ mm (500 ns) and the maximum of 706 nm is at the position of $y = 0$ mm. It is worth noting that here the position of $y = 0$ mm refers to the interaction point (3.5 mm, 0.0 mm) of two gases.

As can be seen in Figure 5.3, the emission signals from the *Ar* lines are still detectable at this coordinate. The *Ar* plasma also has an emission line at 706 nm. As a result, *Ar* 706 nm emitted from the discharge plasma at $y = 0$ mm contributes to the overall intensity of the wavelength at 706 nm. Even if the emission intensity of *Ar* 706 nm is low at this coordinate,

Chapter 5 Excitation and Ionisation of a Diagnosis Gas

this compensation results in the maximum intensity of 706 nm remaining at $y = 0$ mm. The *He* 706 nm and N_2^+ 391 nm signals propagate inside the diagnosis tube in the case of the *Ar-He* and *Kr-He*, which is also valid for the case of the plasma driven by *Xe* (see Figure 5.3 a). The propagation of *He* 706 nm reaches the diagnosis tube nozzle at 700 ns and 850 ns in *Ar-He* and *Kr-He*, respectively. It is noticeable that the p-FWHM of *He* 706 nm within the diagnosis tube becomes narrow compared to that in the open area. Such results hint that *He* atoms not only are excited but also ionised at the same time in the open area. These species are located at different positions, leading to a broadening of the emission peak of *He* 706 nm. He^+ and N_2^+ reach the diagnosis tube nozzle and polarise it.

So far, it has been demonstrated that the energy of the metastable states of noble gases (e.g. Ne^M , Ar^M , Kr^M , Xe^M) and even their ionic states (e.g. Ar^+ , Kr^+ , Xe^+) is not sufficient to generate the lowest excited state of *He* (19.6 eV). Nevertheless, the diagnosis plasma is still successfully ignited by a *Ne-*, *Ar-*, *Kr-* and *Xe-F μ TP*. These results cannot be attributed to the Penning ionisation, charge transfer, or excitation transfer between these plasmas and diagnosis gases. Usually, the excited *He* is produced by collision of *He* atoms with energetic electrons accelerated in an electric field. Once the electric field is sufficient, the electrons can be accelerated to the energy level required to excite *He* atoms.

Moreover, it has been demonstrated that the ionisation wave of N_2^+ and noble gas ions stop in the vicinity of the capillary outlet. As a result, a temporally and spatially dependent potential can be created by these ions and thereby an electric field. When such a potential is sufficient, the diagnosis gas located in front of the discharge capillary is ignited. Therefore, the excitation of *He* atoms does not depend on the type of discharge gas used but on the strength of potential formed by these plasmas. When the diagnosis gas *He* is replaced by ambient air, it is reasonable to expect that the air components of N_2 , O_2 and H_2O can be ionised, generating N_2^+ , O_2^+ and H_3O^+ , etc. even if their ionisation levels are higher than that of the noble gas used for the discharge.

To further confirm the role of a transient potential on the excitation and ionisation of the diagnosis gas, two further experiments will be carried out by changing the experimental arrangements. In these modified cases, a glass wall is present between the discharge plasma and the volume to be ionised, where the discharge plasma will no longer be in contact with the diagnosis gas. They can be handled as two individual gas flows without any mixture. In one case, the diagnosis tube is moved so far in the positive y -axis direction that the glass wall of the diagnosis tube is located between the diagnosis gas stream and the discharge gas stream. In the other case, the diagnosis tube is shifted in the negative x -

5.3 Diagnosis Plasma Ignition Beyond a Glass Wall

axis, so that the glass wall of the discharge capillary is positioned between the diagnosis gas stream and the discharge gas stream. It is worth noting that the silica glass wall of these two capillaries does not transmit radiation below 300 nm.

The energy levels of *Ar*, *Kr*, and *Xe* are all lower than those of the *He^M*. In addition, *Ar* costs less compared to *Kr* and *Xe*. Therefore, *Ar* is selected as the discharge gas and *He* is introduced as the diagnosis gas in the following measurements.

5.3 Diagnosis Plasma Ignition Beyond a Glass Wall

5.3.1 Beyond the Diagnosis Tube Wall

The preceding chapters have demonstrated that a fraction of the ions within the plasma temporarily adhere to the inner wall of the discharge capillary. According to the effect of the dielectric barrier of the glass, a rapidly changing potential on the outer wall induces a corresponding change in potential on the inner wall. This occurs through the polarisation of the glass, which is caused by sorting of the charged species within the dielectric layer. Consequently, ionisation is expected to occur outside of the capillary as well when the potential is sufficiently strong.

Figure 5.6 a displays the experimental arrangement of the first case where the diagnosis tube is located between two gases. A corresponding photograph where the flow rate of the diagnosis gas is 25 sccm is shown in Figure 5.6 b. Underneath are the two-dimensional colour plots showing temporal and spatial emissions of *He* 706 nm and N_2^+ 391 nm (Figures 5.6 c and d). The emission intensities of *He* 706 nm and N_2^+ 391 nm as a function of position at different instants of time along the diagnosis tube are shown in Figure 5.6 e. The corresponding time is inserted on the left side of each subgraph, and the maximum intensity of each wavelength at the corresponding moment is displayed on the right side. The crossing point of the discharge capillary and diagnosis tube axis is defined as $y = 0$ mm marked by a blue dashed line.

The first moment shown in Figure 5.6 e is at 150 ns. Up to this time, *Ar* plasma propagates in the discharge capillary up to the outer surface of the diagnosis tube. A temporal charge layer on the outer wall of the diagnosis tube is formed by the attachment of ions generated in front of the discharge capillary nozzle. Meanwhile, a temporal potential on the inner wall of the diagnosis tube is created by the polarisation effect of glass. Ignition of the diagnosis

Chapter 5 Excitation and Ionisation of a Diagnosis Gas

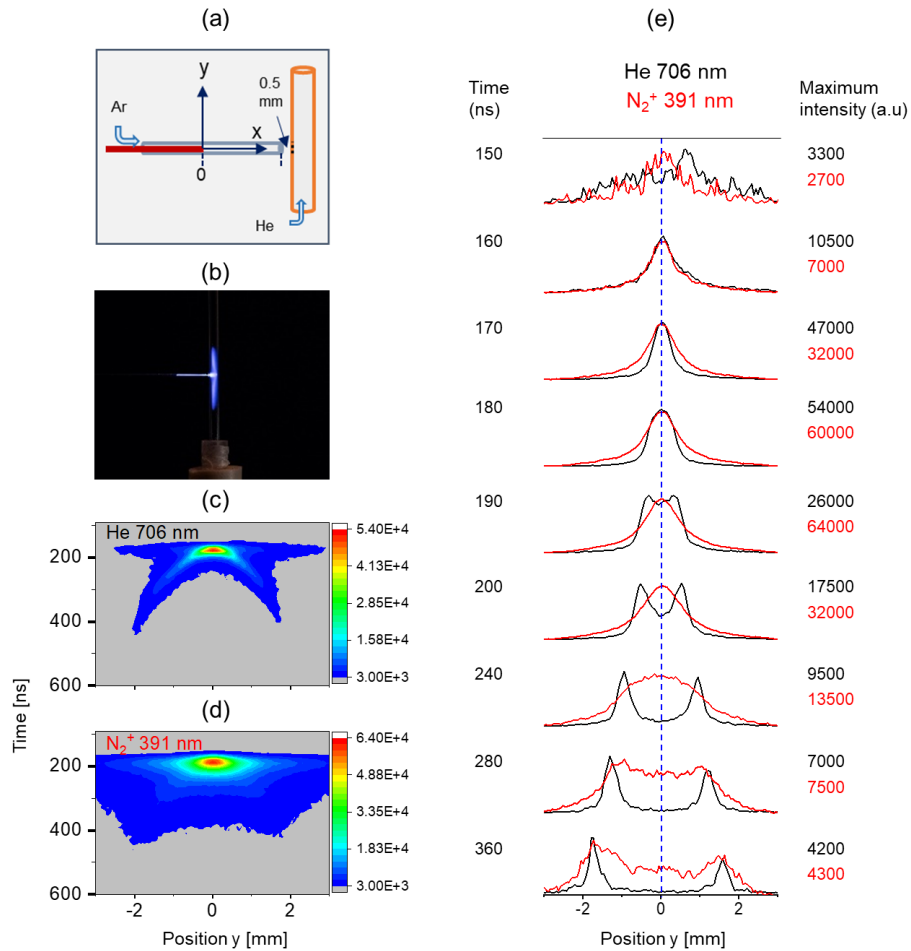


Figure 5.6: The ignition and propagation of the diagnosis plasma beyond the diagnosis tube wall. The diagnosis gas *He* with a flow rate of 25 sccm is ignited by an *Ar*-F μ TP at 3.5 kV. The flow rate of the discharge gas *Ar* is 50 sccm. Experimental arrangement (a). Photo (b). Two-dimensional colour plots in time and position for *He* 706 nm (c) and N_2^+ 391 nm (d). The position dependent plots at different instants of time for the 706 nm (black line) and N_2^+ 391 nm (red line) (e). Both the gate width and the step width are 10 ns. The gain is set 200 a.u. The blue dashed line represents the crossing point of the axis of diagnosis tube and discharge capillary along *y* axis ($y = 0$ mm). Adapted with the permission from [109], Copyright 2024 Elsevier.

gas occurs when the potential on the inner wall surpasses its breakdown threshold. As shown in the subplot at 160 ns, the *He* 706 nm signal begins to be measured within the diagnosis tube. At the same time, the N_2^+ 391 nm signal is also observed. The emission intensity of *He* 706 nm reaches the maximum at 180 ns and its peak starts separating into two signals from 190 ns. The one propagates in the positive *y* direction, and the other propagates in the negative *y* direction. The emission intensity of N_2^+ 391 nm reaches the maximum at 190 ns. The profile of N_2^+ 391 nm becomes broader until it clearly splits into two peaks at 280 ns. Subsequently, the emission of N_2^+ 391 nm propagates to both sides along the diagnosis tube. With these N_2^+ inside the diagnosis tube, a transient potential

5.3 Diagnosis Plasma Ignition Beyond a Glass Wall

could be created, which is responsible for the further excitation and ionisation of the diagnosis gas along the tube.

5.3.2 Beyond the Discharge Capillary Wall

Figure 5.7 a shows the experimental arrangement of the second case, where the glass wall of the discharge capillary separates the discharge plasma and the diagnosis gas. A photograph of diagnosis plasma with a diagnosis gas flow of 500 sccm ignited by an Ar-F μ TP is shown in Figure 5.7 b. The two-dimensional colour plots of the emission evolution of He 706 nm and N₂⁺ 391 nm inside the diagnosis tube are shown in Figures 5.7 c and d,

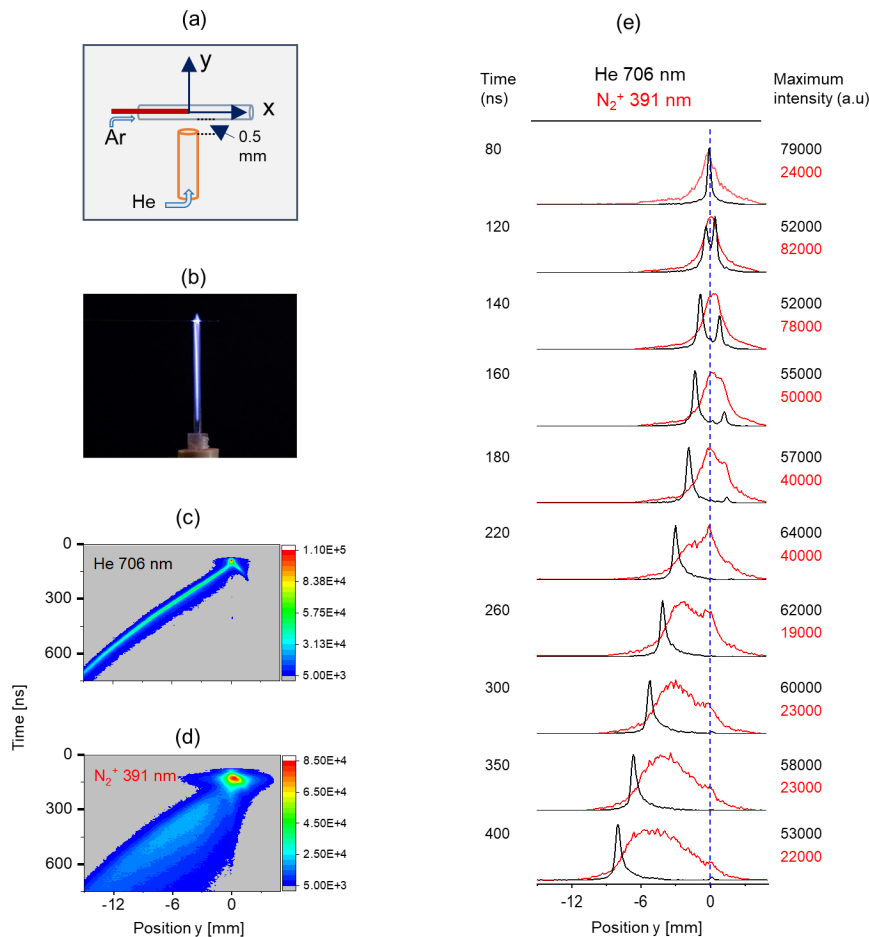


Figure 5.7: The ignition and propagation of the diagnosis plasma beyond the discharge capillary wall. The diagnosis gas He with a flow rate of 500 sccm is ignited by an Ar-F μ TP at 3.5 kV. The flow rate of the discharge gas Ar is 50 sccm. Experimental arrangement (a). Photo (b). Two-dimensional colour plots in time and position for He 706 nm (c) and N₂⁺ 391 nm (d). The position dependent plots at different instants of time for the 706 nm (black line) and N₂⁺ 391 nm (red line) (e). Both the gate width and the step width are 5 ns. The gain is set 250 a.u. The blue dashed line represents the crossing point of the axis of diagnosis tube and discharge capillary along y axis ($y = 0$ mm). Adapted with the permission from [109], Copyright 2024 Elsevier.

Chapter 5 Excitation and Ionisation of a Diagnosis Gas

respectively. The corresponding graphs for the emission intensities of *He* 706 nm and N_2^+ 391 nm as a function of position at different instants of time are shown in Figure 5.7 e. In this case, the $y = 0$ mm with the blue dashed line represents the position of the electrode tip along the diagnosis tube.

It can be seen clearly that the diagnosis gas is ignited. In addition, the emission propagates to both sides, with the direction of the diagnosis gas stream and against the direction of the diagnosis flow. Due to obstruction caused by the discharge capillary wall, fewer diagnosis gas atoms reach the positive side. Consequently, the emission of *He* 706 nm on the positive side only propagates approximately 1.5 mm away. Within the diagnosis tube, the emission of *He* 706 nm develops even 12 mm far away. This result further verifies that the discharge gas stream acts as a kind of curtain explained in Section 5.2, which blocks the diagnosis gas flow towards the positive y-axis.

A transient potential on the outer wall of the discharge capillary can be formed by the polarisation after ions are produced inside the discharge capillary. This potential attracts and accelerates electrons to be energetic ones, which collide with *He* atoms producing He^{**} , He^{*} , He^M . The maximum intensity of *He* 706 nm inside the diagnosis tube is always in front of the maximum intensity of the N_2^+ 391 nm signal. This is similar to the propagation of excitation and ionisation that occurs in the discharge capillary, where *He* is used as a discharge gas [92]. It should be noted that the emission of N_2^+ 391 nm at $y = 0$ mm can be observed over time due to the detachment of N_2^+ B $^2\Sigma_u^+$ from the discharge capillary.

In summary, it is not necessary to have a contact between a discharge plasma and a diagnosis gas to ignite a diagnosis plasma. Diagnosis gas can still be ignited even when separated by a glass media. This phenomenon is similar to a commercial plasma ball being able to ignite a lamp operating at low pressure or even a beam of gas at atmospheric pressure, as depicted in Figure 5.8. In this manner, the Penning ionisation, charge transfer, and excitation transfer between the discharge plasma and diagnosis gas for the excitation and ionisation of diagnosis gas can be completely excluded. Furthermore, the energy of photons released from *Ar*, *Kr* and *Xe* plasmas is not sufficient to excite *He* directly. Additionally, the silica glass of the capillary does not transmit radiation below 300 nm. Therefore, the excitation of *He* via a photoionisation process is not feasible.

In the first scenario, a transient potential is formed on the outer surface of the diagnosis tube. Such potential can be attributed to the production of ions in the ambient air such as N_2^+ , O_2^+ , H_3O^+ , etc. in front of the discharge capillary orifice. A transient potential is created on the inner surface of the diagnosis tube by polarisation in succession. In the second

5.4 The Closed micro-Tube Plasma

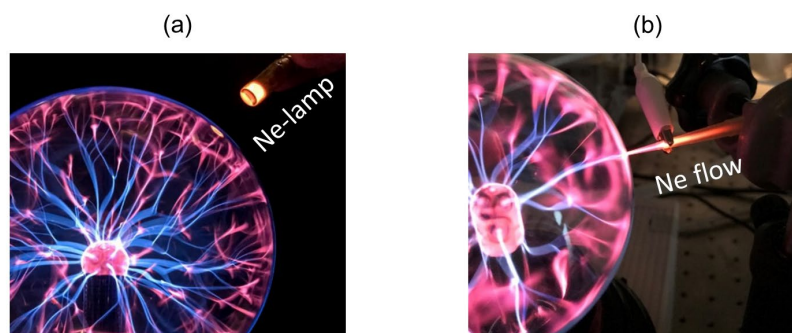


Figure 5.8: The ignition of a *Ne* lamp at low pressure (a) and a beam of *Ne* gas at atmospheric pressure (b) by a commercial plasma ball. Adapted with the permission from [109], Copyright 2024 Elsevier.

scenario, a transient potential is created on the inner surface of the discharge capillary, which in turn induces a corresponding potential on the outer surface via polarisation. The expression of transient potential is reminiscent of a process known from dielectric barrier discharges, where a fast-changing potential facilitates the discharge process. Once this potential is sufficient to breakdown the diagnosis gas or air components, the corresponding atoms or molecules can be excited and ionised. This explains why the ionisation efficiency of a *Xe*-F μ TP is similar to that of a *He*-F μ TP even if the energy of *Xe*⁺ is not sufficient to generate H₃O⁺ by collision. One possibility of receiving ions in the ambient air is that electrons are accelerated in the electrical field towards the transient potential, during which ions are produced by collisions.

The findings that a changing potential formed by a F μ TP ignites a diagnosis gas, rather than Penning ionisation, charge transfer or excitation transfer between the plasma and a diagnosis gas, open up new pathways for analytical applications. This breakthrough paves the way for the development of a new ionisation source, the Closed micro-Tube Plasma (C μ TP) [93,108]. The next section of this chapter will briefly describe the C μ TP, which is the end of the characterisation effort on the discharge mechanism and the study of soft ionisation throughout this thesis.

5.4 The Closed micro-Tube Plasma

The C μ TP is a new design according to the characterisation effort of the discharge in the F μ TP. The principal advantage of this novel design is its operation without the requirement

Chapter 5 Excitation and Ionisation of a Diagnosis Gas

for a continuous gas flow. A fixed discharge gas volume is trapped inside the closed column. No plasma gas supply is necessary and no gas consumption takes place. The common plasma is usually generated inside the capillary, and the plasma jet propagates into the ambient surrounding. The plasma jet and the analytes are in contact with each other. This closed design allows for a reliable operation where no excitation and ionisation waves can be passed beyond the glass into the ambient surrounding. The schematic of $C\mu TP$ operating during the positive half cycle of alternating voltage is shown in Figure 5.9 a [108].

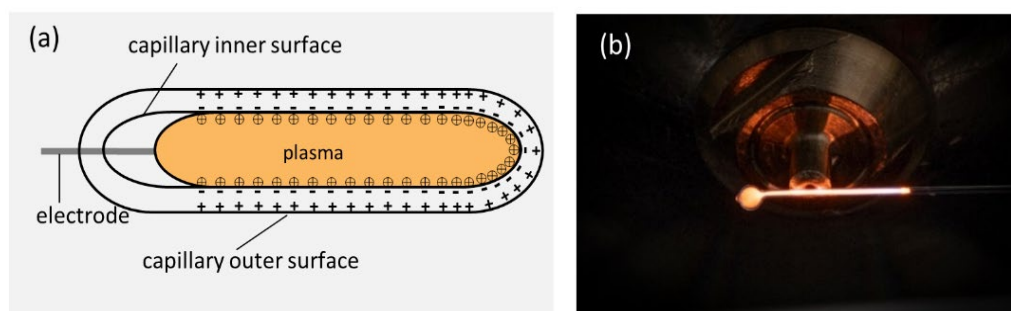


Figure 5.9: The schematic diagram of the $C\mu TP$. (a) Operating during the positive half cycle of an alternating voltage. (b) Photograph of a $Ne-C\mu TP$ in front of a MS inlet. Reprinted with the permission from [92], Copyright 2024 Springer.

A single wire electrode is inserted within a plasma gas filled capillary. It is sealed gas-tight at both ends, usually at ambient pressure. Upon application of a high voltage, a plasma is initiated within the capillary. The capillary is alternately polarised and depolarised independently of the plasma gas used. This makes it possible to ionise a gaseous sample without contact with the plasma when the sample flows over or at a short distance from the outer surface of the capillary. The sample ions are transferred to the analyser where they are analysed.

Another advantage is that the capillary takes up very little space. Thus, it can be easily positioned in the sample gas inlet region of an analyser. As shown in Figure 5.9 b, a $Ne-C\mu TP$ is arranged adjacent to the lower area of the inlet of a mass spectrometer. The ionisation efficiency of a self-made $C\mu TP$ as a soft ionisation source has been preliminarily investigated by MS measurements. Furthermore, its performance was compared to that of a $F\mu TP$. The results show that the detection strength of an $Ar-C\mu TP$ is approximately two times lower than that of an $Ar-F\mu TP$ [92].

However, the production of a $C\mu TP$ is not trivial since the capillary must be melted at two points during the flow of noble gas, which can lead to impurities in the gas. The bubble as

shown in Figure 5.9 b at one end of the *Ne*-C μ TP is a result of the current production process. The perfect production of a C μ TP in the lab has not yet been successful. Further improvement in the production and systematic investigation of C μ TP as an ionisation source is worth being pursued for analytical applications.

5.5 Conclusion

In this chapter, three different experimental setups were designed to deliver a diagnosis gas as a substitute for surrounding air. This aims to understand the generation and propagation of the diagnosis plasma outside the discharge capillary, as well as the soft ionisation mechanism.

In the first arrangement, the diagnosis gas *He* was introduced in front of the discharge capillary nozzle, where the discharge plasma was in contact with the diagnosis gas. It was shown that the diagnosis gas *He* is excited by a *Ne*-, *Ar*-, *Kr*- and *Xe*-F μ TP, even though all their energy states are not sufficient to excite *He* atoms to *He*** by collisions. The ignition of the diagnosis gas occurs only in the positive half cycle and not in the negative half cycle. This is consistent with the conclusion that the contribution for protonation in the negative half cycle is negligent. The propagation of the diagnosis plasma is related to the voltage applied to the discharge gases.

With further modifications, the separation of the discharge plasma and the diagnosis gas were realised by a glass wall, either by the wall of the diagnosis tube or the discharge capillary. The propagation of *He* 706 nm and N_2^+ 391 nm were also traced along the diagnosis tube. These findings demonstrated that a transient potential created via polarisation of the glass leads to the excitation of the diagnosis gas, rather than Penning ionisation, charge transfer, excitation transfer, or photoionisation between the discharge plasma and the diagnosis gas. Only the amount of charged species is a decisive factor in achieving excitation of the diagnosis gas, not their energy levels or lifetimes. It is reasonable to suppose that N_2^+ , O_2^+ , H_3O^+ , etc. could be produced in the electric field created by such potential in the ambient air and then involved in the protonation process. On the basis of these findings, a new plasma source, closed micro-tube plasma (C μ TP) was developed.

Summary and Outlook

This thesis focused on a systematic characterisation of the excitation and ionisation propagation in the F μ TP by introducing various noble gases first. The aim is to elucidate the fundamental excitation and ionisation mechanisms within the discharge capillary and their transitions to the ambient surrounding. On the basis of the interesting findings and acquired knowledge, the excitation and ionisation of a diagnosis gas in front of the F μ TP as well as inside the diagnosis tube was then elucidated. This provided insight into soft ionisation mechanisms that can be used for the improvement and expansion of discharges for analytical applications. Furthermore, the findings can be used as a basis for the construction of new ionisation sources.

The **Fundamentals** chapter introduced plasma-based ionisation sources used for soft ionisation as well as the evolution of the F μ TP. It also dealt with the diagnostic methods for plasmas, data acquisition and processing, discharge gases and diagnosis gas.

In part of chapter **F μ TP Ionisation Source: A Dielectric Guided Discharge, He (5.0)** was used as the discharge gas firstly to investigate the discharge mechanism in one discharge cycle under clean environmental conditions, using a discharge column length of 30 mm. One dielectric guided discharge along the capillary was identified in the positive half cycle. In the negative half cycle, one dielectric guided discharge along the capillary and one

Chapter 6 Summary and Outlook

negative glow discharge near the electrode were found. As a result of the higher electron density in the negative half cycle and the effect of the attached charges on the wall, the propagation was more continuous and faster compared to the case of the positive half cycle. This chapter identified the discharge in the F μ TP that is not a strict dielectric barrier discharge, but a dielectric guided discharge.

Another part of this chapter examines the effect of N₂ on the discharge by adding a controlled amount of N₂ to He (5.0) gas. A small concentration of N₂ in He favours the discharge. On the contrary, with a continuously increased concentration of N₂, the ionisation of the gas would become more difficult. With this modification, it was possible to experimentally identify the generation of N₂⁺ to be electron collision and Penning ionisation. It can be extended to ionisation outside the capillary.

In practice, F μ TP with a short discharge column is usually used for MS measurements. To align with practical applications, a discharge column with a length of 3 mm was used to investigate the discharge mechanism in the subsequent chapters. In the chapter **Discharge Mechanisms of the F μ TP**, the MS measurements revealed that F μ TP source operated with He, Ne, Ar, Kr and Xe achieved comparable ionisation efficiencies. This finding suggests that Penning ionisation, charge transfer, and photoionisation between the discharge plasmas and ambient air are not the primary ionisation mechanisms.

Detailed OES measurements recognised that there is a fundamental discharge difference between the He-, Ne-F μ TP and Ar-, Kr-, Xe-F μ TP inside the capillary. The discharge mainly depends on the components of the discharge gases and their associated energy levels. N₂⁺ are the dominant ions in a He- and Ne-F μ TP at low applied voltage, which are responsible for the excitation and ionisation propagation within the capillary. In an Ar-, Kr- and Xe-F μ TP, noble gas ions are generated and play a role in plasma propagation along the discharge capillary. This is the first time that the element ions can be distinguished from excited noble gas species in cold plasmas used for soft ionisation.

During the positive half cycle, all measured ions stop in the vicinity of the capillary outlet, and the excitation develops into the ambient surrounding. This finding suggests that a transient potential in the vicinity of the capillary outlet is formed by the ions generated in the plasma. With this potential, an electric field is created that decreases in space. When the electric field is sufficiently strong, air components could be ionised by collisions with energetic electrons, generating e.g. N₂⁺, O₂⁺, H₃O⁺, etc. These ions facilitate not only the excitation propagation of noble gases in the ambient air but also contribute to protonation processes.

However, positive ions are attracted by the negative electrode during the negative half cycle. No excitation exceeds the discharge capillary nozzle. It was explained that in this case the strength of a transient potential and thus the strength of an electric field in the vicinity of the capillary outlet are not sufficient to support further excitation and ionisation in ambient air. This leads to a negligent effect on protonation in the negative half cycle. The strength of such potential is independent of the type of the discharge gas, but is dependent on the number of charges.

Nevertheless, the emission wavelengths of air component ions are either unknown or missing, preventing their direct detection. For this reason, a different approach must be applied. In the chapter **Excitation and Ionisation of a Diagnosis Gas**, a diagnosis gas with known emission wavelengths was delivered as a substitute for the surrounding air.

Three experimental setups were designed. The diagnosis gas *He* is excited in all cases whether the discharge plasma is in contact with it or not. Penning ionisation, charge transfer, excitation transfer, or photoionisation between the discharge plasma and the diagnosis gas were completely excluded by using a glass wall in between. Furthermore, the role of a transient potential in the excitation of the diagnosis gas was confirmed. When the diagnosis gas *He* is substituted by ambient air, it can be understood that N_2 , H_2O and O_2 can be ionised even though their ionisation levels are higher than those of the noble gases used for the discharge.

The generated air component ions, on the one hand, support the excitation propagation of the noble gas outside the capillary. On the other hand, they participate in protonation processes. Therefore, the protonation outside the capillary is mainly attributed to a transient potential rather than to Penning ionisation, charge transfer, or photoionisation between the plasma and ambient air. This explains why the ionisation efficiency of a *Xe*-F μ TP is comparable to other noble gases driven plasmas even if the energy level of Xe^+ is lower than the ionisation level of H_2O . On the basis of these findings, a new idea was proposed using closed micro-tube plasma (C μ TP) as a soft ionisation source.

This C μ TP offers great economic benefits by eliminating the need for a continuous gas supply. Furthermore, the capillary takes up very little space and can be coupled to other analytical setups. This is very exciting and encouraging. The proposal of the C μ TP can be seen as an appropriate example of how conscientious study and characterisation of the basic discharge mechanisms can result in an alternative design suitable for soft ionisation. This advancement not only further supplements the ionisation source library, but also fosters the development of miniature analytical instrument.

Chapter 6 Summary and Outlook

However, as far as the C μ TP ionisation source itself is concerned, the production process has not yet been well established. It is not trivial or simple and can easily lead to impurities in the gas. The defect is that it might affect the discharge behaviour, and thereby the soft ionisation performance. Further attempts and efforts are needed to achieve better outcomes and applications.

Although in the present thesis a single ionisation source was primarily focused on and its ionisation characteristics were reported, the findings may potentially be applied to other plasma-based ionisation sources and definitely should be considered in future studies. These new insights emphasise the need for further research into the mechanisms of soft ionisation. A similar study would be interesting for other plasma-based ionisation sources to fully examine their overlooked ionisation mechanisms. A deeper understanding of the fundamental mechanisms and ionisation properties of these sources would improve ambient ionisation methodologies and help to explore new fields as well as exciting applications.

During the protonation process of the analytes, oxygen seems to be an important compound inside the ionisation atmosphere. An improved understanding of the ionisation process, including how oxygen is involved in the production of reactant ions, is beneficial for the optimisation of ionisation conditions.

In addition to the ionisation mechanism, the transport of the analyte ions is an important factor that affects the analytical performance. Normally, there is a space between the plasma source and the mass spectrometer inlet. An electric field is created in this area in which the ions are accelerated into the mass spectrometer. In addition to the present electric field, the use of an extra electric field by applying a DC voltage may help guide ions into the mass spectrometer. A better understanding of these transport processes and the potential impact factor could further improve the analytical applications of F μ TP sources. This may also contribute to the idea for other plasma-based ionisation sources on the ionisation mechanism and efficiency.

Bibliography

1. Dole M, Mack LL, Hines RL, Mobley RC, Ferguson LD, Alice MB (1968) Molecular beams of macroions. *The Journal of chemical physics* 49 (5):2240-2249
2. Fenn JB, Mann M, Meng CK, Wong SF, Whitehouse CM (1989) Electrospray ionization for mass spectrometry of large biomolecules. *Science* 246 (4926):64-71
3. Horning E, Horning M, Carroll D, Dzidic I, Stillwell R (1973) New picogram detection system based on a mass spectrometer with an external ionization source at atmospheric pressure. *Anal Chem* 45 (6):936-943
4. Cody RB, Laramée JA, Durst HD (2005) Versatile new ion source for the analysis of materials in open air under ambient conditions. *Anal Chem* 77 (8):2297-2302
5. Na N, Zhao M, Zhang S, Yang C, Zhang X (2007) Development of a dielectric barrier discharge ion source for ambient mass spectrometry. *J Am Soc Mass Spectrom* 18 (10):1859-1862
6. Na N, Zhang C, Zhao M, Zhang S, Yang C, Fang X, Zhang X (2007) Direct detection of explosives on solid surfaces by mass spectrometry with an ambient ion source based on dielectric barrier discharge. *J Mass Spectrom* 42 (8):1079-1085
7. Harper JD, Charipar NA, Mulligan CC, Zhang X, Cooks RG, Ouyang Z (2008) Low-temperature plasma probe for ambient desorption ionization. *Anal Chem* 80 (23):9097-9104
8. Andrade FJ, Shelley JT, Wetzel WC, Webb MR, Gamez G, Ray SJ, Hieftje GM (2008) Atmospheric pressure chemical ionization source. 1. Ionization of compounds in the gas phase. *Anal Chem* 80 (8):2646-2653
9. Brandt S, Klute FD, Schütz A, Marggraf U, Drees C, Vogel P, Vautz W, Franzke J (2018) Flexible microtube plasma (F μ TP) as an embedded ionization source for a microchip mass spectrometer interface. *Anal Chem* 90 (17):10111-10116
10. Ding X, Duan Y (2015) Plasma - based ambient mass spectrometry techniques: The current status and future prospective. *Mass Spectrom Rev* 34 (4):449-473
11. Yue H, He F, Zhao Z, Duan Y (2023) Plasma - based ambient mass spectrometry: Recent progress and applications. *Mass Spectrom Rev* 42 (1):95-130
12. Ayala-Cabrera JF, Turkowski J, Uteschil F, Schmitz OJ (2022) Development of a Tube Plasma Ion Source for Gas Chromatography–Mass Spectrometry Analysis and Comparison with Other Atmospheric Pressure Ionization Techniques. *Anal Chem* 94 (27):9595-9602
13. Shahin M (1966) Mass - spectrometric studies of corona discharges in air at atmospheric pressures. *The Journal of Chemical Physics* 45 (7):2600-2605
14. Dzidic I, Carroll D, Stillwell R, Horning E (1976) Comparison of positive ions formed in nickel-63 and corona discharge ion sources using nitrogen, argon, isobutane, ammonia and nitric oxide as reagents in atmospheric pressure ionization mass spectrometry. *Anal Chem* 48 (12):1763-1768
15. Hayen H, Michels A, Franzke J (2009) Dielectric barrier discharge ionization for liquid chromatography/mass spectrometry. *Anal Chem* 81 (24):10239-10245

Bibliography

16. Brandt S, Klute FD, Schütz A, Franzke J (2017) Dielectric barrier discharges applied for soft ionization and their mechanism. *Anal Chim Acta* 951:16-31
17. Chan GC-Y, Shelley JT, Wiley JS, Engelhard C, Jackson AU, Cooks RG, Hieftje GM (2011) Elucidation of reaction mechanisms responsible for afterglow and reagent-ion formation in the low-temperature plasma probe ambient ionization source. *Anal Chem* 83 (10):3675-3686
18. Penning F (1927) Über ionisation durch metastabile atome. *Naturwissenschaften* 15 (40):818-818
19. Bell K, Dalgarno A, Kingston A (1968) Penning ionization by metastable helium atoms. *Journal of Physics B: Atomic and Molecular Physics* 1 (1):18
20. Ayala-Cabrera JF, Montero L, Meckelmann SW, Uteschil F, Schmitz OJ (2023) Review on atmospheric pressure ionization sources for gas chromatography-mass spectrometry. Part I: Current ion source developments and improvements in ionization strategies. *Anal Chim Acta* 1238:340353
21. Brecht D, Uteschil F, Schmitz OJ (2021) Development of an inverse low - temperature plasma ionization source for liquid chromatography/mass spectrometry. *Rapid Commun Mass Spectrom* 35 (10):e9071
22. Bogaerts A (2007) The afterglow mystery of pulsed glow discharges and the role of dissociative electron-ion recombination. *J Anal At Spectrom* 22 (5):502-512
23. Hiraoka K, Fujimaki S, Kambara S, Furuya H, Okazaki S (2004) Atmospheric - pressure Penning ionization mass spectrometry. *Rapid Commun Mass Spectrom* 18 (19):2323-2330
24. Horvatic V, Müller S, Veza D, Vadla C, Franzke J (2014) Atmospheric helium capillary dielectric barrier discharge for soft ionization: determination of atom number densities in the lowest excited and metastable states. *Anal Chem* 86 (1):857-864
25. Badal SP, Michalak SD, Chan GC-Y, You Y, Shelley JT (2016) Tunable ionization modes of a flowing atmospheric-pressure afterglow (FAPA) ambient ionization source. *Anal Chem* 88 (7):3494-3503
26. Baricholo P, Hlatywayo DJ, Collier M, Von Bergmann HM, Stehmann T, Rohwer E (2011) Influence of gas discharge parameters on emissions from a dielectric barrier discharge excited argon excimer lamp. *South African Journal of Science* 107 (11):1-7
27. Zhang J-Y, Boyd IW (1998) Efficient Xe* excimer ultraviolet sources from a dielectric barrier discharge. *J Appl Phys* 84 (3):1174-1178
28. Dempster A (1918) A new method of positive ray analysis. *Phys Rev* 11 (4):316
29. Albritton DL, Miller T, Martin D, McDaniel E (1968) Mobilities of mass-identified H³⁺ and H⁺ ions in hydrogen. *Phys Rev* 171 (1):94
30. Hu Q, Noll RJ, Li H, Makarov A, Hardman M, Graham Cooks R (2005) The Orbitrap: a new mass spectrometer. *J Mass Spectrom* 40 (4):430-443
31. Kanu AB, Dwivedi P, Tam M, Matz L, Hill Jr HH (2008) Ion mobility-mass spectrometry. *J Mass Spectrom* 43 (1):1-22
32. Snyder DT, Pulliam CJ, Ouyang Z, Cooks RG (2016) Miniature and fieldable mass spectrometers: recent advances. *Anal Chem* 88 (1):2-29
33. McLafferty F (1993) Interpretation of mass spectra *University Science Books*
34. Carroll D, Dzidic I, Stillwell RN, Haegele KD, Horning EC (1975) Atmospheric pressure ionization mass spectrometry. Corona discharge ion source for use in a liquid chromatograph-mass spectrometer-computer analytical system. *Anal Chem* 47 (14):2369-2373
35. Lara-Ortega FJ, Robles-Molina J, Brandt S, Schütz A, Gilbert-López B, Molina-Díaz A, García-Reyes JF, Franzke J (2018) Use of dielectric barrier discharge ionization to minimize matrix effects and expand coverage in pesticide residue analysis by liquid chromatography-mass spectrometry. *Anal Chim Acta* 1020:76-85
36. Pape A, Schmitz OJ (2023) Dielectric barrier discharge in mass spectrometry—An overview over plasma investigations and ion sources applications. *TrAC, Trends Anal Chem*:117420
37. Foest D (2023) Development and characterisation of quasisimultaneous electrospray and plasma ionisation for the analysis of polar and less polar compounds in mass spectrometry.
38. Klute FD, Michels A, Schütz A, Vadla C, Horvatic V, Franzke J (2016) Capillary dielectric barrier discharge: transition from soft ionization to dissociative plasma. *Anal Chem* 88 (9):4701-4705

39. Nijdam S, Teunissen J, Ebert U (2020) The physics of streamer discharge phenomena. *Plasma Sources Sci Technol* 29 (10):103001
40. Bradshaw SJ, Raymond J (2014) Collisional and radiative processes in optically thin plasmas. *Microphysics of Cosmic Plasmas*:195-230
41. Hodgman S, Dall R, Byron L, Baldwin K, Buckman S, Truscott A (2009) Metastable helium: A new determination of the longest atomic excited-state lifetime. *Phys Rev Lett* 103 (5):053002
42. Miller W, Morgner H (1977) A unified treatment of Penning ionization and excitation transfer. *The Journal of Chemical Physics* 67 (11):4923-4930
43. Somogyi Á (2008) Chapter 6 - Mass spectrometry instrumentation and techniques. In: Vékey K, Telekes A, Vertes A (eds) *Medical Applications of Mass Spectrometry*. Elsevier, Amsterdam, pp 93-140.
44. Good A, Durden DA, Kebarle P (1970) Ion-molecule reactions in pure nitrogen and nitrogen containing traces of water at total pressures 0.5–4 Torr. Kinetics of clustering reactions forming H⁺(H₂O)_n. *The Journal of Chemical Physics* 52 (1):212-221
45. Takats Z, Wiseman JM, Gologan B, Cooks RG (2004) Mass spectrometry sampling under ambient conditions with desorption electrospray ionization. *Science* 306 (5695):471-473
46. Ding X, Zhan X, Yuan X, Zhao Z, Duan Y (2013) Microfabricated glow discharge plasma (MFGDP) for ambient desorption/ionization mass spectrometry. *Anal Chem* 85 (19):9013-9020
47. Ma X, Ouyang Z (2016) Ambient ionization and miniature mass spectrometry system for chemical and biological analysis. *TrAC, Trends Anal Chem* 85:10-19
48. Kogelschatz U, Eliasson B, Egli W (1997) Dielectric-barrier discharges. Principle and applications. *Le Journal de Physique IV* 7 (C4):C4-47-C44-66
49. Gibalov VI, Pietsch GJ (2012) Dynamics of dielectric barrier discharges in different arrangements. *Plasma Sources Sci Technol* 21 (2):024010
50. Olenici-Craciunescu S, Michels A, Meyer C, Heming R, Tombrink S, Vautz W, Franzke J (2009) Characterization of a capillary dielectric barrier plasma jet for use as a soft ionization source by optical emission and ion mobility spectrometry. *Spectrochimica Acta Part B: Atomic Spectroscopy* 64 (11-12):1253-1258
51. Griffiths DJ (2023) Introduction to electrodynamics *Cambridge University Press*
52. Jackson JD (2021) Classical electrodynamics *John Wiley & Sons*
53. Niu G, Knodel A, Burhenn S, Brandt S, Franzke J (2021) Miniature dielectric barrier discharge (DBD) in analytical atomic spectrometry. *Anal Chim Acta* 1147:211-239
54. Meyer C, Müller S, Gurevich E, Franzke J (2011) Dielectric barrier discharges in analytical chemistry. *Analyst* 136 (12):2427-2440
55. Michels A, Tombrink S, Vautz W, Miclea M, Franzke J (2007) Spectroscopic characterization of a microplasma used as ionization source for ion mobility spectrometry. *Spectrochimica Acta Part B: Atomic Spectroscopy* 62 (11):1208-1215
56. Klute FD, Brandt S, Vogel P, Biskup B, Reiningner C, Horvatic V, Vadla C, Farnsworth PB, Franzke J (2017) Systematic comparison between half and full dielectric barrier discharges based on the low temperature plasma probe (LTP) and dielectric barrier discharge for soft ionization (DBDI) configurations. *Anal Chem* 89 (17):9368-9374
57. Liu Y, Lin Z, Zhang S, Yang C, Zhang X (2009) Rapid screening of active ingredients in drugs by mass spectrometry with low-temperature plasma probe. *Analytical and bioanalytical chemistry* 395:591-599
58. Horvatic V, Michels A, Ahlmann N, Jestel G, Veza D, Vadla C, Franzke J (2015) Time-resolved spectroscopy of a homogeneous dielectric barrier discharge for soft ionization driven by square wave high voltage. *Analytical and bioanalytical chemistry* 407:7973-7981
59. Horvatic V, Michels A, Ahlmann N, Jestel G, Veza D, Vadla C, Franzke J (2015) Time- and spatially resolved emission spectroscopy of the dielectric barrier discharge for soft ionization sustained by a quasi-sinusoidal high voltage. *Analytical and bioanalytical chemistry* 407:6689-6696
60. Schütz A, Klute FD, Brandt S, Liedtke S, Jestel Gn, Franzke J (2016) Tuning soft ionization strength for organic mass spectrometry. *Anal Chem* 88 (10):5538-5541
61. Klute FD (2019) Characterization of dielectric barrier discharges for analytical applications. Dissertation, Dortmund, Technische Universität, 2020,

Bibliography

62. Klute FD, Brandt S, Franzke J (2021) Spatiotemporal characterization of different dielectric barrier discharges designed for soft ionization. *Spectrochimica Acta Part B: Atomic Spectroscopy* 176:106037
63. Knodel A, Foest D, Brandt S, Ahlmann N, Marggraf U, Gilbert-López B, Franzke J (2020) Detection and evaluation of lipid classes and other hydrophobic compounds using a laser desorption/plasma ionization interface. *Anal Chem* 92 (22):15212-15220
64. Knodel A, Marggraf U, Ahlmann N, Brandt S, Foest D, Gilbert-López B, Franzke J (2020) Standardization of Sandwich-Structured Cu–Glass Substrates Embedded in a Flexible Diode Laser–Plasma Interface for the Detection of Cholesterol. *Anal Chem* 92 (6):4663-4671
65. Moreno-González D, Castilla-Fernández D, Vogel P, Niu G, Brandt S, Drees C, García-Reyes JF, Molina-Díaz A, Franzke J (2021) Evaluation of a novel controlled-atmosphere flexible microtube plasma soft ionization source for the determination of BTEX in olive oil by headspace-gas chromatography/mass spectrometry. *Anal Chim Acta* 1179:338835
66. Tian C, Speicher L, Xue D, Moreno-González D, Marggraf U, Ahlmann N, Brandt S, Franzke J, Niu G (2022) Ionization of semi-fluorinated n - alkanes in controlled atmosphere using flexible microtube plasma (F μ TP) ionization source with square-and sine-wave voltage. *Talanta*:123662
67. Drees C, Schütz A, Niu G, Franzke J, Vautz W, Brandt S (2020) Stepwise optimization of a Flexible Microtube Plasma (F μ TP) as an ionization source for Ion Mobility Spectrometry. *Anal Chim Acta* 1127:89-97
68. Vogel P, Lazarou C, Gazeli O, Brandt S, Franzke J, Moreno-González D (2020) Study of controlled atmosphere flexible microtube plasma soft ionization mass spectrometry for detection of volatile organic compounds as potential biomarkers in saliva for cancer. *Anal Chem* 92 (14):9722-9729
69. Foest D, Knodel A, Brandt S, Franzke J (2022) Coupling paper spray ionization with the flexible microtube plasma for the determination of low polar biomarkers in mass spectrometry. *Anal Chim Acta* 1201:339619
70. Foest D, Knodel A, Ahrends R, Coman C, Franzke J, Brandt S (2023) Flexible Microtube Plasma for the Consecutive-Ionization of Cholesterol in Nano-Electrospray Mass Spectrometry. *Anal Chem*
71. Bengtson A (2019) Optical Emission Spectroscopy. In: *Materials Characterization*, vol 10. ASM International, p 0.
72. Kirchhoff G, Bunsen R (1860) Chemical analysis by observation of spectra. *Annalen der Physik und der Chemie* 110:161-189
73. Chen FF, Chang JP (2003) Optical Emission Spectroscopy. In: *Lecture Notes on Principles of Plasma Processing*. Springer US, Boston, MA, pp 151-160.
74. Hanna AR, Fisher ER (2020) Investigating recent developments and applications of optical plasma spectroscopy: A review. *Journal of Vacuum Science & Technology A* 38 (2).
75. Albert E (1905) On a heuristic viewpoint concerning the production and transformation of light. *Annalen der Physik* 17:132-148
76. Cassidy DC, Holton GJ (2002) *Floyd James Rutherford Understanding physics*. Birkhäuser,
77. USB4000 Fiber Optic Spectrometer Installation and Operation Manual.
78. Fraunhofer J (1823) Kurzer Bericht von den Resultaten neuerer Versuche über die Gesetze des Lichtes, und die Theorie derselben. *Annalen der Physik* 74 (8):337-378
79. Tian C, Ahlmann N, Brandt S, Franzke J, Niu G (2021) Optical characterization of miniature flexible micro-tube plasma (F μ TP) ionization source: A dielectric guided discharge. *Spectrochimica Acta Part B: Atomic Spectroscopy* 181:106222
80. Wu S, Lu X, Yue Y, Dong X, Pei X (2016) Effects of the tube diameter on the propagation of helium plasma plume via electric field measurement. *Physics of Plasmas* 23 (10)
81. Sretenović GB, Guaitella O, Sobota A, Krstić IB, Kovačević VV, Obradović BM, Kuraica MM (2017) Electric field measurement in the dielectric tube of helium atmospheric pressure plasma jet. *J Appl Phys* 121 (12)
82. Bourdon A, Darny T, Pechereau F, Pouvesle J-M, Viegas P, Iséni S, Robert E (2016) Numerical and experimental study of the dynamics of a μ s helium plasma gun discharge with various amounts of N₂ admixture. *Plasma Sources Sci Technol* 25 (3):035002
83. Staack D, Farouk B, Gutsol A, Fridman A (2005) Characterization of a dc atmospheric pressure normal glow discharge. *Plasma Sources Sci Technol* 14 (4):700

84. Staack D, Farouk B, Gutsol A, Fridman A (2008) DC normal glow discharges in atmospheric pressure atomic and molecular gases. *Plasma Sources Sci Technol* 17 (2):025013
85. Wang R, Zhang K, Shen Y, Zhang C, Zhu W, Shao T (2016) Effect of pulse polarity on the temporal and spatial emission of an atmospheric pressure helium plasma jet. *Plasma Sources Sci Technol* 25 (1):015020
86. Ball DW, Key JA (2014) Chapter 17 Introductory Chemistry – 1st Canadian Edition. Victoria, B.C.: BCcampus. <https://opentextbc.ca/introductorychemistry>.
87. Lofthus A, Krupenie PH (1977) The spectrum of molecular nitrogen. *J Phys Chem Ref Data* 6 (1):113-307. doi:10.1063/1.555546
88. Krupenie PH (1972) The Spectrum of Molecular Oxygen. *J Phys Chem Ref Data* 1 (2):423-534.
89. Ascenzi D, Franceschi P, Guella G, Tosi P (2006) Phenol production in benzene/air plasmas at atmospheric pressure. Role of radical and ionic routes. *The Journal of Physical Chemistry A* 110 (25):7841-7847
90. Gibson AR, Donkó Z, Alelyani L, Bischoff L, Hübner G, Bredin J, Doyle S, Korolov I, Niemi K, Mussenbrock T (2019) Disrupting the spatio-temporal symmetry of the electron dynamics in atmospheric pressure plasmas by voltage waveform tailoring. *Plasma Sources Sci Technol* 28 (1):01LT01
91. Song H, Tian C, Speicher L, Ahlmann N, Brandt S, Niu G, Franzke J (2024) Elucidation of discharge mechanisms in He- and Ar-flexible μ -tube plasmas by temporally and spatially resolved plasma optical emission Phoresis spectroscopy. *Spectrochimica Acta Part B: Atomic Spectroscopy*:107014
92. Speicher L, Song H, Ahlmann N, Foest D, Höving S, Brandt S, Niu G, Franzke J, Tian C (2024) Soft ionization mechanisms in flexible μ -tube plasma—from F μ TP to closed μ -tube plasma. *Analytical and Bioanalytical Chemistry*:1-9
93. Tian C, Song H, Ahlmann N, Brandt S, Foest D, Niu G, Franzke J, Speicher L (2024) Soft ionization mechanisms in flexible μ -tube plasma—elucidation of He-, Ar-, Kr-, and Xe-F μ TP. *Analytical and Bioanalytical Chemistry*:1-12
94. Tian C, Speicher L, Song H, Ahlmann N, Brandt S, Niu G, Franzke J (2025) Study of the discharge mode transition in a Ne-flexible micro-tube plasma (F μ TP). *Spectrochimica Acta Part B: Atomic Spectroscopy*:107180
95. Blake RS, Monks PS, Ellis AM (2009) Proton-transfer reaction mass spectrometry. *Chem Rev* 109 (3):861-896
96. NIST Atomic Spectra Database <https://dx.doi.org/10.18434/T4W30F>.
97. Carman R, Kane D, Ward B (2009) Enhanced performance of an EUV light source ($\lambda = 84$ nm) using short-pulse excitation of a windowless dielectric barrier discharge in neon. *J Phys D: Appl Phys* 43 (2):025205
98. Hirose K, Sugahara H, Matsuno H (2002) Basic performance of VUV exposure systems using head-on type Ar 2^* and Kr 2^* DBD excimer lamps. *Journal of Light & Visual Environment* 26 (1):1_35-31_41
99. Robert E, Sarron V, Ries D, Dozias S, Vandamme M, Pouvesle JM (2012) Characterization of pulsed atmospheric-pressure plasma streams (PAPS) generated by a plasma gun. *Plasma Sources Sci Technol* 21 (3):034017
100. Xiong Z, Kushner MJ (2012) Atmospheric pressure ionization waves propagating through a flexible high aspect ratio capillary channel and impinging upon a target. *Plasma Sources Sci Technol* 21 (3):034001
101. Gherardi M, Puač N, Marić D, Stancampiano A, Malović G, Colombo V, Petrović ZL (2015) Practical and theoretical considerations on the use of ICCD imaging for the characterization of non-equilibrium plasmas. *Plasma Sources Sci Technol* 24 (6):064004
102. Pinchuk M, Nikiforov A, Snetov V, Chen Z, Leys C, Stepanova O (2021) Role of charge accumulation in guided streamer evolution in helium DBD plasma jets. *Scientific reports* 11 (1):1-11
103. Schütz A, Lara-Ortega FJ, Klute FD, Brandt S, Schilling M, Michels A, Veza D, Horvatic V, Garcia-Reyes JF, Franzke J (2018) Soft argon–propane dielectric barrier discharge ionization. *Anal Chem* 90 (5):3537-3542
104. Heylen A (1968) Ionization coefficients and sparking voltages in argon-methane and argon-propane mixtures. *International Journal of Electronics* 24 (2):165-175

Bibliography

105. Klute F, Schütz A, Michels A, Vadla C, Veza D, Horvatic V, Franzke J (2016) An experimental study on the influence of trace impurities on ionization of atmospheric noble gas dielectric barrier discharges. *Analyst* 141 (20):5842-5848
106. Sobelman I (2012) Atomic spectra and radiative transitions Prof Dr. Günter Ecker PDPL, Prof Igor I. Sobelman, Prof Dr. Herbert Walther. 12. *Springer Science & Business Media*
107. Docenko D, Sunyaev R (2008) Optical and near-infrared recombination lines of oxygen ions from Cassiopeia A knots. *Astronomy & Astrophysics* 484 (3):755-771
108. Franzke J, Tian C, Speicher L, Brandt S, Foest D, Höving S, Ahlmann N (2023) Verfahren zur Ionisierung von gasförmigen Proben mittels Gasentladung. Germany Patent 10 2022121 736.1,
109. Song H, Tian C, Speicher L, Ahlmann N, Foest D, Höving S, Brandt S, Niu G, Franzke J (2024) Excitation and ionization of a diagnosis gas in front of the flexible μ tube plasma and in a diagnosis tube. *Spectrochimica Acta Part B: Atomic Spectroscopy*:107052

Appendix

A. F μ TP Ionisation Source: A Dielectric Guided Discharge

A.1 Positive bias square wave voltage

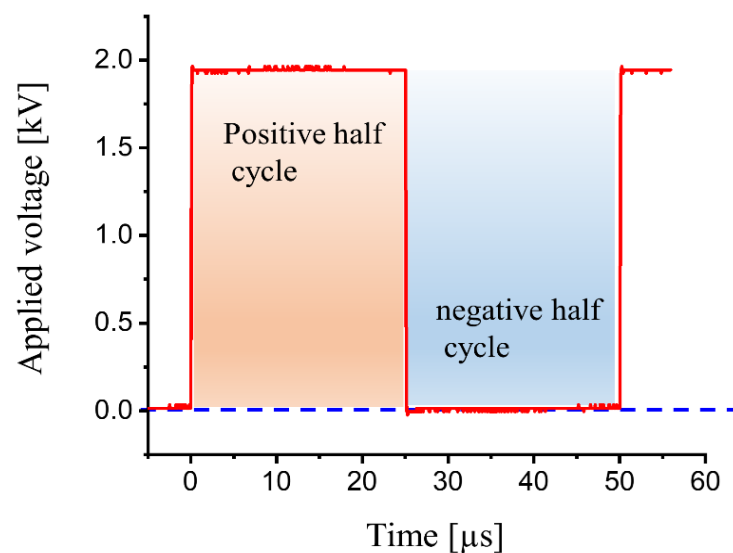


Figure A.1: Diagram of positive bias square wave voltage. This diagram is an example of an applied voltage of 2.0 kV. The orange background represents the positive half cycle and the blue background for the negative half cycle. The dashed blue line represents the 0.0 kV.

Appendix

A.2 Optical transitions of excited He, N₂ and O

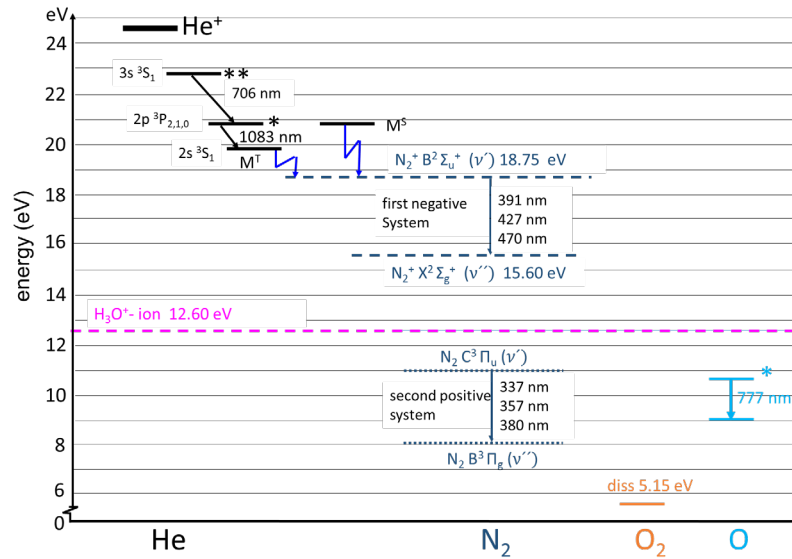


Figure A.2: Diagram of optical transitions of excited He with their respective wavelengths and excitation and ionisation energies for nitrogen and oxygen species.

B. Discharge Mechanisms of the F_μTP

B.1 Bi-polar square wave voltage

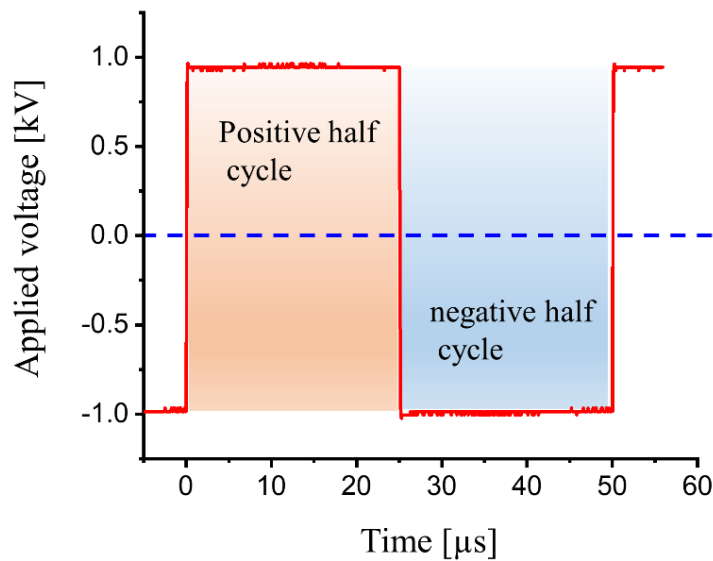


Figure B.1: Diagram of bi-polar square wave voltage. This diagram is an example of an applied voltage of 2.0 kV. The orange background represents the positive half cycle and the blue background for the negative half cycle. The dashed blue line represents the 0.0 kV.

B.2 Experimental setup for a Xe-F μ TP

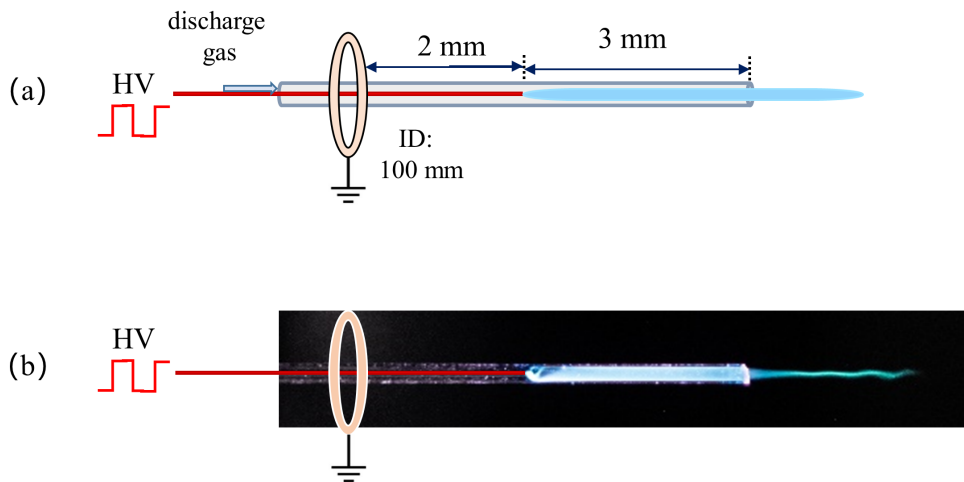


Figure B.2: Experimental setup for a Xe-F μ TP. (a) Schematic of the experimental setup. (b) Photograph. The ring with an inner diameter of 100 mm is grounded.

B.3 Simulation of the overlap of two Gaussian peaks

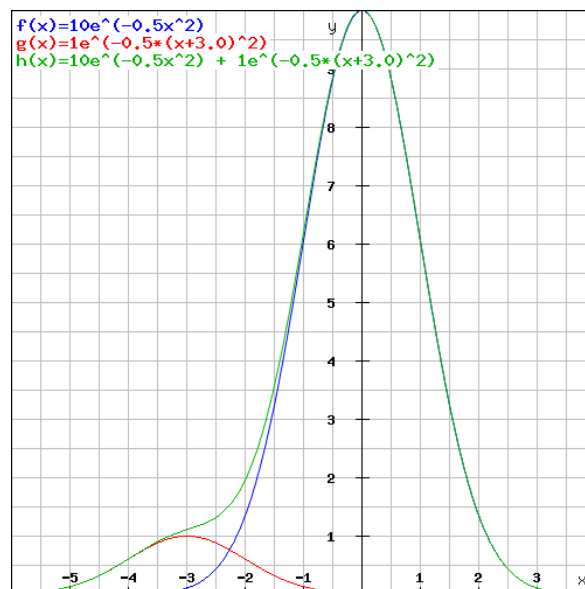


Figure B.3: Schematic of the overlap of two Gaussian peaks. The function of each peak is given on the top of the Figure. The green peak is the result of overlapping blue and red peaks.

Appendix

B.4 Ne plasma propagation operating at 2.0 kV

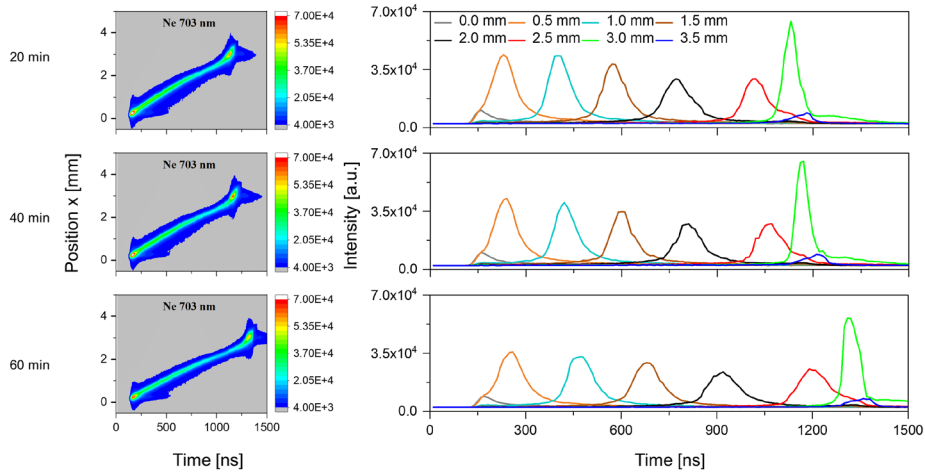


Figure B.4: Two dimensional colour plot in time and position and the related phoresis plots for the emission intensities as a function of time at different positions for Ne 703 nm signal measured at different time of plasma running, 20 min, 40 min and 60 min. The applied voltage is 2.0 kV.

B.5 Comparison of He 706 nm measured at different voltage

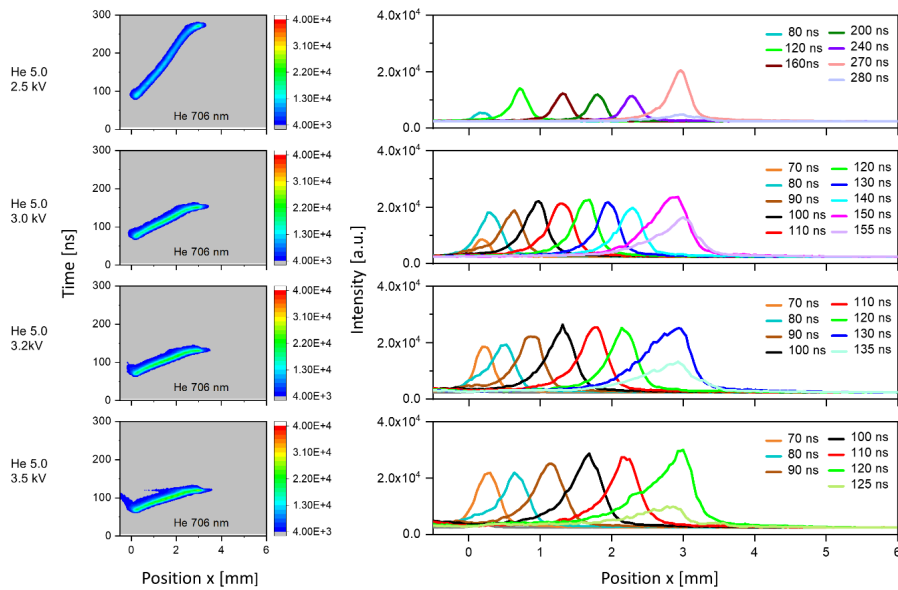


Figure B.5: Comparison of He 706 nm measured at different voltages. Two-dimensional colour plots and the position dependent plots of He 706 nm at different voltages in the positive half cycle. The gate width and gate step width are 5 ns. The gain is 200 a.u.

List of Publications and Patent

Peer-reviewed Articles (relevant for this work)

- P1 **Caiyan Tian**, Norman Ahlmann, Sebastian Brandt, Joachim Franzke, Guanghui Niu*
Optical characterization of miniature flexible micro-tube plasma (F μ TP) ionisation source: A dielectric guided discharge
Spectrochimica Acta Part B: Atomic Spectroscopy, **2021**,
DOI: 10.1016/j.sab.2021.106222
- P2 Luisa Speicher, Hao Song, Norman Ahlmann, Daniel Foest, Simon Höving, Sebastian Brandt, Guanghui Niu, Joachim Franzke*, **Caiyan Tian***
Soft ionisation mechanisms in flexible μ -tube plasma—from F μ TP to closed μ -tube plasma
Analytical and Bioanalytical Chemistry, **2024**,
DOI: 10.1007/s00216-024-05420-8
- P3 **Caiyan Tian**, Hao Song, Norman Ahlmann, Sebastian Brandt, Daniel Foest, Guanghui Niu, Joachim Franzke*, Luisa Speicher*
Soft ionisation mechanisms in flexible μ -tube plasma—elucidation of He-, Ar-, Kr-, and Xe-F μ TP
Analytical and Bioanalytical Chemistry, **2024**,
DOI: 10.1007/s00216-024-05419-1
- P4 **Caiyan Tian**, Luisa Speicher, Hao Song, Norman Ahlmann, Sebastian Brandt, Guanghui Niu, Joachim Franzke*
Study of the discharge mode transition in a Ne-Flexible μ -Tube Plasma
Spectrochimica Acta Part B: Atomic Spectroscopy, **2025**,
DOI: 10.1016/j.sab.2025.107180
- P5 Hao Song, **Caiyan Tian**, Luisa Speicher, Norman Ahlmann, Sebastian Brandt, Guanghui Niu, Joachim Franzke*
Elucidation of discharge mechanisms in He- and Ar-flexible μ -tube plasmas by temporally and spatially resolved plasma optical emission phoresis spectroscopy
Spectrochimica Acta Part B: Atomic Spectroscopy, **2024**,
DOI: 10.1016/j.sab.2024.107014
- P6 Hao Song¹, **Caiyan Tian**¹, Luisa Speicher, Norman Ahlmann, Daniel Foest, Simon Höving, Sebastian Brandt, Guanghui Niu, Joachim Franzke*

List of Publications and Patent

Excitation and ionisation of a diagnosis gas in front of the flexible μ tube plasma and in a diagnosis tube

Spectrochimica Acta Part B: Atomic Spectroscopy, **2024**,

DOI: 10.1016/j.sab.2024.107052

Further Peer-reviewed Article

- **Caiyan Tian**¹, Luisa Speicher¹, Dengqi Xue, David Moreno-González, Ulrich Marggraf, Norman Ahlmann, Sebastian Brandt, Joachim Franzke, Guanghui Niu*
Ionisation of semi-fluorinated n-alkanes in controlled atmosphere using flexible micro-tube plasma (F μ TP) ionisation source with square- and sine-wave voltage
Talanta, **2022**,

DOI: 10.1016/j.talanta.2022.123662

Patent

- Joachim Franzke, **Caiyan Tian**, Luisa Speicher, Sebastian Brandt, Daniel Foest, Simon Höving, Norman Ahlmann
Verfahren zur Ionisierung von gasförmigen Proben mittels Gasentladung
Published as: DE102022121736B3
Leibniz Institut für Analytische Wissenschaften - ISAS - e.V. **2023**.

Presentations

- **Caiyan Tian**, Norman Ahlmann, Sebastian Brandt, Guanghui Niu, Joachim Franzke
Elucidation of discharge mechanism in *He*-, *Ne*, *Ar*, *Kr*, *Xe*-Flexible μ Tube and their transition to ambient air
The 5th International Symposium on Frontiers of Plasma and Energy Conversion
Nanjing, China, 27. Oct. 2023 - 29. Oct. 2023
- **Caiyan Tian**, Luisa Speicher, Hao Song, Norman Ahlmann, Sebastian Brandt, Daniel Foest, Guanghui Niu, Joachim Franzke
Discharge mechanism of Flexible μ -Tube Plasma for analytical applications
The 33rd International Conference on Ion Mobility Spectrometry
Miami Beach, USA, 20. Jul. 2023 - 26. Jul. 2024

Declaration of Pre-Published Contents

Parts of this thesis were already published by the author in articles (P1-P6), presentations and posters. This thesis contains the following reproductions:

Chapter 1

1.1

1.2

Chapter 2

content partly published in P1 - P6

2.1

2.1.1

2.1.2

2.1.3

2.1.4

content partly published in P1 - P6

2.2

2.2.1

2.2.2

2.2.3

2.3

2.3.1

content partly published in P1

2.3.2

content partly published in P1

2.4

content partly published in P1 - P6

Chapter 3

content partly published in P1

3.1

content partly published in P1

3.2

content partly published in P1

3.3

content partly published in P1

	3.3.1	content partly published in	P1
	3.3.2	content partly published in	P1
	3.3.3	content partly published in	P1
	4.4	content partly published in	P1
Chapter 4		content partly published in	P2 - P5
	4.1	content partly published in	P2, P3
	4.2		
	4.2.1	content partly published in	P3 - P5
	4.2.2	content partly published in	P3 - P4
	4.2.3	content partly published in	P3 - P5
	4.2.4	content partly published in	P3 - P4
	4.2.5	content partly published in	P3
	4.2.6	content partly published in	P5
	4.3	content partly published in	P2 - P5
Chapter 5		content partly published in	P2, P6
	5.1	content partly published in	P6
	5.2	content partly published in	P6
	5.3		
	5.3.1	content partly published in	P6
	5.3.2	content partly published in	P6
	5.4	content partly published in	P2
	5.5	content partly published in	P2, P6
Chapter 6			

Acknowledgements

I would like to thank all those people who have provided invaluable assistance and supported me, without whom this dissertation would not have been possible.

Firstly, I extend my deepest gratitude to PD Dr. Joachim Franzke, my doctoral supervisor, who spares no effort in developing plasmas with his wise insight and ability to carry out critical investigations. I've always been inspired by his passion for scientific work and fascination with things. His patient discussion, tolerance, openness, kindness, relaxed and pleasant working atmosphere He creates have made my doctoral journey very enjoyable. I am going to benefit from it for the rest of my life.

I would also like to thank Prof. Dr. Dr. h. c. Oliver Kayser, Prof. Dr.-Ing. Norbert Kockmann and Prof. Dr.-Ing. Alba Diéguez Alonso, who served as my thesis supervisors and examiners. Their thoughtful scientific critiques significantly enhanced the quality of this research.

My sincere appreciation goes to Guanghui Niu for recommending me to Joachim's group, making me feel less alone in a foreign land and taking me into the world of the emission spectroscopy.

I am thankful to Luisa Speicher, my office-mate, whose helpful advice and cheerful companionship created a welcoming work environment. Norman Ahlmann also provided patient, professional guidance that enabled me to tackle challenging tasks confidently. Daniel Foest especially offered valuable feedback on the thesis. Simon Höving patiently offered the guidance on the writing and submission process on the thesis. Annika Fechner extended warm personal help and practical advice during my life in Germany. Christopher Brog and Arthur Schiller contribute their support and engaging conversation. I also express gratitude to other colleagues and friends I have had the pleasure of meeting during this period for their kindness and support, particularly Min Zhang.

Finally, I am especially grateful to my family, my parents, sisters, brother and my husband (Hao Song) for their support, encouragement and companionship. Sharing joy and challenges with me has meant the world.

Curriculum Vitae

Caiyan Tian

Date and Place of Birth: 18.02.1990 in Longnan, China

Work experience

- since Oct. 2020 **Research Associate**
Leibniz-Institut für Analytische Wissenschaften-ISAS-e.V.
Dortmund, Germany
- 2018.05-2020.09 **Project Management**
Sichuan Kelun Pharmaceutical Co., Ltd
Chengdu, China

Education

- Since Oct. 2020 **PhD in Physical Chemistry**
Miniaturisation
Leibniz-Institut für Analytische Wissenschaften – ISAS – e.V.
Dortmund, Germany
- Sep. 2014 – Jun. 2014 **M.Sc. in Biochemical and Molecular Biology**
Department of Life Science Sichuan University
Chengdu, China
- Sep. 2010 – Jun. 2014 **B.Sc.in Life Science**
Department of Life Science Tianshui Normal University
Tianshui, China
- Sep. 2007 – Jun. 2010 **High school**
Anhua High school
Longnan, China
- Sep. 1999 – Jun. 2007 **Elementary school**
Anhua Elementary school
Longnan, China